A discrete transport-mechanical approach for modelling the durability of concrete

Caroline Fahy

Infrastructure & Environment Research Division

School of Engineering

University of Glasgow

Submitted in fulfilment of the requirements for the Degree of Doctor of Philosophy

November 2014

Declaration

I declare that this thesis is a record of the original work carried out by myself under the supervision of Doctor Peter Grassl and Professor Simon Wheeler in the Infrastructure & Environment Division of the School of Engineering at the University of Glasgow, United Kingdom. This research was undertaken during the period of November 2010 to June 2014. The copyright of this thesis belongs to the author under the terms of the United Kingdom Copyright acts. Due acknowledgment must always be made of the use of any material contained in, or derived from, this thesis. The thesis has not been presented elsewhere in consideration for a higher degree.

Caroline Fahy

Abstract

Reinforced concrete is one of the most commonly used structural materials in the world and is used for buildings and many different types of civil engineering structures, such as bridges, tunnels and airports. The majority of these structures are required to remain in service for at least 50 years while some are expected to last well over 100 years. Fracture of these structures leads to an increase in the permeability of the concrete which in turn can result in increased ingress of water and other aggressive agents, such as chlorides or carbon dioxide, that accelerate the deterioration of these structures. Likewise, the mechanical properties of the concrete can be affected by the transport of moisture into the structure. The increase in moisture can lead to a reduction of the strength and the stiffness of the material.

The costs arising from structural failure are extremely high and in practice repair work tends to be implemented even when it is not entirely necessary. Therefore reliable approaches that can describe the interaction between the transport and mechanical properties of concrete and predict resulting structural degradation are of great benefit for practising engineers. Numerical models, such as the one proposed in this work, could be used for predicting when a repair is really necessary.

In this work, a transport-mechanical lattice approach to modelling the durability of concrete is proposed. The discretisation of the specimen domain is based on a dual Delaunay and Voronoi tessellation in which the edges of the Delaunay triangles form the mechanical elements and the transport elements are placed along the edges of the Voronoi polygons. The mechanical response of the concrete is described using an isotropic damage constitutive law, while the transport of moisture through the specimen is described using constitutive laws developed for mass transport through porous materials.

Both the mechanical and the transport models are assessed individually before the coupling

between the two models is implemented. The accuracy of the proposed coupled approach is validated through the analysis of an elastic thick-walled cylinder, in which the numerical results are compared with an analytical solution derived as part of this work. The proposed coupled approach is then applied to the case of corrosion-induced cracking of reinforced concrete structures. In this approach, the corrosion products are assumed to behave as a fluid and therefore values of fluid properties are required. A value of viscosity is determined based on the analysis of a concrete specimen containing a single reinforcement bar. Finally, the proposed approach is applied to a concrete specimen containing four reinforcement bars to assess the approach as a predictive model.

As expected with the concrete specimen containing a single reinforcement bar, very good agreement between numerical and experimental results is obtained. In the case of a specimen containing four reinforcement bars, it is observed that for small attack penetration depths the proposed approach is in very good agreement with experimental results. As the analysis continued, however, the numerical approach under-estimated the crack width when compared to experimental results.

Acknowledgments

I would like to start by saying a special thank you to my supervisor Dr Peter Grassl. Peter's constant guidance, knowledge and support throughout this project have been invaluable. He has shown tremendous patience and encouragement throughout this journey.

I would also like to thank Professor Domenico Gallipoli and Professor Simon Wheeler for their input into this work. Their guidance and support throughout this project have been greatly appreciated.

Next I must say a big thank you to my friends and collegues. To Ross, Alan and Graeme, thanks for all the chats, laughs, tea breaks and help with deciphering error messages. To Dimitris and Ignatios, you both proved to be better group members than tea makers but you have made our Friday meetings very enjoyable. Also, Dimitris, your I.T. support was greatly appreciated! Thank you also to Eri, Euan, Ali and the rest of my colleagues in room 604. The past three and a half years have been most enjoyable.

To my family; my mother, father and sister, thank you for your constant encouragement and support throughout this project and indeed throughout my many years of education! Also to Rita, for sparking a love of learning that would last a lifetime.

Finally a thank you to Shaun, my fiance, proof-reader, spell-checker and and everything else in between! Your unwavering support and encouragement throughout this project has made it possible for me to achieve this.

Contents

List of Figures

List of Tables

List of Symbols

Greek Symbols

α	Rust expansion coefficient
σ	Stress tensor
γ	Parameter for relating the elastic stiffness ratio of the lattice element to the Poisson's ratio of the continuum $((1-3\upsilon)/(\upsilon+1))$
κ_{i}	Intrinsic conductivity
κ_{r}	Relative conductivity
μ	Absolute (dynamic) viscosity of water
ρ	Fluid density
σ_{ϕ}	Rotational stress
σ_{n}	Normal stress
σ_{s}	Shear stress
θ_{m}	Model parameter for calculating the relative conductivity
θ_{r}	Residual water content
θ_{s}	Saturated water content
θ	Volumetric water content
$\tilde{\mathbf{n}}$	Vector of direction cosines to the normal boundary
υ	Poisson's ratio
ε_{ϕ}	Rotational strain

ε_n Normal strain

ε_s Shear strain

ξ Crack tortuosity parameter

α_e Conductivity matrix

Roman Symbols

$\mathbf{q}$ Flux

$\bar{w}_{c,max}$ Maximum equivalent mechanical crack opening

$\bar{w}_c$ Equivalent crack opening

$\mathbf{C}_e$ Capacity matrix

$\mathbf{D}$ Material stiffness matrix

$\mathbf{f}$ Vector of applied loads

$\mathbf{f}_e$ Nodal flow rate vector

$\mathbf{K}$ Stiffness matrix

$\mathbf{P}_c$ Fluid pressure vector

$\mathbf{T}$ Traction vector

$\mathbf{u}_e$ Displacement vector

$\mathbf{v}$ Vector for splitting radial force into corresponding vertical and horizontal components

G_f Fracture energy

ϕ Rotational degree of freedom

A Cross-sectional area of an element

a Model parameter for calculating the effective degree of saturation

b Biot's coefficient

C Midpoint of element

c Material storage capacity

C_{i} Constant of integration

d Dimensional parameter

d_{min} Minimum distance between nodes of the Delaunay tessellation

E Elastic modulus of lattice element

e Eccentricity of midpoint

E_{i} Equivalent stiffness of the interface elements

E_{c} Young's modulus of the continuum

f Depth of penetration of corrosion products into the pores

g Gravitational constant

h Length of mechanical element

i_{cor} Applied corrosion rate

I_{x} Influx in the x-direction

I_{y} Influx in the y-direction

k Conductivity

k_{c} Conductivity contribution due to cracks

k_{o} Material conductivity

M Mass

m Model parameter for calculating the effective degree of saturation

P Force

$P_{\mathrm{c(aev)}}$ Air entry value of capillary pressure

P_{c} Capillary pressure

P_{fi} Internal fluid pressure

P_{fo} External fluid pressure

P_{f} Fluid pressure

P_s Shear force

Q Total flow rate

q Flux (flow rate per unit area)

r Radius

S_e Effective degree of saturation

t Out of plane thickness of element

u Normal degree of freedom

u_{cor} Eigen-displacement

v Shear degree of freedom

V_c^{total} Total volume of corrosion products that have penetrated the pores (Section 7.4.2)

V_c^t Volume of corrosion products that have penetrated the pores at a particular time (Section 7.4.2)

w_{cr} Critical amount of corrosion products

w_{cn} Crack opening in the normal direction

w_{cs} Crack opening in the shear direction

w_f Parameter for determining the initial slope of the stress-strain curve

x_{cor} Attack penetration depth

z Elevation

Chapter 1

Introduction

1.1 Background

Reinforced concrete is one of the most commonly used structural materials in the world. It is used for buildings and many different types of civil engineering structures, such as bridges, tunnels and airports. The majority of these structures are required to remain in service for at least 50 years while some are expected to last well over 100 years. In many cases, these structures suffer from premature deterioration which leads to a shortened lifespan. The costs arising from structural failure are extremely high and therefore, in practice, repair work tends to be implemented even when it is not entirely necessary. It is therefore important that an accurate method of modelling coupled processes in concrete is developed to predict when repair work is really necessary.

The permeability of cementitious materials, such as concrete, is increased by fracture of the material. This in turn can lead to increased ingress of water and other aggressive agents, such as chlorides or carbon dioxide, that accelerate the deterioration of these structures. The mechanical material properties of the concrete are also effected by the transport of fluids. An increase in the degree of saturation can lead to a reduction of both stiffness and strength.

One of the most commonly encountered degradation processes is caused by corrosion of the reinforcement. The process of corrosion-induced cracking can be described by two distinct phases; initiation and propagation, as proposed by Tuutti (2981). The corrosion initiation stage refers to the process of de-passivation of the reinforcing steel by the introduction of chloride ions. This occurs when chloride ions break down the protective oxide film (passive film) that forms on the surface of the reinforcing steel. The corrosion propagation stage is the degradation of the reinforcement bar and the formation of the corrosion products, which occurs after the corrosion process has started. As the corrosion products are generated, they occupy a larger volume than the steel being consumed and can result in crack generation. There are large costs associated with inspecting, maintaining and repairing corroded structures. Numerical models can be used to indicate when a repair or a replacement is necessary and thus can be used to extend the lifespan of structures.

While there are many pre-existing numerical models available for predicting the cracking of concrete due to corrosion of the rebar, the penetration of the corrosion products into the pores and micro-cracks surrounding the rebar is not always considered. It is important to consider this penetration as it reduces the early stresses acting on the concrete that surrounds the rebar and hence delays the time to cracking. Therefore, the coupled approach developed in this work will be applied to the problem of corrosion-induced cracking of reinforced concrete.

1.2 Aims

The main purpose of this project was to develop a coupled transport-mechanical approach for modelling the durability of concrete. To achieve this, a discrete lattice approach is used to describe the transport and fracture properties of the concrete. The specimen domain is discretised using a dual Delaunay and Voronoi tessellation, in which the mechanical elements are placed along the edges of the Delaunay triangles and the transport elements are placed along the edges of the Voronoi polygons. This allows for coupling between the two models.

The novel element of this work is the coupling between the transport and mechanical models. This is enforced in two ways. Firstly, on the element level, the effect of pore fluid pressure on the mechanical effective stresses is considered, along with the effect of cracking on the permeability of the material. Secondly, coupling is enforced along the boundaries, in which either model can be used as a driving force for the coupled approach. For example, the application of a fluid pressure at a boundary results in deformation and cracking of the

mechanical mesh. Likewise, Eigen-displacements can result in a fluid pressure along the transport boundary. Each model is assessed individually before the coupling is enforced and the coupled approach is verified through the analysis of a thick-walled cylinder in which the numerical results are compared to an analytical solution derived as part of this work.

One of the main applications of the proposed coupled approach is the prediction of the lifespan of reinforced concrete structures due to the corrosion of the reinforcing bars. Although there are many existing numerical approaches available for predicting corrosion-induced cracking, the penetration of the corrosion products into the pores and micro-cracks within the concrete is not alway considered. As part of this work, an investigation of the influence of the movement of the corrosion products into the pores and micro-cracks within the concrete on the time to cracking is undertaken.

1.3 Assumptions

This thesis presents work on modelling the durability of concrete. Concrete is a heterogeneous material comprising cement, water and aggregates. In some cases admixtures are incorporated to improve one or more of the material properties, such as workability or porosity. Concrete is also a multi-scale material that can be loosely defined at three scales; micro, meso and macro level (van Mier,1997). At the micro-scale ($< 10^{-4}$ m), hydration products and capillary pores are visible. Individual aggregates and larger pores are visible at the meso-scale level ($10^{-4} < 10^{-1}$ m). At this scale, concrete is considered as a three phase composite material consisting of mortar matrix, coarse aggregates and interfacial transition zones between the aggregates and matrix. When considering the macro-scale level ($> 10^{-1}$ m), the concrete can be treated as a homogeneous material. The work presented later in this thesis deals with modelling of macro-scale specimens and thus assumes that the concrete is a homogeneous material.

1.4 Outline of Thesis

The thesis is divided into a number of chapters and the focus of each chapter is presented below.

CHAPTER 2 - A review of the existing literature is presented in this chapter and it is divided into three main sections. Firstly, a discussion of the applications for which a coupled transport-mechanical model would be beneficial is presented. Next a review

of experimental research carried out to investigate the physical problems outlined in the first section of this chapter. This section also highlights some of the problems with undertaking experimental work in these areas, again highlighting the need for a reliable transport-mechanical coupled approach. Finally, a discussion of existing modelling approaches available for describing transport-mechanical problems is presented and is sub-divided into three further subsections; discrete, continuum and mixed approaches.

CHAPTER 3 - In this chapter the modelling approach used in this work is presented. Firstly, the dual Delaunay and Voronoi tessellation used for discretisation of the specimen domain is presented. A dual mesh is considered along which the Delauany edges form the mechanical elements and the transport elements are placed along the edges of the Voronoi cells. Next the transport model is presented, starting with the differential equation and the constitutive laws. The mechanical model used in the proposed coupled approach is also presented in this chapter. In both cases, the coupling terms are highlighted. The coupling process is explained and the exchange of information along boundaries during the coupled analysis is also presented.

CHAPTER 4 - This chapter presents the initial work undertaken before coupling of the mechanical and transport models was enforced, in order to assess and verify each model individually. Firstly, analyses were carried out on notched concrete specimens that capture different modes of cracking using the mechanical model. Next, a transport analysis was carried out on a one-dimensional clay column to verify the implementation of the constitutive laws.

CHAPTER 5 - The transport model was used for analysing uncracked and cracked concrete specimens. In this two part investigation, an analysis is carried out firstly on an uncracked concrete specimen and the numerical results obtained are compared to experimental results reported in the literature. The effect of cracking on the permeability of the transport elements is considered in the second part of these analyses. This is the first instance of coupling between the individual mechanical and transport models.

CHAPTER 6 - The potential of the coupled lattice approach to describe the interaction of transport and mechanical responses was investigated by analysing an elastic plane stress thick-walled cylinder subjected to an internal fluid pressure. Firstly, the derivation of the analytical solution of a thick-walled cylinder is presented. Next the numerical results obtained using the proposed coupled approach are compared to the analytical solutions derived as part of this work. In this investigation, three values of Biot's coefficient were considered, corresponding to $b = 0$, 0.5 and 1, along with three values of Poisson's ratio $\nu = 0$, 0.1 and 0.2. Finally the effect of the staggered

approach used during the analysis on the numerically predicted results is investigated.

CHAPTER 7 - The proposed coupled lattice approach is applied to the plane stress analysis of concrete specimens with both single and multiple reinforcement bars. Firstly, the method for applying the corrosion layer is discussed and the method for calculating the corresponding reduction in steel radius is presented. It is assumed that the corrosion products behave as a fluid and therefore require fluid properties such as dynamic viscosity. The viscosity determined during the study is applied to an additional analysis to assess the ability of the proposed model for predicting corrosion-induced cracking in a specimen containing multiple rebars. A comparison between numerical and experimental results is presented. Finally a sensitivity study is presented. An investigation of the effect of parameters such as the viscosity of the corrosion products and the tortuosity of the cracks on the time to cracking is presented.

CHAPTER 8 - Conclusions arising from the work are presented in this chapter along with recommendations for future work.

Chapter 2

Literature Review

This chapter presents a review of the relevant literature and is divided into three main sections. Firstly, a discussion of the applications for which a coupled transport-mechanical model would be beneficial is presented. Next, a review of experimental research carried out to investigate the physical problems outlined in the first section of this chapter is discussed. Some of the problems with undertaking experimental work in these areas are also highlighted. Finally, a discussion of existing modelling approaches for describing transport-mechanical problems is presented.

2.1 Applications

This section examines potential applications of a coupled transport-mechanical numerical model. In this work, the term coupling means that the mechanical and transport models have an effect on each other. There are two forms of coupling that can occur. In the first instance, the transport model influences the mechanical model. This can occur in two ways. Firstly, the fluid pressure P_{f} (from the transport model) is required in the mechanical model (unless the Biot coefficient $b = 0$) to link the total stresses and the mechanical effective stresses. Secondly, the mechanical material properties can be affected by the transport model. In this case properties such as the strength, stiffness, etc, can be governed entirely by the mechanical effective stress (which will be influenced by the fluid pressure P_{f}). However, they can also be influenced by other variables coming from the transport model, e.g. degree of saturation or concentration of aggressive substances.

The alternative form of coupling involves the mechanical model influencing the transport model. For example, deformation leading to a change of porosity and/or cracking which changes the fluid storage capacity of the material and hence influences the transport model through the continuity of the fluid mass equation. Also, deformation can lead to a change of porosity and/or cracking that can lead to a change of conductivity.

Applications in which a coupled transport-mechanical model is of benefit include fracture in concrete, hydraulic fracture and corrosion-induced cracking of reinforced concrete. In many of these applications, experimental work can be expensive. Computational modelling can be used to enhance experimental works by offering the opportunity to investigate phenomena numerically before tailoring experiments to capture the required phenomena. Another advantage of computational modelling is that it can be used to analyse structures that are very difficult to test or that would take too long to test.

Considering the case of corrosion-induced cracking of reinforced concrete, both the effect of the transport model on the mechanical model and the effect of the mechanical model on the transport model are important. As the rebar corrodes, the constrained volume expansion of the corrosion products causes a mechanical stress on the concrete surrounding the rebar. Furthermore, these stresses cause some of the corrosion products to penetrate into the pores and micro-cracks surrounding the rebar (Wong et al., 2010). Initially, this penetration reduces the stresses acting on the concrete and delays the time to cracking. Once the corrosion products start to penetrate the pore network, the resulting pore pressure from the transport model influences the total stresses in the material. As the concrete cracks, the conductivity of the material increases and allows for the corrosion products to penetrate further into the concrete, thus the mechanical model influences the transport model.

The ingress of aggressive substances leads to a reduction of strength and stiffness due to chemical reactions that occur over time. Likewise, the transport of fluids through porous materials can also affect the mechanical material properties of porous materials. Materials such as soils can swell when the degree of saturation increases. This in turn can lead to a reduction of both the stiffness and strength occurs. If this swelling is restrained, cracking of the material may occur leading to areas where the fluid transport is increased and thus causing additional swelling and cracking (Roels et al., 2006). Another example of fluid transport affecting the mechanical behaviour of a material is shrinkage-induced cracking of concrete

(Bolander and Berton, 2004). Fluid transport can also affect the chemical composition of the material without causing any visible damage, and thus reduce the strength and stiffness of the material. Over time, this can result in the material no longer being fit for its original purpose.

Hydraulic fracturing is another area where the mechanical and fluid processes are coupled. Hydraulic fracturing occurs in saturated rock formations under high pressure and is a phenomenon that can occur both naturally or be induced manually (Valko and Economides, 1995). Induced hydraulic fracturing or "fracking" involves the injection of fracturing fluid into a wellbore at a very high pressure to initiate fracture (van Damme et al., 1989). This build up of fluid pressure causes cracking that influences the permeability of the material allowing for easier flow of the fluid. It can be difficult to experimentally observe the initiation, propagation and resulting stress evolution of the hydraulic fracture (Li et al., 2013) and due to this, it is important to be able to accurately simulate the process numerically. Hydraulic fracture can also occur in structures such as dams, where the pressure acting on the dam from the water causes cracking of the structure.

2.2 Experiments

Many of the phenomena discussed in Section 2.1 have been experimentally studied. This section discusses some of these experiments. In Section 2.2.1, experiments investigating cracking in concrete structures are discussed. Then, in Section 2.2.2, experiments on water transport through cracks are presented. Finally, in Section 2.2.3, corrosion-induced cracking experiments are addressed.

2.2.1 Cracking of concrete

It is important that the cracking process in concrete is understood as these cracks will influence the ingress of moisture or aggressive agents. A wide range of experimental studies have been carried out to investigate fracture processes in concrete. Some researchers consider small scale specimens of plain concrete, while others focus on larger scale specimens that represent more realistic structural members (Arrea and Ingraffea (1982), Nooru-Mohamed (1992), Vecchio and Shim, 2004, Nemecek, 2005). In the present study, the former type of structures are modelled. Therefore, a short review of this type of experiment is presented.

Tests investigating crack initiation and propagation in notched beams have been carried out for instance by Arrea and Ingraffea, 1982, Galvez et al., 1998 and Schlangen (1993). Arrea and Ingraffea (1982) carried out a four point shear test on a single-edge notched (SEN) specimen to investigate the resulting fracture patterns. Schlangen (1993) investigated mixed-mode fracture to develop an understanding of the fracture processes in concrete. The study consisted of experimental and numerical work. Experiments were carried out on beam specimens with either one or two notches and using various concrete mixes. One of the main findings of the experimental work undertaken was that even if the external loading on the beam was a combination of tensile and shear loading, fracture in the concrete was always a mode I mechanism. The knowledge gained from these tests was then used to develop a numerical model for simulating fracture processes in experiments and real structures.

Non-symmetric bending tests were carried out by Galvez et al. (1998) in which four point bending of notched beams was studied under the action of two independent force actuators. In this method, changes to one of the actuators allows for non-proportional loading and thus modifications to the corresponding crack trajectories. The main purpose of these studies was to develop results for comparing with numerical models, so that their potential for describing physical processes could be assessed. Other work has been carried out on notched specimens subjected to non-proportional loading to investigate the size effect in mixed-mode fracture (Nooru-Mohamed, 1992).

Numerical analysis of the tests undertaken by Arrea and Ingraffea (1982) and Nooru-Mohamed (1992) is presented in Section 4 of this document, where the geometrical parameters, loading setup and results will be discussed.

2.2.2 Water transport in cracked concrete

There are four mechanisms which allow for the movement of fluids or moisture through porous materials such as concrete. These are capillary action, permeation, diffusion and migration. Capillary action is the movement of liquid in small voids or pores due to the combined effects of cohesive forces, adhesive forces and surface tension. Cohesion and adhesion are the result of inter-molecular forces. Cohesion defines the attraction between the individual liquid molecules and adhesion defines the attraction between the liquid and the surrounding solid. Surface tension acts to maintain the surface of the liquid. Capillary action occurs when the adhesion to the surrounding solid is greater than the cohesion between the liquid molecules. Permeation is fluid movement caused by the action of a fluid pressure

gradient. Diffusion results from a concentration gradient and migration is due to an electrical potential gradient. In marine environments, for example, water penetration into concrete by capillary action is generally regarded as the main invasion process for dissolved chloride ions (Martys and Ferraris, 1997). The work presented in Chapter 4 of this report investigates the effect of permeation.

The literature reviewed for this work is divided into two areas of research. The first discusses research that investigates capillary action, while the second part presents work investigating the influence of cracking on the conductivity of concrete.

Wittmann et al. (2008) and Zhang et al. (2011) investigated water transport through uncracked concrete for a variety of different concretes and mortars. Before testing, all samples were oven-dried and some of the sides were covered with self adhesive aluminium foils to cause unidirectional water flow when one of the surfaces is put in contact with water. As soon as the sample was placed in contact with water, neutron images were taken in regular intervals to capture the absorption of water over time. Some important findings were observed during testing. Firstly, it was observed that concrete with a higher water–cement ratio absorbs much more water than concrete with a lower water–cement ratio. These tests also highlighted that when fine cracks in the concrete surface get in contact with water, they immediately become water filled. During testing an irregular water front was observed as the water moved upwards. This indicates that the material parameters of mortar samples are not completely homogeneous and this should be considered when developing numerical models.

The same group of researchers also investigated the time dependent process of water penetration into cracked steel-reinforced concrete specimens (Zhang et al., 2011). Firstly, a reinforced concrete specimen was cracked. Afterwards it was placed in water and the uptake of water through the specimen was monitored. Again, one of the main observations in this work was the increase in water uptake through cracks. This observation is very important when looking at the durability of cracked concrete as increased amounts of chloride ions can be transported into the concrete and eventually lead to the degradation of the reinforcing bar.

Roels et al. (2003) also investigated water uptake in fractured materials. However, in this case brick samples were tested rather than concrete specimens. In both the work presented

by Zhang et al. (2011) and Roels et al. (2003), it was observed that the fracture acts as an extra water source for the surrounding matrix, thus, highlighting the importance of including the effect of cracking in coupled numerical approaches.

More recently, Gardner et al. (2012) presented work on capillary action in discrete cracks in cementitious materials with the aim of validating an updated theoretical model. Three types of crack configurations were considered in these tests; planar, four-staged sloped and natural. The effect of crack aperture, specimen age, degree of saturation and crack configuration on the level and rate of capillary rise height was examined in this work. It was observed that the age of the specimen affected the response, for example, 7 day specimens had a faster capillary rise than 28 day specimens. The shape of the fracture also influenced the response. In the work presented later in this report, a tortuosity factor is considered that accounts for the shape of the fracture.

The second part of this review discusses experiments that investigate the effect of cracks on the conductivity of a material. Many of the coupled approaches discussed in Section 2.3, and in the coupled mechanical-transport approach proposed in this work, include the effect of cracking on the conductivity of the material. A cubic law for relating the conductivity to the cube of crack width is a popular choice amongst researchers for considering this effect (Grassl, 2009, Fu et al., 2013).

Witherspoon et al. (1980) investigated the validity of the cubic law for laminar flow of fluids through a deformable rock fracture. Horizontal fractures were created in cylindrical samples using a modified form of the Brazilian test. They found that the cubic law was valid regardless of whether the fracture surfaces were opening or closing. The results obtained from testing were also shown to be independent of the rock type.

Aldea et al. (2000) investigated the relationship between cracking and water permeability in loaded concrete specimens. A wedge splitting test was used to induce width-controlled cracks and the water flow was monitored for the loaded samples. The results of these experiments indicated that cracking has a significant effect on the water permeability, thus highlighting the need for inclusion in numerical models.

More recently, Wong et al. (2009) investigated the influence of interfacial transition zone (ITZ) and micro-cracking on the diffusivity, permeability and sorptivity of cementitious materials after drying. Some interesting conclusions were drawn from the tests. For example, it was observed that although the interfacial transition zone contains a higher porosity than the bulk paste, its effect on the overall transport properties is small. Moreover, the effects of parameters such as tortuosity and the presence of micro-cracks far out-weigh any effects of the high porosity ITZ.

Experimental work clearly shows the importance of considering the effect of cracking on the transport properties of porous materials such as concrete. Consideration of this effect is given in the coupled approach proposed as part of this work.

2.2.3 Corrosion-induced cracking of reinforced concrete

One of the aims of the present coupled transport-mechanical approach is analysing corrosion-induced cracking of reinforced concrete. A review of experiments on this process is presented in this section. Corrosion-induced cracking is caused by the constrained volume expansion of corrosion products. To develop an understanding of the formation of corrosion products and how their presence affects the surrounding concrete, many researchers have performed experiments to recreate this phenomena. One of the problems with this type of experiments is the time required for the corrosion products to form and to cause cracking. For example, Liu and Weyers (1998) carried out corrosion tests on forty-four reinforced concrete slabs over a five year period. Variations to the concrete mix, cover depths and reinforcement diameters were introduced to investigate the influence of these factors on the corrosion process. To initiate the corrosion process, different amounts of chlorides were added to the concrete. At the end of the tests, only ten of the specimens had cracked. The cracked specimens were those which contained the highest amounts of chloride admixtures. In some cases, it was possible to study corrosion products that had formed over a period of 60 years (Duffó et al. (2004)). These cases give a realistic view of the types of corrosion products produced. However, the time involved in these types of studies are not very well suited for typical short term research projects.

To reduce the time scale of experiments, accelerated corrosion tests are common. These accelerated tests allow for corrosion-induced cracking to occur within a matter of days, rather than years. For this type of experiment, the specimen is partially immersed in either water or a sodium chloride solution and a constant electrical current is applied to the steel bars

via a current regulator. A steel plate is placed within the fluid to act as a cathode while the steel rebar acts as an anode. For an applied current, Faraday's law can then be used to calculate the rate at which the attack penetration depth increases with time, where the attack penetration depth is the depth of steel transformed into rust (Andrade et al., 1993). The applied current density i_{cor} normally ranges between $10\mu A/cm^2$ and $100\mu A/cm^2$ (Andrade et al., 1993). However, some experiments use a greater applied density of $250\mu A/cm^2$ or $500\mu A/cm^2$. During these accelerated tests, researchers usually assume that the current efficiency of 100% is maintained during testing (Andrade et al., 1993). However, in reality it is unlikely that this assumption is correct due to factors such as imperfect cathode and anode ion exchange, variations in environmental factors or spalling of un-corroded steel from the bar surface (Mullard and Stewart, 2009a). This may result in the attack penetration depth calculated by Faraday's law to be greater than those observed experimentally.

In many cases, the main purpose of these experiments is to investigate the effect of material and geometric parameters on the time to cracking. Using a specimen with a single reinforcement bar, Morinaga (1990) investigated the effect of material and geometric parameters on cracking and used accelerated corrosion tests to determine the critical amount of corrosion products w_{cr} required for cracking. Andrade et al. (1993) observed during accelerated corrosion tests that cracking occurred at structurally negligible diameter loss of rebar regardless of the i_{cor}. Alonso et al. (1998) quantified the relationship between the amount of corrosion and cover cracking. It was observed during these tests that w_{cr} was not greatly affected by i_{cor}. More recently, Sanz et al. (2013) carried out accelerated tests to investigate the cracking of concrete due to corrosion products. However, a very large i_{cor} of $400\mu A/cm^2$ was applied, which may have had an effect on the type of oxides produced.

One of the main criticisms of many of the experimental studies is that many specimens used contained only one reinforcement bar. This does not accurately represent structural applications where commonly a number of reinforcement bars are present. Very few tests have been performed for specimens with multiple bars. Cabrera (1996) was one of the first researchers to consider a specimen with multiple reinforcement bars for studying the effect of cement type, bar diameter, cover thickness and orthogonally laid bars on cracking. Accelerated corrosion tests were carried out on specimens containing three main rebars and two secondary bars. The tests showed that cracking was influenced by the depth of cover, but spalling was not reported. Vu et al. (2005) carried out tests on eight rectangular reinforced concrete slabs. This type of specimen provides a more realistic representation of how cracks initiate and

propagate than specimens with a single reinforcement bar. The influence of concrete cover and water/cement ratio on the time to crack initiation and propagation was studied. As with previous accelerated tests, an i_{cor} of $100\mu A/cm^2$ was applied to the reinforcement bars. It was observed that individual cracks close to the rebar join to form one continuous longitudinal crack. This interaction of the rebars shows that there are important differences between specimens with one and multiple reinforcement bars.

Although more realistic than previous experiments, the tests carried out by Vu et al. (2005) failed to consider the effect of different rebar diameter sizes on the development of corrosion-induced cracking. To investigate this influence more carefully, Mullard and Stewart (2009a) looked at specimens containing five rebars. Variations to concrete cover, rebar diameter size and i_{cor} were included in this work. A study of the crack widths measured above internal and external rebars showed that the crack widths above internal rebars was less than those above external ones. It was also observed that individual cracks joined together and cause spalling of the concrete cover. The same authors later carried out experimental work on specimens containing four rebars (Mullard and Stewart, 2011). Again, the influence of the confinement on the internal crack widths was observed during testing.

During the corrosion process, the volume of corrosion products is higher than that of the original metal. The ratio between the volume of corrosion products and the volume of rebar consumed in the corrosion process is referred to as the "rust expansion coefficient". Experiments have been undertaken to learn more about the composition and properties of the corrosion products that are formed (Suda et al., 1993, Caré et al., 2008) and to determine the rust expansion coefficient α. A popular method for determining the composition of the corrosion products is X-ray diffraction (XRD) proposed by Suda et al. (1993) and used more recently by Duffó et al. (2004). From the composition of the corrosion products, Suda et al. (1993) calculated α as 2.74. Vu et al. (2005) also used this method on their experiments and determined α as 2.94. Other researchers have proposed values of this coefficient ranging from 2.0 - 3.2 (Ouglova et al., 2006, Mullard and Stewart, 2009b) and in some extreme cases a value of up to 6.4 was reported (Caré et al., 2008). When undertaking analyses, the value of α can be taken from the values determined by researchers in experimental work.

Some of the rust products penetrate into the pores and micro-cracks in the concrete surrounding the rebar (Wong et al., 2010, Michel et al., 2011, Andrade and Figueiredo, 2012, Michel

et al., 2013). Alonso et al. (1998) observed that an increase in porosity (w/c ratio) produces a delay in crack initiation. It is believed that this occurs due to the higher amount of void space available to accommodate corrosion products without stress generation. Experimental testing on a specimen containing three reinforcing bars was carried out by Wong et al. (2010) for the purpose of investigating the amount and distribution of corrosion products from corrosion initiation through to the point when significant damage to the specimen had occurred. Unlike previous tests, the researchers decided not to accelerate the corrosion process by the addition of admixed chlorides, an imposed electrical current or manufactured cracks. It was felt that such treatments would artificially influence the formation and distribution of the corrosion products. To create a more realistic exposure to chlorides, the specimens were placed in an environmental chamber and subjected to cyclic wetting and drying to induce corrosion. These tests showed the penetration of the corrosion products into the pores within the concrete surrounding the rebar. It was also observed during testing that once cracking is initiated, the corrosion products travel into the large cracks rather than into pore spaces in the cement paste.

Recently, work has been carried out to determine how far into the concrete surrounding the rebar the corrosion products penetrate (Michel et al., 2011, 2013). Michel et al. (2011) proposed a non-destructive test method using X-ray attenuation measurements to monitor the time-dependent development of corrosion products and subsequent corrosion-induced cracking. During the testing of this method, the rate of production of corrosion products was accelerated with an i_{cor} of $250\mu\text{A}/\text{cm}^2$. One possible problem with this method is the accuracy of the camera used during testing. It is difficult to determine if the accuracy is sufficient to capture individual pores and micro-cracks surrounding the reinforcement bar. Recent work carried out by the same authors, in which smaller current densities were applied, indicate that the corrosion products penetrate into the pores and micro-cracks (Michel et al., 2013).

2.3 Modelling

A vast number of approaches for coupling transport and mechanical problems have been proposed. In many cases, the coupling does not only describe the transport-mechanical relationship but also includes additional effects such as the effect of heat transfer or chemical diffusion (Bangert et al., 2004, Gawin et al., 2006). These coupled problems are not only applied to concrete but include a wide range of materials (Ababou et al., 1994, Liu and Rutqvist, 2012, Asahina and Houseworth, 2013). In this review, coupled approaches de-

veloped for describing the stress distribution in porous materials are discussed. Coupled transport-mechanical models can be divided into three categories; discrete, continuum and mixed approaches. A discrete coupled approach is proposed in this work and, therefore, the main focus of this literature review is on alternative discrete approaches available. Both continuum and mixed approaches are also reviewed, but with less emphasis than on discrete methods.

2.3.1 Discrete approaches

In terms of modelling fracture processes, discrete models use entities such as springs, and beams, to establish a relationship between the internal forces acting on the ends of the elements and the relative displacements and/or the rotations of these sections. These types of discrete models have been used extensively for modelling fracture in concrete (Zubelewicz and Bažant, 1987, Bažant et al., 1990, Bolander et al., 1996, Bolander and Saito, 1998, Cusatis et al., 2003). For transport problems, transport elements are idealised as conductive "pipes" (Bolander and Berton, 2004, Wang and Ueda, 2011). Discrete approaches are advantageous as they have been proven to be well suited to modelling both fracture and flow problems individually (Bolander and Saito, 1998, Grassl, 2009) and also coupled problems (Chatzigeorgiou et al., 2005).

One type of discrete approach was first proposed by Kawai (1978) and used more recently by Bolander and Saito (1998). Spring network models consist of either regularly or randomly distributed nodal sites interconnected by zero-sized springs. In a two dimensional analysis a Voronoi tessellation is used to produce irregular polygons across the domain. Each of these polygons maybe referred to as Voronoi cells. Construction of a Voronoi tessellation commences with the placement of a set of generator points throughout the domain. A Voronoi cell is then defined as the region closer to one generator point than to any other generator point in the domain (Okabe et al., 2000). The springs are located at the centre of the Voronoi facet with rigid-arm constraints that link the spring set and the nodal degrees of freedom, where each spring is governed by its own set of constitutive relations (Figure 2.1) (Bolander and Saito, 1998). Each spring set consists of normal, shear, and rotational springs that are assigned stiffnesses. For this approach, the initiation and propagation of fracture can be modelled by either a) removing springs or b) reducing the elastic properties of the springs (Bolander and Saito, 1998). One of the main advantages of this type of lattice model is that it can capture well the random characteristics of cracks such as location and direction.

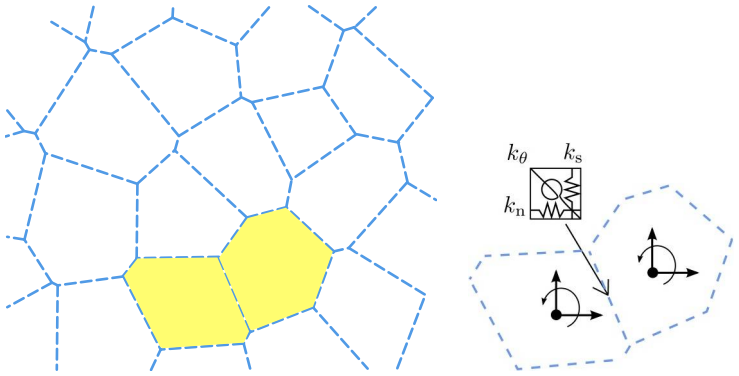

Figure 2.1: Rigid-Body-Spring Networks (RBSN) modified from Bolander and Hong (2003).

Bolander and Berton (2004) proposed a hygro-mechanical model for describing shrinkage induced cracking in cement composite overlays using lattice elements to represent the continuum. A random lattice based on a Voronoi tessellation of the domain was used to model both the moisture transport and crack development caused by the drying process. Rigid-body-spring-networks (RBSN) were used to describe elasticity, creep and fracture properties of the material. The random lattice was also used for modelling the moisture transport. In this case, conduit elements or "pipes" connected the lattice nodes and their geometry was defined by the Delaunay triangulation of the same set of generator points. In this triangulation, two nodes in the domain are joined by a Delaunay edge if their Voronoi cells are adjacent. Delaunay triangles are formed when their circumcircle does not contain any other points within its interior. The cross-section area of a given transport element was given by the length of the corresponding Voronoi facet. Moisture transport was governed by the diffusion equation and the effect of the transport model on the mechanical model was considered by assuming that the moisture distribution produced a shrinkage strain field. It was assumed that the diffusion process was uncoupled from the mechanical behaviour of the material and any damage incurred during mechanical or hygral loading.

Nakamura et al. (2006) employed a similar model for considering drying shrinkage due to moisture transport and rebar corrosion due to the penetration of chloride ions. Moisture transport was described by the network model. As with the previous work by Bolander and Berton (2004), coupling between the transport and mechanical models was taken into account by assuming a shrinkage strain field. The RBSN model was also used by Wang et al. (2008) for describing fracture in their proposed model for simulating the chloride diffusivity for concrete. In this approach, the diffusion coefficient in the transport model depended on

the crack opening of the mechanical model. Firstly, cracking of the specimens was carried out and the crack widths were determined by calculating the elongation of the normal spring. The network model was also adopted for evaluating the chloride diffusivity of cracked concrete.

Asahina and Houseworth (2013) used the RBSN method for describing fracture development in geomaterials and a finite volume method for modelling wetting and drying. The coupling of the mechanical and transport models was considered in two ways. In the first instance, Biot's theory of porous solids (Biot, 1941) was introduced to account for the effect of the fluid pressure on the mechanical stresses. Secondly, and in a similar approach to previous work carried out by Nakamura et al. (2006), the effect of moisture transport on the mechanical model is enforced by a shrinkage/swelling strain acting on the mechanical model. Here, it is assumed that local changes in the liquid saturation induce the strain. Finally, the effect of cracking on the permeability is considered through a parallel plate model.

Another type of discrete model represents the continuum specimen as a lattice of frame or truss elements. Lattice elements are linear elements defined by two nodes located at either end of the element. Originally beam elements in a regular square formation were used for modelling fracture processes (Hrennikoff, 1941). One of the problems with using a regular square lattice is that it produces a Poisson's ratio equal to zero (van Mier, 1997), making it unsuitable for modelling materials such as concrete. Another problem is that the fracture patterns are strongly aligned with the mesh lines. For modelling concrete, the use of a regular triangular lattice of beam elements was adopted by Schlangen and Mier (1992). A random lattice approach using triangular lattices was originally proposed by Moukarzel and Herrmann (1992). Schlangen and Mier (1992) used a triangular lattice for modeling fracture of concrete. They introduced two different methods for introducing randomness into the mesh before comparing the results to experiments. In the first instance, the element properties were determined by projecting the lattice onto a generated grain structure of the concrete and assigning different strengths and stiffness to the respective elements. Secondly, a distribution of element strengths or stiffnesses was introduced to replicate the heterogeneity of the concrete. Good agreement between the numerical results and experiments was obtained in this work, indicating that lattice models are suitable for modelling fracture in concrete. Schlangen and Garboczi (1996) further investigated the influence of the mesh on the resulting fracture patterns. Three different meshes were considered; triangular, rotated triangular, and square. Although the fracture patterns were replicated well, the crack shapes differed

due to the different orientation of the meshes used. To overcome the mesh dependency, a random lattice was introduced.

Random lattices are still a popular choice for modelling fracture in concrete. In this case, the nodes are randomly defined based on the Voronoi discretisation of the material domain (Berton and Bolander, 2006) and the lattice elements are then defined as the edges of the triangles of the Delaunay triangulation (Grassl and Jirásek, 2010). When modelling aggregates the nodes may be placed at specified locations within the domain. This ensures that the midpoint of the lattice element is aligned with the theoretical boundary between the aggregate and the mortar (Bolander and Berton, 2004). The discrete approach has advantages over the continuum approach by allowing the application of different cross sectional areas to each individual element. Also, when an individual element exceeds its capacity it can be removed to simulate a crack in the material. It has been noted by some researchers that continuum fracture models may not converge when dealing with multiple crack paths and the method works better if the location of the crack is known beforehand, allowing for the element boundaries to be placed along the crack path (Yu et al., 2008).

A coupled approach for modelling crack growth due to moisture movement was proposed by Sadouki and van Mier (1997) in which lattice elements in the form of beams were used to describe the fracture of concrete. In this work, a triangular network of beam elements was used to discretise the specimen domain. Consideration of the different phases of the material was given by projecting the material on top of the lattice and assigning the material properties to the elements based on this projection. As with the other approaches discussed previously, the transport elements were considered as one-dimensional conductive pipes. Coupling of the effect of moisture transport on the mechanical response of the concrete was considered in a similar method to that proposed by Nakamura et al. (2006).

Jankovic (2001) adopted a lattice approach for modelling moisture flow in the interface zone. A lattice fracture model was used to simulate the cracking of concrete, combined with a lattice gas automation model for the moisture transport. The effect of moisture movement on the mechanical response of the concrete was considered by means of a shrinkage coefficient. These shrinkage strains led to shrinkage stresses, which were applied as pre-stresses on the sample in order to induce cracking.

Grassl (2009) also proposed a coupled lattice approach for modelling flow in concrete. Again, the lattice model was based on a dual Voronoi and Delaunay tessellation of the specimen domain. Beam-like elements were placed along the edges of the Delaunay triangles. This type of elements is used as part of the coupled approach proposed as part of this work and will be discussed in more detail in Chapter 3. The mechanical response of the concrete was described by Grassl (2009) by a lattice approach combined with a damage-plasticity constitutive model. Transport elements were placed along the edges of the corresponding Voronoi polygons and moisture transport was governed by a diffusion equation similar to the approach by Bolander and Berton (2004). An advantage of this method is that information regarding crack widths can be easily transferred to the transport model as the mechanical element crosses the corresponding transport element. The influence of the mechanical model on the transport properties was considered by using a simple linear law was used to relate crack widths obtained from the mechanical model to the change in diffusivity in the transport model. In this work, the influence of the transport model on the mechanical model was not considered.

In each of the cases presented above, good agreement between experimental and numerical results was obtained. However, full coupling between the transport and mechanical models which allows for the effects of the transport analysis on the mechanical response and vice versa has been enforced in only a minority of cases in the approaches discussed in this section.

2.3.2 Continuum approaches

In continuum approaches, the mechanical behaviour of a specimen is modelled by a stress-strain law and cracks are considered by using higher order constitutive laws. One of the main problems with continuum approaches is that they can be computationally expensive. Thomas and He (1997) presented an approach that coupled heat and moisture transfer in partially saturated soil for considering the effect of a temperature gradient and deformations on flows. One way in which the coupled effects were considered was through assuming that the strains are dependent on net stress, capillary suction and temperature changes.

Pijaudier-Cabot et al. (2009) proposed an approach which incorporated the effect of damage on the permeability of concrete. In this approach, the mechanical behaviour of the material was captured using a non local integral damage model (Pijaudier-Cabot and Bažant, 1988). The effect of damage on the permeability was included by assuming a relationship between

the logarithm of the permeability and the damage in the material. One possible disadvantage of this approach is that the effect of crack closure on the permeability is neglected, and thus the permeability can overestimated.

More recently, Liu and Rutqvist (2012) proposed a dual-continuum system for modelling coupled hydraulic and mechanical deformation processes. Unlike many of the previous coupled approaches discussed so far, the purpose of this model was to accurately describe hydraulic fracture in rock. In this work, continuum mechanics formulations were used to describe flow and transport and mechanical deformations. A pore-space conservation equation was developed that describes the pore-space evolution resulting from the coupled hydraulic and mechanical process. This equation was then combined with a fluid mass balance equation, leading to the derivation of a governing equation for fluid flow in fractured rock. The coupling between the fluid pressure and the mechanical stresses was based on Biot's theory of porous solids (Biot, 1941). Li et al. (2013) also proposed a coupled approach for modelling hydraulic fracture in rock formations.

The approaches discussed above consider the effect of cracking on the permeability of the material. However, the effect of pore pressure on the mechanical effective stresses in the material is not always considered in these approaches.

2.3.3 Mixed approaches

In mixed approaches, cracks are represented by displacement discontinuities embedded within the continuum. Noorishad et al. (1982) were among the first researchers to propose a coupled approach for the analysis of coupled mechanical and fluid flow phenomena in deformable saturated fractured porous media. Meschke and Grasberger (2003) proposed a coupled hygro-mechanical model for simulating the effects of moisture and external loading on the integrity of new and existing concrete structures. A multi-surface poroelastic damage approach was used to model the mechanical behaviour of the concrete. Cracks in the material were captured using a smeared crack approach. In this approach coupling in both directions between the two models is included, thus moisture movement may cause cracking and in turn, cracking influences the transport properties of the material. The effect of the fluid pressure on the mechanical effective stresses in the material is considered through Biot's theory of porous solids (Biot, 1941). The effect of cracking on the permeability of the concrete is considered by a quadratic law that also considered the effect of the tortuosity of the crack.

Roels et al. (2006) proposed a coupled discrete-continuum approach for simulating moisture effects on damage processes in porous materials. The proposed model was divided into three components; a poromechanical continuum model for the uncracked porous matrix and two discrete models, one for simulating the damage process and one for describing the liquid flow in fractures. Cracks were modelled as displacement discontinuities that were able to propagate throughout the mesh. In this work coupling of the mechanical and transport models is introduced in three ways. Firstly, the effect of the fluid pressure on the mechanical effective stresses in the material was considered through Biot's theory of porous solids (Biot, 1941). Secondly, the effect of degree of saturation on the material properties such as the Young's modulus was considered. Thirdly, the effect of cracks on the transport properties such as permeability was accounted for through a quadratic law relating the crack widths to the increase in permeability. A staggered approach was used for solving the transport and mechanical models during analyses. Firstly the transport problem was solved, during which the geometry of the cracks taken from the previous time-step is used when calculating the increase in permeability due to cracking. Next, the capillary pressure field obtained in the transport analysis was used to calculate the mechanical behaviour. The capillary pressure P_c was assumed to remain constant during the iteration procedure of the mechanical behaviour. During the next stage of the analysis, the updated geometry of the discontinuities (cracks) was exchanged with the moisture transport model. This process continued for the duration of the analysis.

Jox et al. (2007) also proposed a coupled approach for modelling partially saturated cracked concrete in which the Extended Finite Element Method (XFEM) was used to describe the mechanical response of the specimen and a diffusion model describes the moisture transport. In this work, coupling was introduced through the concept of effective stresses and also through the increase in permeability due to cracking.

Idiart et al. (2010) proposed a coupled hygro-mechanical approach for meso-scale modelling of the shrinkage of concrete specimens due to drying. In this model, cracking was introduced through zero-thickness interface elements. These interface elements were placed along all particle–matrix interfaces and some selected matrix–matrix lines. Coupling was considered through the effect of cracking on the diffusivity of the concrete by a cubic law.

More recently, Fu et al. (2013) proposed a coupled approach for modelling hydraulic frac-

turing. A similar method to that used by Roels et al. (2006) for accounting for the effects of cracking on permeability was implemented in this approach. Previously, a quadratic law was used to relate the crack widths to the increase in permeability, however, in this work a cubic law was introduced. One possible disadvantage of this model is that it appears that it does not consider the effect of the fluid pressure on the mechanical effective stresses acting in the specimen.

Kim and Moridis (2013) also developed a coupled thermo-mechanical approach. The purpose of this model was to describe fracture propagation and coupled flow-thermal-geomechanical processes in tight/shale gas systems. The effect of cracking on the permeability of the material was considered by a cubic law. In this approach, the roughness of the fracture was also considered.

Using mixed approaches to couple mechanical and transport models can be more beneficial than using continuum approaches. However, computational difficulties can be encountered when dealing with moisture transport through cracks.

2.3.4 Modelling of corrosion-induced cracking

A short review of existing models for describing corrosion-induced cracking is presented herein. The limitations and shortcomings of these models are discussed. Approaches for modelling corrosion-induced cracking of reinforced concrete can be divided into three groups; empirical (Beaton and Stratfull, 1963, Clear, 1976, Morinaga, 1990, Purvis et al., 1994), analytical (Bažant, 1979, Liu and Weyers, 1998, El Maaddawy and Soudki, 2007, Chernin et al., 2010) and numerical (Molina et al., 1993, Lundgren, 2002, Chernin and Val, 2011, Grassl and Davies, 2011, Michel et al., 2013, Savija et al., 2013). As a numerical approach is proposed in this work, only the limitations of existing numerical approaches will be discussed from this point. When the earliest models were developed, the corrosion products were applied as an expansion of the rebar (Molina et al., 1993). The main drawback of this approach is that it does not capture the penetration of the corrosion products into the pores and micro-cracks surrounding the steel and the compaction of the corrosion products as they form. Therefore, the crack widths obtained with these models were greater than measured in experiments.

Over time, more advanced models have been developed to include the effects of the compaction of the corrosion products and their penetration into the pores and micro-cracks (Michel

et al., 2013). However, it is not clear how to model the penetration of the corrosion products correctly. Some researchers have assumed a reduction of the volume of corrosion products to account for the penetration of the rust into the pores. Others assume the presence of a "corrosion accommodating region" (CAR) that surrounds the rebar, which is interpreted as a very porous layer that surrounds the rebar. Its presence has been observed in experiments (Michel et al., 2013).

More recently, Ožbolt et al. (2014) have proposed a numerical approach in which the penetration of the corrosion products was treated as a convective diffusion problem. Reasonable agreement with experimental results was obtained in this work. However, only a comparison to experimental results that were used to calibrate the model was carried out and the model was not used to predict cracking using any additional specimens.

In many cases, the potential of the proposed approaches as predictive models are not investigated. In the present study, the viscosity of the corrosion products has been determined based on one experiment. This viscosity is then used to predict corrosion-induced cracking in another specimen.

Chapter 3

Modelling Approach

This chapter presents the modelling approach used in this work. Firstly, the dual Delaunay and Voronoi tessellation used for discretising the specimen is presented. A dual mesh is considered in which the Delauany edges form the mechanical elements and the transport elements are placed along the edges of the Voronoi cells. The differential equations for both the transport and mechanical models are presented and the corresponding discrete forms are discussed. The constitutive laws used for the two models are presented and their coupling is explained.

3.1 Domain Discretisation

Discretisation of the material continuum is based on a dual Voronoi and Delaunay tessellation with random geometries (Bolander and Saito, 1998). A three stage process is used for the discretisation of the specimen domain. Firstly, random nodes are placed throughout the domain. Next the program Triangle is used to generate the dual Voronoi and Delaunay tessellation (Shewchuk, 2002). Finally, the input files are created using the data produced during stage two of the process.

In the first stage of the process, nodes are placed at specific locations such as the corners of the specimen, supports and loading points. Next, nodes are placed randomly along the boundaries of the specimen. Then, nodes are placed randomly in the domain, with the constraints of a minimum distance $d_{\min}$ between the nodes and the number of maximum itera-

tions when generating the coordinates of a node. The minimum distance $d_{\min}$ also applies to the nodes placed along the boundaries of the specimen. After the nodes have been placed (Figure 3.1a), the domain is divided up into cells surrounding each of the nodes, shaped such that the edges of the cells are equidistant from the two nearest nodes. This forms the Voronoi cells (Figure 3.1b). The dual to the Voronoi tessellation is the Delaunay triangulation. One of the main properties of tessellation is that for every Voronoi tessellation of a domain, there is a corresponding unique Delaunay triangulation (Okabe et al., 2000). Two nodes in the domain are joined by a Delaunay edge if their Voronoi cells are adjacent. Three nodes in the specimen form a Delaunay triangle when their circumcircle does not contain any other points within its interior. Figure 3.1c shows the final discretisation of a domain. The blue dashed lines indicate the Voronoi edges and the solid purple lines form the Delaunay triangles. For nodes placed along the boundary, the corresponding Voronoi edges tend to infinity. Therefore, the nodes are moved from infinity to the boundary to ensure that they finish at the boundary of the domain.

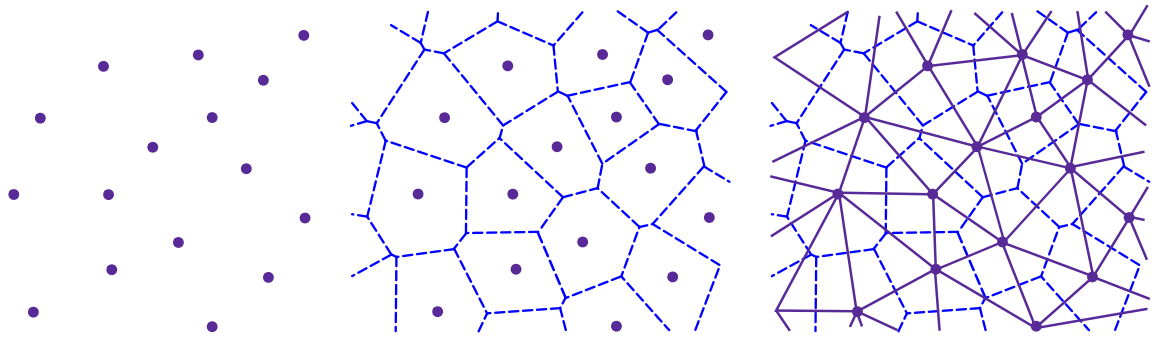

Figure 3.1: Dual Voronoi-Delaunay tessellation: (a) randomly placed points, (b) Voronoi tessellation, (c) Delaunay triangulation.

As stated earlier, there are two constraints that influence the final mesh; the minimum distance between nodes $d_{\min}$ and the maximum number of iterations allowed when placing the nodes. The minimum distance $d_{\min}$ controls the refinement of the tessellation. Figure 3.2 shows three different refinements, the ratio of the values of $d_{\min}$ were chosen as 1, 2 and 4 and the maximum number of iterations allowed was 1000. As $d_{\min}$ is reduced, a finer tessellation of the domain is achieved, thus resulting in a finer mesh. This constraint only controls the minimum length of the Delaunay edges as these connect the nodes. The minimum lengths of the Voronoi edges is not determined by $d_{\min}$.

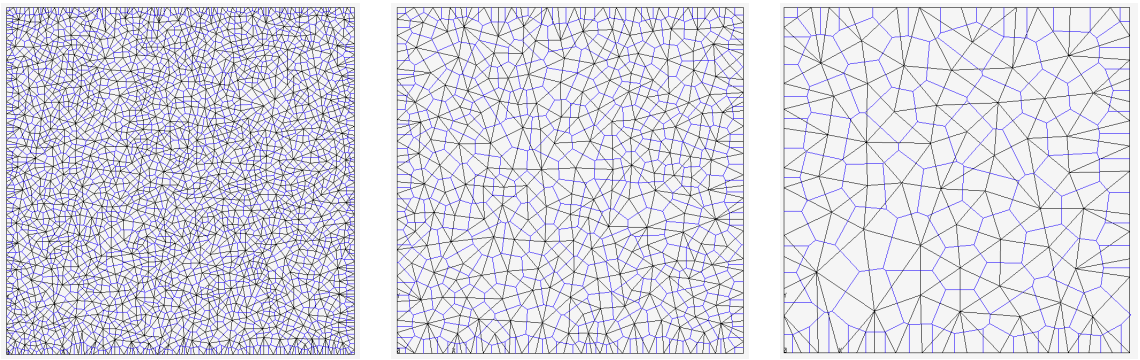

(a) (b) (c)

Figure 3.2: Effect of $d_{\min}$ on the mesh refinement: (a) $1\,d_{\min}$, (b) $2\,d_{\min}$, (c) $4\,d_{\min}$.

The other constraint is the maximum number of iterations allowed when placing nodes. Every time a node is placed, its location is checked against other nodes to ensure the specified minimum distance is maintained. Take for example two nodes denoted as node A and node B. Firstly node A is placed, then the random coordinates for node B are determined. If node B cannot be placed at the proposed position because the distance to a neighbouring node is too small, then new coordinates will be generated. This process is repeated until either acceptable coordinates are found or the maximum number of iterations for placing nodes is reached. Figure 3.3 shows the effect of three different maximum number values on a $100\,\text{mm}^2$ specimen with $d_{\min} = 0.5\,\text{mm}$. The number of maximum iteration values were taken as 1, 100 and 1000.

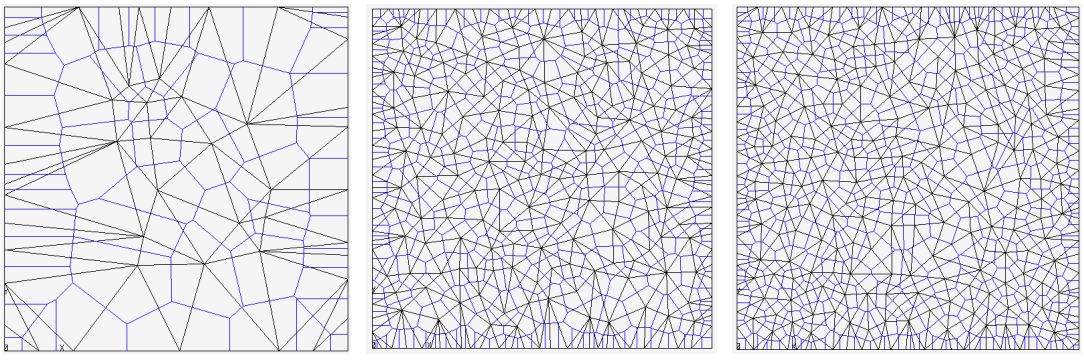

(a) (b) (c)

Figure 3.3: Effect of the maximum number of iterations on the mesh: (a) 1, (b) 100 and (c) 1000.

The dependence of the average length of the Delaunay and Voronoi edges on the maximum number of iterations is shown in Figures 3.4 and 3.5, respectively. For a lower number of

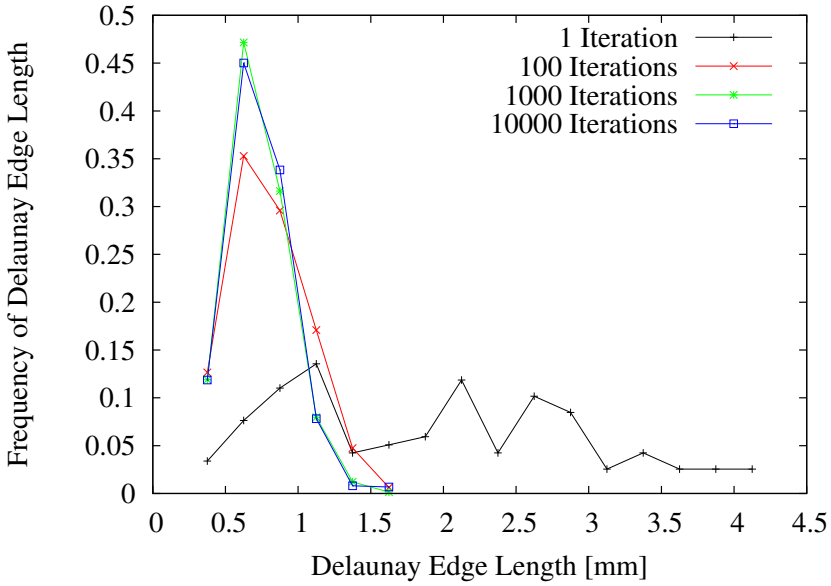

Figure 3.4: Normalised Delaunay edge length distribution.

maximum iterations, there is a much larger spread of Delaunay edge lengths than for when a larger number of maximum iterations is permitted. Figure 3.4 shows that as the number of iterations increases, the frequency of the Delaunay edge lengths converges. There is very little difference between the edge lengths when 1000 and 10000 iterations are considered. However, when the maximum number of iterations is set to 1000 the nodes are generated much quicker. Based on these findings, the maximum number of iterations specified when generating nodes in a domain is chosen as 1000. In Figure 3.4 the presence of Delaunay edge lengths of less than the specified $d_{\min} = 0.5\,\text{mm}$ can be seen. These occur because the minimum distance between the nodes is reduced along the boundaries.

The corresponding Voronoi edge lengths highlight the existence of very small Voronoi edges, much smaller than the minimum distance specified in the node generation. This occurs because the minimum distance $d_{\min}$ controls only the minimum spacing of the end points of the Delaunay edges and does not influence the minimum length of the Voronoi edges.

Along the boundaries the minimum distance between the nodes is reduced in order to avoid problems that can occur during the tessellation of the domain. In Figure 3.6, a $100\,\text{mm}^2$ specimen was discretised with $d_{\min} = 0.5\,\text{mm}$ and the maximum number of iterations chosen was 1000. Previously, the minimum distance between nodes placed along the boundary was half of the specified $d_{\min}$ value. However, in Figure 3.6 the minimum distance between

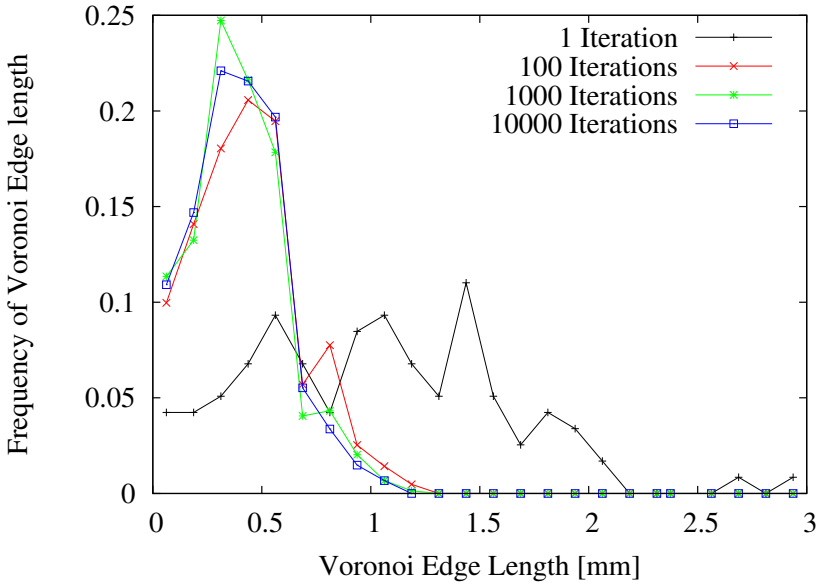

Figure 3.5: Normalised Voronoi edge length distribution.

boundary nodes was equal to $d_{\min}$. In this case, many Voronoi edges are placed outside of the domain. There are also a number of very large and shallow Delaunay triangles close to the boundaries.

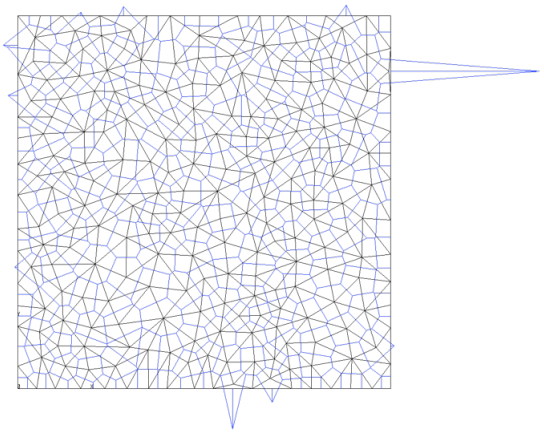

Figure 3.6: Meshing problems along the boundaries if $d_{\min}$ is unchanged.

Finally, the information obtained through the triangulation process is prepared for use in the analyses. For the transport model, one-dimensional transport elements are placed along the edges of the Voronoi polygons (blue dashed lines in Figure 3.7a) and their cross-sectional properties are determined from the corresponding Delaunay triangle edges (Grassl (2009)). In Figure 3.7b P_{f} is the nodal unknown (fluid pressure) of the transport model.

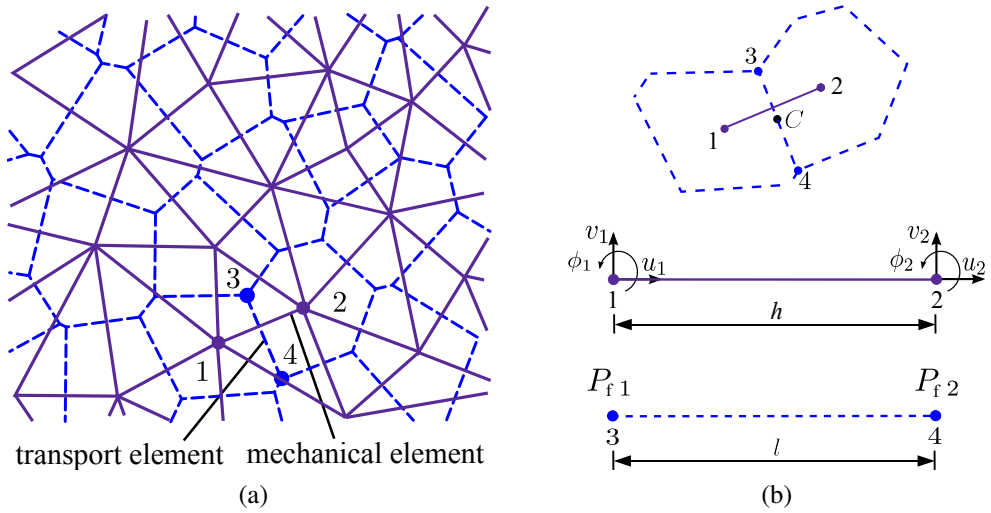

Figure 3.7: (a) Lattice based on Voronoi polygons, (b) Lattice element in the global coordinate system (Grassl and Jirásek, 2010).

The mechanical model consists of one-dimensional lattice elements corresponding to the edges of Delaunay triangles (Bolander and Saito, 1998) (Figure 3.7a). The geometry of the mid cross-section of the elements is determined by the corresponding Voronoi polygon edges. A mechanical lattice element is shown in Figure 3.7b (purple solid line). Each mechanical node has three degrees of freedom, two translations and one rotation, shown in Figure 3.7b as u, v and ϕ. Information for both the mechanical and transport constitutive models is exchanged at point C in Figure 3.7b.

More complicated meshes are required that allow for inclusions within the domain. Two types of inclusions are considered in this work. The first assumes that there is a hole and therefore it is not meshed either for the transport or the mechanical meshes (Figure 3.8). In this case, nodes are placed along the boundary of the hole and both the transport and mechanical elements end along the boundary of the inclusion. A tessellation of the domain is carried out, including areas of inclusions. As the information from the tessellation is being prepared for use in analyses, any elements with a node on either side of the boundary of an inclusion is modified. The node within the inclusion is moved to the boundary, thus reducing the length of the original element. This procedure is carried out for both the transport and mechanical elements allowing for the elements and cross-sections to finish at the boundary of any inclusions.

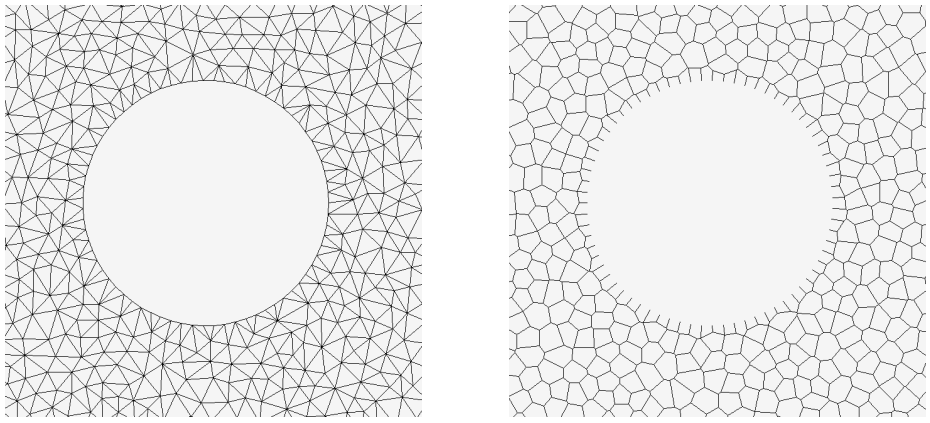

(a) (b)

Figure 3.8: Specimen with a hole in the centre: (a) mechanical mesh, (b) transport mesh.

The alternative option is to assume that the inclusion is impermeable to fluids but has mechanical properties. In this case, the inclusion is meshed as part of the mechanical model but any transport nodes or elements within the inclusion are not included as part of the transport mesh (Figure 3.9). Nodes are placed within the inclusion and just outside it, thus forming elements that cross the boundary between the inclusion and the rest of the specimen. Transport elements along the boundary of the inclusion are considered only in the radial direction, no fluid transport is permitted along the tangent of the boundary.

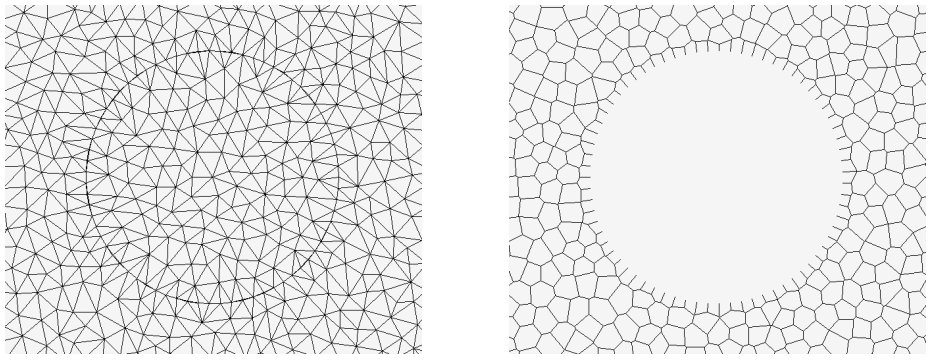

(a) (b)

Figure 3.9: Specimen with an impermeable inclusion: (a) mechanical mesh, (b) transport mesh.

3.2 Transport Model

The differential equation for the transport model is presented in this section. The discrete form for individual transport elements approximating the differential equation is also discussed and the constitutive laws are presented.

3.2.1 Differential equation

The balance equation presented in this section describes the stationary volume flow through a transport element subjected to fluid pressure gradient. In the balance equation, the flux (i.e. the rate of liquid flow per unit area) is related to the pressure gradient through Darcy's law, which gives

$$c\frac{\partial P_{\mathrm{c}}}{\partial t} - \frac{k}{g}\mathrm{div}\left(\mathrm{grad}(P_{\mathrm{c}} - \rho g z)\right) = 0 \tag{3.1}$$

where c is the storage capacity of the material ($1/\mathrm{mm}$), P_{c} is the capillary pressure with the units of MPa, k is the conductivity (mm^2), g is gravity, ρ is the density of the fluid and z is the elevation. The complete derivation of this differential equation is presented in Appendix A of this document. The storage capacity of the material c is defined as

$$c = -\rho\frac{\partial \theta}{\partial P_{\mathrm{c}}} \tag{3.2}$$

where θ is the volumetric water content and is the ratio between the volume of water and the volume of solids with the units of $\mathrm{mm}^3/\mathrm{mm}^3$. Boundary conditions are imposed as either a prescribed value of capillary pressure (along Γ_1 in Figure 3.10) or as prescribed values of flux (along Γ_2 in Figure 3.10). The resulting mathematical constraints are

$$P_{\mathrm{c}} = g(\mathbf{x}) \quad \text{on } \Gamma_1 \quad \text{and} \quad -\frac{\partial P_{\mathrm{c}}}{\partial \mathbf{n}} = f(\mathbf{x}) \quad \text{on } \Gamma_2$$

where $\mathbf{n}$ denotes the direction normal to the boundary and $g(\mathbf{x})$ and $f(\mathbf{x})$ are functions of the spatial coordinate vector $\mathbf{x}$ (Figure 3.10).

If the material is saturated and any changes in porosity are ignored, the capacity term reduces

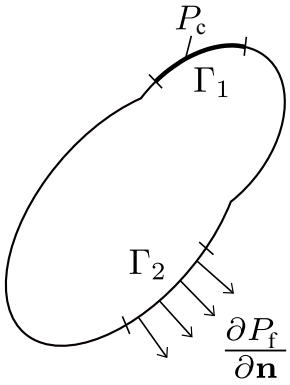

Figure 3.10: Transport boundary conditions.

to zero. Thus, (3.1) becomes

$$\frac{k}{g}\text{div}\left(\text{grad}\left(P_c - \rho g z\right)\right) = 0 \tag{3.3}$$

3.2.2 Discrete equation

To transform the differential form of (3.1) into a discrete version for use on individual elements, the time derivative and conductivity terms in (3.1) are derived by averaging over a control volume (Saka et al., 2012). Equation (3.1) is integrated over a triangular domain associated with a particular node. Next the integral is divided into a sum of sub-integrals over the domains associated with lattice elements connected to that particular node. Both terms in (3.1) are discretised (Saka et al., 2012). Finally, the discrete form of (3.1) for a one-dimensional transport element is defined as

$$\alpha_e \mathbf{P}_c + \mathbf{C}_e \frac{\partial \mathbf{P}_c}{\partial t} = \mathbf{f}_e \tag{3.4}$$

where $\mathbf{P}_c$ is the vector containing the nodal values of fluid pressure, α_e is the conductivity matrix, $\mathbf{C}_e$ is the capacity matrix and $\mathbf{f}_e$ is the nodal flow rate vector. The term involving $\text{grad}\left(\rho g z\right)$ in (3.3) is neglected in (3.4) as it is assumed that the gradient of the elevation is negligible. The conductivity matrix α_e is defined as

$$\alpha_e = \frac{A}{l} k \begin{pmatrix} 1 & -1 \\ -1 & 1 \end{pmatrix} \tag{3.5}$$

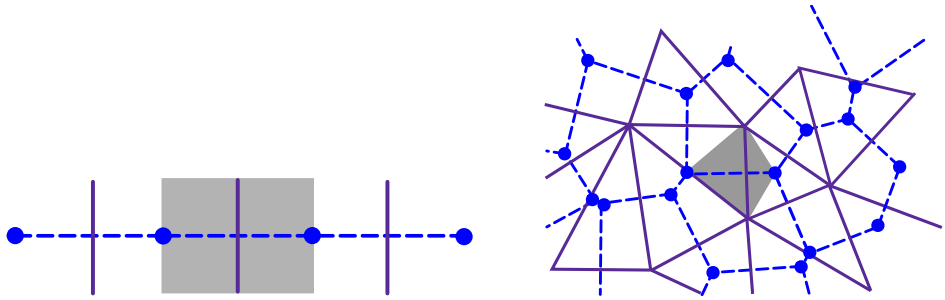

Figure 3.11: Areas considered for one-dimensional and two-dimensional modelling: (a) one-dimensional rectangular area and (b) two-dimensional polygon area.

and the capacity matrix $\mathbf{C}_e$ is

$$\mathbf{C}_e = \frac{Al}{6d} c \begin{pmatrix} 2 & 1 \\ 1 & 2 \end{pmatrix} \tag{3.6}$$

where $A = ht$ is the cross-sectional area, in which t is the out of plane thickness of the element assuming a rectangular cross-section and d equals 1 for a one-dimensional element or 2 for a two dimensional element. The reason for these different values for d is the assumed area belonging to the element. Figure 3.11 shows the difference in the areas. For a rectangular cross-section (Figure 3.11a) (3.6) would correspond to d equal to 1. In a two-dimensional domain (Figure 3.11b), d in (3.6) equals 2. This reduces the area that corresponds to an element to half of the rectangular are in the one-dimensional case. This prevents any overlapping of areas throughout the domain.

3.2.3 Constitutive models

Equations (3.1) and (3.4) require constitutive laws for calculating both the conductivity k and the capacity of the material c. The constitutive models used in this work were proposed by van Genuchten (1980) and later modified by Vogel et al. (2000). For materials that have a steep shaped water retention curve the original van Genuchten model can be numerically unstable, therefore, to overcome these instabilities Vogel et al. (2000) proposed modifications to this model which are presented here.

Firstly, the conductivity k in (3.5) comprises two parts

$$k = k_o + k_c \tag{3.7}$$

in which k_o is the conductivity of the uncracked material and k_c is a contribution due to

the effect of cracking. The calculation of the material conductivity k_o is discussed later in this section. The following cubic law is used for including the effect of cracking on the conductivity as proposed by Witherspoon et al. (1980)

$$k_c = \begin{cases} \xi \dfrac{\rho g}{\mu} \dfrac{\bar{w}_c^3}{12h} \kappa_r & \text{if } \bar{w}_c < \bar{w}_{c,max} \\ \xi \dfrac{\rho g}{\mu} \dfrac{\bar{w}_{c,max}^3}{12h} \kappa_r & \text{if } \bar{w}_c \geq \bar{w}_{c,max} \end{cases} \tag{3.8}$$

in which ξ is a factor taking into account the crack tortuosity, μ is the absolute (dynamic) viscosity of water, $\bar{w}_c$ is the equivalent crack opening of the mechanical lattice element, κ_r is the relative conductivity and $\bar{w}_{c,max}$ is the maximum equivalent crack opening. The equivalent crack opening in an element is taken as $\bar{w}_c = \sqrt{w_{cn}^2 + w_{cs}^2}$ where w_{cn} and w_{cs} are the crack opening in the normal and shear directions respectively. It is important to consider both the normal and the shear components of the crack in order to capture correctly mode I, mode II and mixed mode fracture. This is one of the key features involved in the coupling of mechanical and transport models. In (3.7) k_o is defined as the hydraulic conductivity of the uncracked material as

$$k_o = \begin{cases} \dfrac{\rho g \kappa_i}{\mu} \kappa_r & \text{if } P_c > P_{c(aev)} \\ \dfrac{\rho g \kappa_i}{\mu} & \text{if } P_c \leq P_{c(aev)} \end{cases} \tag{3.9}$$

where κ_i is the intrinsic conductivity of the material, $P_{c(aev)}$ is the air entry value of the capillary pressure that separates saturated $\left(P_c < P_{c(aev)}\right)$ and unsaturated states $\left(P_c > P_{c(aev)}\right)$. Figure 3.12 below shows an idealised diagram of saturated and unsaturated conditions. When a material is fully saturated, capillary pressure $P_c \leq P_{c(aev)}$, the capacity is zero (assuming that any changes in porosity are ignored) and the conductivity is at a maximum. However, when the material is unsaturated, $P_c > P_{c(aev)}$, the capacity is non-zero and the conductivity reduces with increasing P_c. In work presented later in this document, the term P_f is introduced. This is the term used when the material is fully saturated, i.e. when the capillary pressure $P_c \leq P_{c(aev)}$.

An empirical expression for the relative conductivity κ_r is given by Vogel et al. (2000) as

$$\kappa_r = \sqrt{S_e} \left(\frac{1 - \left[1 - \left(\frac{\theta_s - \theta_r}{\theta_m - \theta_r} S_e \right)^{1/m} \right]^m}{1 - \left[1 - \left(\frac{\theta_s - \theta_r}{\theta_m - \theta_r} \right)^{1/m} \right]^m} \right)^2 \tag{3.10}$$

where S_e is the effective degree of saturation (varying between zero and one when P_c tends to

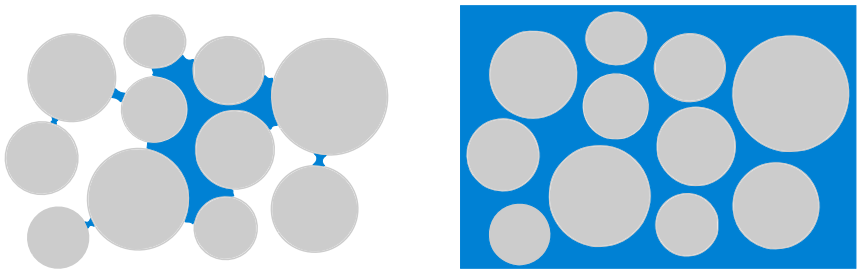

(a) (b)

Figure 3.12: Degree of saturation: (a) unsaturated and (b) fully saturated.

infinity and $P_{c(aev)}$ respectively), θ_s is the saturated water content which is the water content when the material si fully saturated, θ_r is the residual water content and is the water content of the material when it is unsaturated and θ_m is a model parameter. Equation (3.10) is based on the assumption of a non-deforming material, or that the material is at least incompressible (i.e. there is no change in porosity). Equation (3.10) is valid for use in materials such as concrete, as it is porous materials and is less compressible than soils for which this equation is used. According to Vogel et al. (2000), the effective degree of saturation S_e can be estimated from the following empirical expression for the water retention curve

$$S_e = \frac{\theta_m - \theta_r}{\theta_s - \theta_r}\left(1 + \left(\frac{P_c}{a}\right)^{\frac{1}{1-m}}\right)^{-m} \tag{3.11}$$

where m and a are model parameters. If $\theta_m = \theta_s$, (3.10) reduces to the relative conductivity expression originally proposed by van Genuchten as

$$\kappa_R = \sqrt{S_e}\left(1 - \left(1 - S_e^{1/m}\right)^m\right)^2 \tag{3.12}$$

Figure 3.13 shows a schematic diagram of the change in conductivity k_o with respect to the capillary pressure P_c for the modified and original van Genuchten model. At the point when $P_c = P_{c(aev)}$, the material is saturated and the relative conductivity κ_r equals 1.

Air breaks into a fully saturated material when the capillary pressure exceeds $P_{c(aev)}$. When the capillary pressure falls below $P_{c(aev)}$, water penetrates all of the pores. This air entry value is calculated by imposing $S_e = 1$ in (3.11), which leads to

$$P_{c(aev)} = a\left(\left(\frac{\theta_m - \theta_r}{\theta_s - \theta_r}\right)^{1/m} - 1\right)^{1-m} \tag{3.13}$$

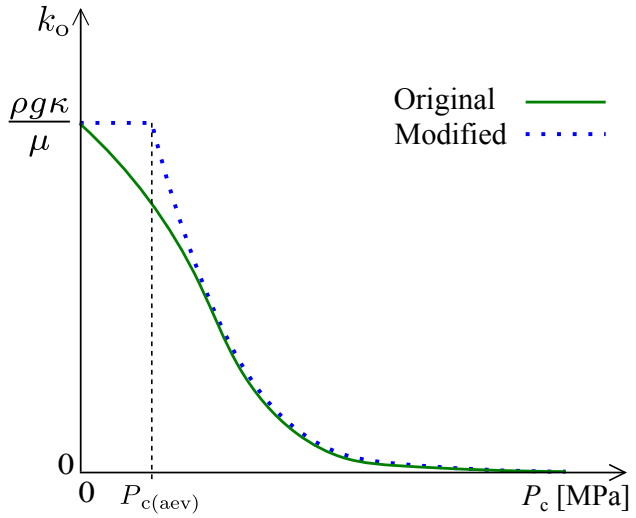

Figure 3.13: Material conductivity k_o versus capillary pressure P_c.

Figure 3.14 shows the effective degree of saturation versus capillary pressure for both the original and modified versions of van Genuchten model. The original version is displayed as a thick green line. With the modified version, $\theta_m > \theta_s$, a horizontal cut-off line at $S_e = 1$ is introduced (dotted line in Figure 3.14) to avoid values of effective degree of saturation greater than one. This line intersects the modified van Genuchten graph (3.11) at $P_c = P_{c(aev)}$.

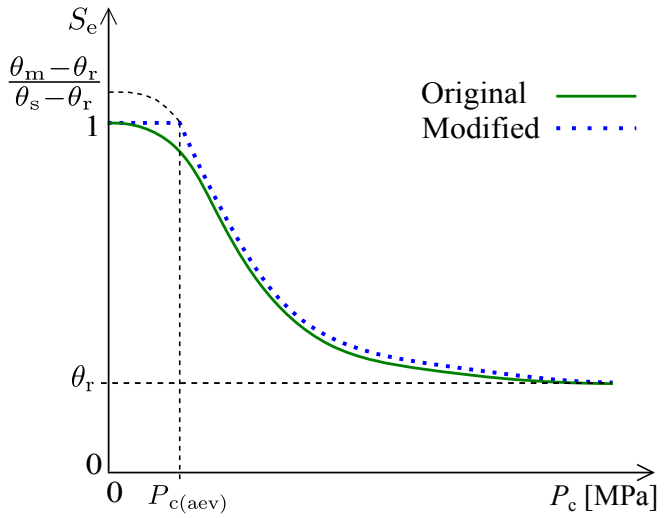

Figure 3.14: Effective degree of saturation S_e versus capillary pressure P_c.

The other parameter required is the capacity of the material c as defined in (3.6). Figure 3.15 shows a schematic diagram of the relationship between the capacity c and the capillary pressure P_c for both the modified and original van Genuchten model. Once $P_{c(aev)}$ is reached,

the material is completely saturated and the capacity becomes zero.

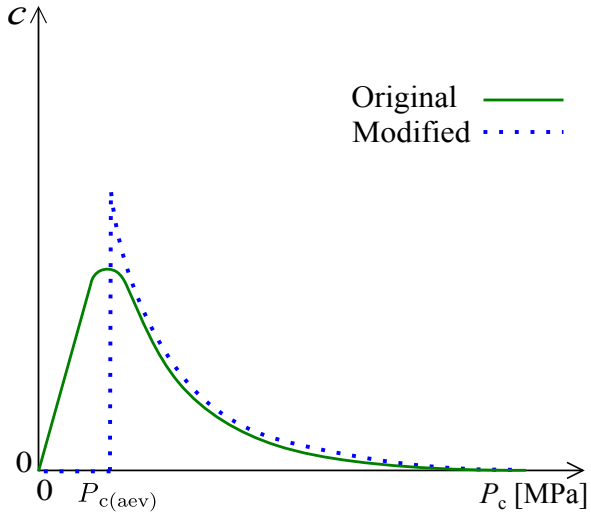

Figure 3.15: Capacity c versus capillary pressure P_c.

The relationship between the water content θ and effective degree of saturation S_e is defined by (van Genuchten, 1980) as

$$\theta = \begin{cases} S_e(\theta_s - \theta_r) + \theta_r & \text{if } P_c > P_{c(aev)} \\ \theta_s & \text{if } P_c \leq P_{c(aev)} \end{cases} \tag{3.14}$$

Therefore, the capacity c given in (3.2) for unsaturated conditions $\left(P_c > P_{c(aev)}\right)$ can be expressed as

$$c = -\frac{\partial S_e}{\partial P_c}\rho(\theta_s - \theta_r) \tag{3.15}$$

An investigation into the the influence of the parameters a and m on both the relative conductivity κ_r and the capacity c was undertaken and the results are presented in Figures 3.16 to 3.19. For all cases, the values of θ_s, θ_r and θ_m were chosen as 0.380, 0.068 and 0.3803 respectively. These values correspond to those used in Vogel and Cislerova (1988). The value of $P_{c(aev)}$ is then dependent on the parameters a and m (see (3.13)). Thus, the corresponding $P_{c(aev)}$ values are calculated. Firstly the influence of the parameter a was investigated. Here, a constant value of $m = 0.08$ and five different values of a were investigated ranging from 1×10^{-4} MPa to 1 MPa. In this work, the value of relative conductivity in (3.10) depends only on the value of the effective degree of saturation in (3.11), which in turn depends on the

parameter a. In Figure 3.16, for a constant capillary pressure of $P_c = 0.01\,\text{MPa}$, the corresponding relative conductivity κ_r is indicated with an $\times$ symbol. These points on the graph indicate that with a decreasing value a, the effective degree of saturation for a corresponding capillary pressure reduces. In Section 4.2, an a value of $0.0123\,\text{MPa}$ is used for a soil material, whereas in Section 5 $a = 18.6237\,\text{MPa}$ for concrete as determined by Baroghel-Bouny et al. (1999).

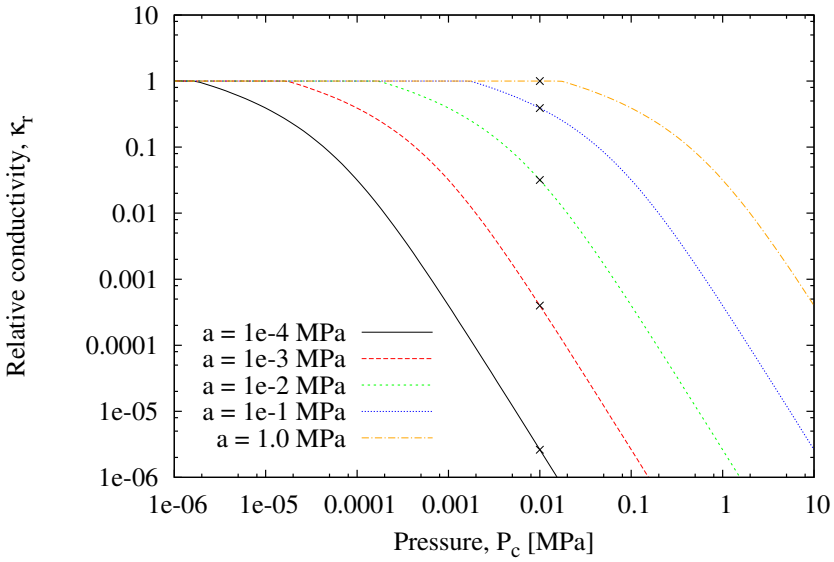

Figure 3.16: Effect of parameter a on the relative conductivity of a material.

The parameter a also strongly influences the capacity curve of a material (Figure 3.17). The capacity equals zero when the material is fully saturated.

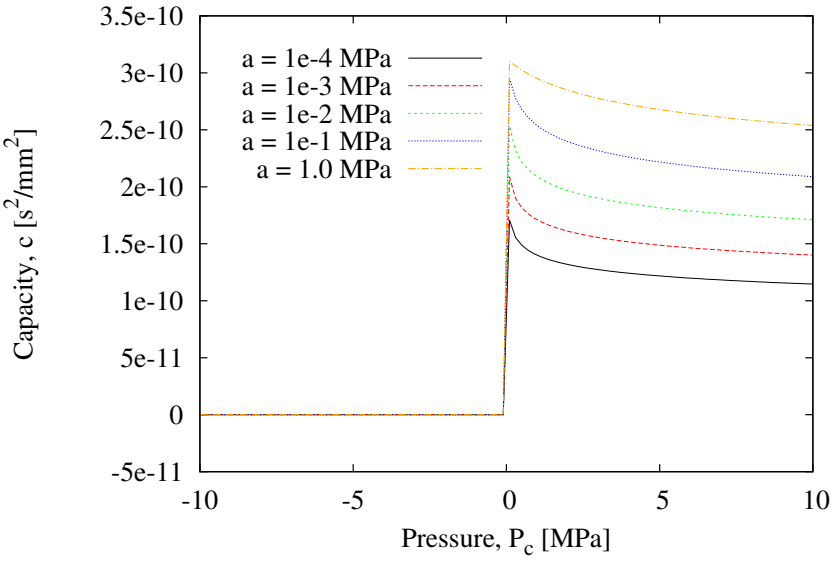

Figure 3.17: Effect of parameter a on the capacity of a material.

Figures 3.18 and 3.19 show the effect of the model parameter m on the corresponding relative conductivity κ_r and capacity c. In this case, the value of a remained constant at 0.01 MPa and five values of m ranging between 0.0001 and 0.9 were investigated. The parameter m has a very strong influence on the shape of the resulting relative conductivity curves. A much steeper curve is obtained when a value of $m = 0.9$ is used compared to when the value of m is closer to 0.0001. Considering a capillary pressure of $P_c = 0.01$ MPa, the corresponding relative conductivities are indicated with an $\times$ symbol in Figure 3.18. In this case, the influence of m on the relative conductivity is not very clear. As the value of m increases, the curve becomes steeper.

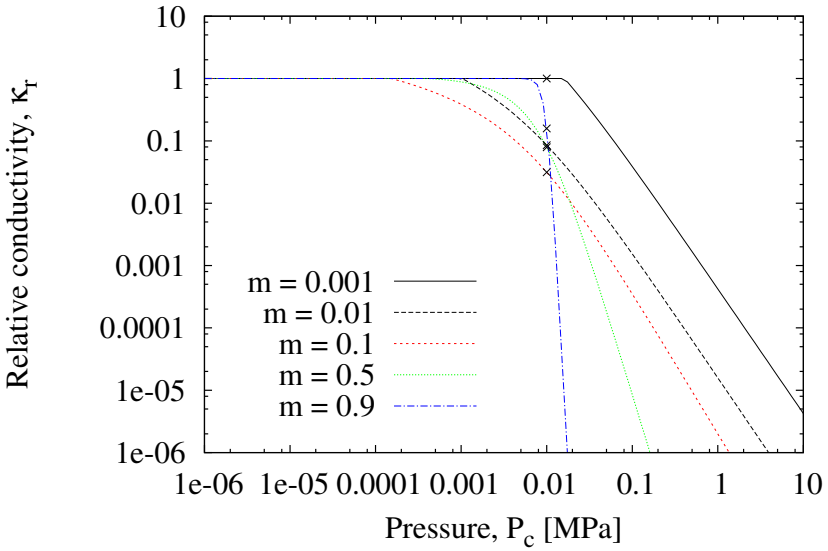

Figure 3.18: Effect of parameter m on the relative conductivity of a material.

The influence of m on the capacity c is shown in Figure 3.19. For smaller values of m, there is a strong influence resulting shape of the capacity curves. However, as the value of m approaches 1, the influence reduces. Not only does the peak value of the capacity reduce, but the slope of the curves also changes with the values of m. As the value of m increases, the capacity of the material decreases. In Section 4.2, a m value of 0.0826 is used for a soil material, whereas in Section 5, $m = 0.4396\,\text{MPa}$ for concrete as determined by Baroghel-Bouny et al. (1999).

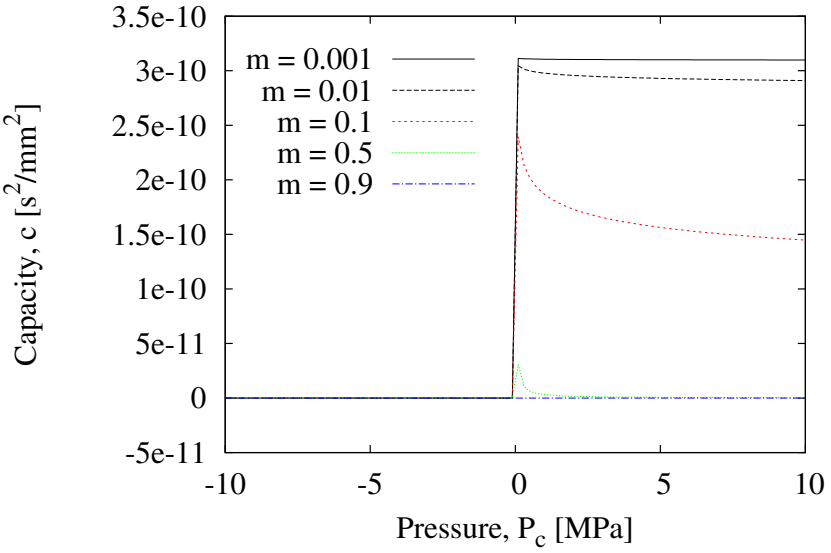

Figure 3.19: Effect of parameter m on the capacity of a material.

3.2.4 Model parameters

For saturated conditions, the following input parameters are required; intrinsic conductivity κ_i, density ρ, viscosity μ, tortuosity factor ξ, maximum equivalent crack opening $\bar{w}_{c,max}$ and gravity g. Calibration of the values of intrinsic conductivity κ_i and maximum equivalent crack opening $\bar{w}_{c,max}$ is required when running the model. However, values for all other parameters can be found in the literature.

In addition to the parameters listed above, the following parameters are required for an unsaturated analysis; residual water content θ_r, saturated water content θ_s and the model parameters θ_m, m and a.

3.3 Mechanical Model

This section is divided into three sub-sections. Firstly, the differential equation for the mechanical model is presented and the approximation of this differential equation by discrete lattice elements is discussed. Finally, the constitutive laws used in the model are presented.

3.3.1 Differential equation

Gradients of stress are governed by the conditions of static equilibrium, therefore the stresses cannot change arbitrarily between two points, or the material between these points may no longer be in equilibrium. In order to maintain equilibrium, the integrated value of a surface traction over the surface of an arbitrary volume element dV within the material must be equal to zero.

$$0 = \int_{\mathrm{A}} \mathbf{T} \mathrm{d}A = \int_{\mathrm{A}} \boldsymbol{\sigma} \tilde{\mathbf{n}} \mathrm{d}A \tag{3.16}$$

where A is the surface area, $\mathbf{T}$ is the traction vector, $\boldsymbol{\sigma}$ is the stress tensor and $\tilde{\mathbf{n}}$ is the vector of direction cosines. Assuming that no additional forces act on a body, such as gravity or centripetal forces, (3.16) can be transformed into a volume integral using Gauss' divergence theorem resulting in

$$\int_{\mathrm{V}} \nabla \boldsymbol{\sigma} \mathrm{d}V = 0 \tag{3.17}$$

As the volume is arbitrary, the intergrand has to equal zero. Thus

$$\nabla \boldsymbol{\sigma} = 0 \tag{3.18}$$

3.3.2 Discrete equation

Several researchers (Sukumar, 2003, Hüttig and Stemmer, 2008) have discretised (3.18) using the finite volume method. On the structural level, the forces are related to the stiffness and displacements as follows

$$\mathbf{f}_{\mathrm{e}} = \mathbf{K}\mathbf{u}_{\mathrm{e}} \tag{3.19}$$

where $\mathbf{f}_{\mathrm{e}} = \left\{ f_{\mathrm{u}1}, f_{\mathrm{v}1}, f_{\phi 1}, f_{\mathrm{u}2}, f_{\mathrm{v}2}, f_{\phi 2}, \right\}^T$ is the force vector, $\mathbf{K}$ is the stiffness matrix and $\mathbf{u}_{\mathrm{e}} = \{u_1, v_1, \phi_1, u_2, v_2, \phi_2\}^T$ is the vector of displacements. The degrees of freedom of lattice elements are related to the local displacements at the point C which is located at the centre of the middle cross-section of the element (see Figure 3.20).

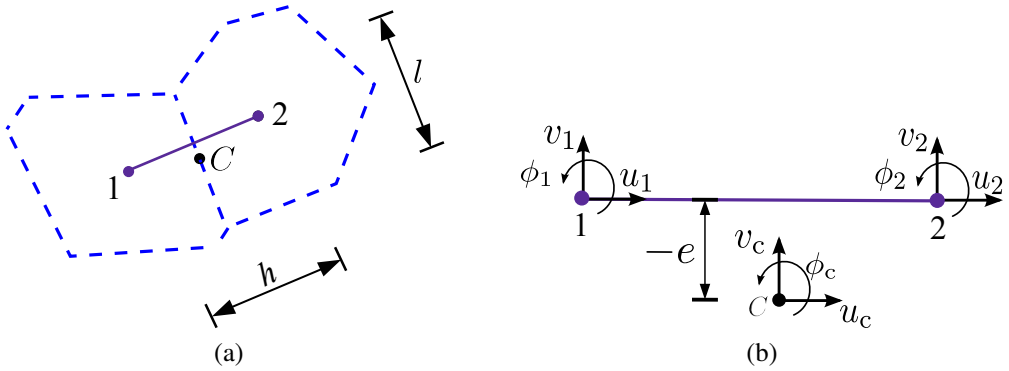

Figure 3.20: (a) Mechanical lattice element, (b) Mechanical lattice element in the local coordinate system (Grassl and Jirásek, 2010).

The relationship between the displacement discontinuities at the point C and the degrees of freedom at the nodes is

$$\mathbf{u}_c = \mathbf{B}\mathbf{u}_e \tag{3.20}$$

in which

$$\mathbf{B} = \frac{1}{h}\begin{bmatrix} -1 & 0 & e & 1 & 0 & -e \\ 0 & -1 & -\frac{h}{2} & 0 & 1 & \frac{h}{2} \\ 0 & 0 & -\frac{l^2}{\sqrt{12}h} & 0 & 0 & \frac{l^2}{\sqrt{12}h} \end{bmatrix} \tag{3.21}$$

where h is the length of the mechanical element and e is the eccentricity of the midpoint C with respect to the element axis. If C is on the left hand side of the element when viewed from node 1, e is positive otherwise e is negative. The stiffness matrix of the mechanical element is

$$\mathbf{K} = \frac{A}{h}\mathbf{B}^T\mathbf{D}\mathbf{B} \tag{3.22}$$

where $A = lt$ is the cross-sectional area of the element, in which l is the length of the cross-section and t is the out of plane thickness of the element assuming a rectangular cross-section and $\mathbf{D}$ is the material stiffness matrix. The various stiffnesses of an element are functions of the cross-sectional area of the element (Figure 3.20). The element stiffness (3.22) is calculated in terms of the local coordinate system and should be transformed to the global coordinate system using the appropriate rotation matrix.

3.3.3 Constitutive models

The inelastic response of the lattice element is described by an isotropic damage approach, which corresponds to a continuous reduction of the element's stiffness (Grassl and Jirásek,

2010). At the constitutive level, the stress of the mechanical model which enters the equilibrium condition is split into two parts; an effective stress carried by the solid and the fluid pressure in the pores. This follows Biot's theory of porous solids (Biot, 1941). It should be noted that this assumption is only valid for a saturated material. The mechanical effective stress is defined as

$$\sigma = \sigma^{\mathrm{m}} + b\sigma^{\mathrm{f}} \tag{3.23}$$

where $\sigma = \left\{\sigma_{\mathrm{n}}, \sigma_{\mathrm{s}}, \sigma_{\phi}\right\}^{T}$ is the stress vector (comprising normal, shear and rotational stresses), $\sigma^{\mathrm{m}} = \left\{\sigma_{\mathrm{n}}^{\mathrm{m}}, \sigma_{\mathrm{s}}^{\mathrm{m}}, \sigma_{\phi}^{\mathrm{m}}\right\}^{T}$ is the mechanical effective stress vector, b is Biot's coefficient ranging from zero to 1 and $\sigma^{\mathrm{f}} = \{P_{\mathrm{c}}, 0, 0\}^{T}$. The rotational stress σ_{ϕ} comes from the rotational degree of freedom at the mechancical nodes. An isotropic damage model is used for relating the effective stress with the strain. Here, the inelastic response of an element corresponds to a continuous reduction of the element's stiffness. The stress-strain law is

$$\sigma^{\mathrm{m}} = (1-\omega)\,\mathbf{D}\varepsilon \tag{3.24}$$

in which ω is a damage parameter, $\mathbf{D}$ is the elastic stiffness matrix and $\varepsilon = \left\{\varepsilon_{\mathrm{n}}, \varepsilon_{\mathrm{s}}, \varepsilon_{\phi}\right\}^{T}$ is the strain vector (comprising of normal, shear and rotational strains). The displacement discontinuities $\mathbf{u}_{\mathrm{c}}$ at the point C are transformed into strains ε by

$$\varepsilon = \frac{\mathbf{u}_{\mathrm{c}}}{h} \tag{3.25}$$

The elastic stiffness matrix $\mathbf{D}$ is defined as

$$\mathbf{D} = \begin{pmatrix} E & 0 & 0 \\ 0 & \gamma E & 0 \\ 0 & 0 & E \end{pmatrix} \tag{3.26}$$

where E and γ model parameters that are used to relate the continuum properties of the specimen to the local properties of the lattice element (Griffith and Mustoe, 2001). E and γ are calculated as

$$\gamma = \frac{1-3\upsilon}{\upsilon+1} \tag{3.27}$$

and

$$E = \frac{E_{\mathrm{c}}}{1-\upsilon} \tag{3.28}$$

Here, υ is Poisson's ratio and E_{c} is the Young's modulus of the continuum. Equations (3.27) and (3.28) are valid for plane stress analysis and a regular lattice. As an irregular mesh is used in this work, (3.27) and (3.28) are only approximations. Section 6, highlights the effect of different Poisson's ratio values on the resulting displacement curves. It is seen that

when a Poisson's ratio of 0 is used, there is excellent agreement between the numerical and analytical results. However, as the value of the Poisson's ration increases, the agreement between the numerical and analytical results reduces slightly. This highlights that equations (3.27) and (3.28) are only approximations.

The damage parameter ω in (3.24) is a function of a history variable κ which is determined by the loading function

$$f(\varepsilon, \kappa) = \varepsilon_{\text{eq}}(\varepsilon) - \kappa \tag{3.29}$$

and the loading - unloading conditions

$$f \leq 0, \quad \dot{\kappa} \geq 0, \quad \dot{\kappa} f = 0 \tag{3.30}$$

The equivalent strain ε_{eq} in (3.29) is defined as

$$\varepsilon_{\text{eq}}(\varepsilon_{\text{n}}, \varepsilon_{\text{s}}) = \frac{1}{2}\varepsilon_0(1-c) + \sqrt{\left(\frac{1}{2}\varepsilon_0(c-1) + \varepsilon_{\text{n}}\right)^2 + \frac{c\gamma^2\varepsilon_{\text{s}}^2}{q^2}} \tag{3.31}$$

in which ε_0 is the strain threshold and c and q are model parameters directly related to the strength of the lattice elements. At the point when κ is equal to ε_0, the strength envelope is reached and (3.31) leads to an elliptical stress envelope in the mechanical effective stress space (Figure 3.21). In the case of pure tension, the mechanical stress is limited by the tensile strength $f_{\text{t}} = E\varepsilon_0$. For pure shear and pure compression, the mechanical stresses are limited by $f_{\text{q}} = qf_{\text{t}}$ and $f_{\text{c}} = cf_{\text{t}}$ respectively (Figure 3.21).

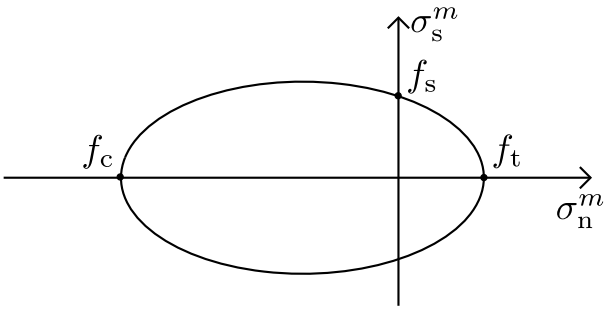

Figure 3.21: Elliptical strength envelope.

An exponential softening curve is used to describe the stress crack opening part of the model.

The softening curve for pure tension is defined as

$$\sigma_{\mathrm{n}}^{\mathrm{m}} = f_{\mathrm{t}} \exp(-\frac{w_{\mathrm{c}}}{w_{\mathrm{f}}}) \tag{3.32}$$

where $w_{\mathrm{c}} = \omega h \varepsilon_{\mathrm{n}}$ is considered as the crack opening under monotonic loading and w_{f} is the initial slope of the curve (Figure 3.22).

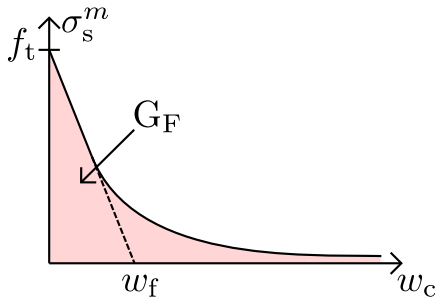

Figure 3.22: Stress-crack opening curve.

Parameter w_{f} determines the initial slope of the stress-crack opening curve and it is given as

$$w_{\mathrm{f}} = \frac{G_{\mathrm{F}}}{f_{\mathrm{t}}} \tag{3.33}$$

where $\mathrm{G_F}$ is the fracture energy and is shown as the shaded area under the curve in Figure 3.22. The damage parameter ω is determined by deriving an equation for ω under the assumption of pure tension. Equation (3.24), in pure tension, can be expressed as

$$\sigma_{\mathrm{n}}^{\mathrm{m}} = (1-\omega) E \varepsilon_{\mathrm{n}} \tag{3.34}$$

Comparing the right-hand sides of (3.32) and (3.34), and replacing ε_{n} with κ, the following equation is obtained

$$(1-\omega)\,\kappa = \varepsilon_0 \exp\left(-\frac{\omega h \kappa}{w_{\mathrm{f}}}\right)$$

from which the damage parameter ω can be determined iteratively using, for example, a Newton-Raphson method. Finally, Biot's coefficient b in (3.23) is used to determine the amount of fluid pressure that must be added to the mechanical effective stress to give the total stresses.

3.3.4 Model parameters

For an elastic mechanical analysis, the parameters E and γ are required. For an inelastic analysis, the following parameters are also required; ε_0, c, q and w_f. In addition, the Biot coefficient b is also required for the model, as equilibrium is expressed in terms of total stresses (3.23). Unless b is zero, a coupled analysis will be required, so that the value of P_c can be provided from the transport model.

3.4 Coupled Approach

Section 2.1 of this thesis discussed the aspects of coupling that can be considered in a coupled transport-mechanical approach. In this work, there are two aspects of coupling that are considered. In the first instance, the fluid pressure P_f from the transport model is used in the mechanical model to link the total stresses and the mechanical effective stresses, unless the Biot coefficient $b = 0$. Also, the influence of the mechanical model on the transport properties is considered by an increase in conductivity due to cracking. The effect of cracking on the transport properties such as porosity and capacity is not considered in this work. The mechanical properties such as strength, stiffness, etc, are governed entirely by the mechanical effective stress (which will be influenced by the fluid pressure P_f) and are independent of variables coming from the transport model such as the degree of saturation.

A staggered approach is used for the coupling of the two models. Each model (transport and mechanical) is solved independently at each time step in separate domains (Figure 3.23). The required coupling information is exchanged at the beginning of each step. Take for example the fluid pressure calculated at step i. This value will enter the mechanical model at step $i+1$. This process continues for the complete analysis with information being exchanged between both the mechanical and transport models.

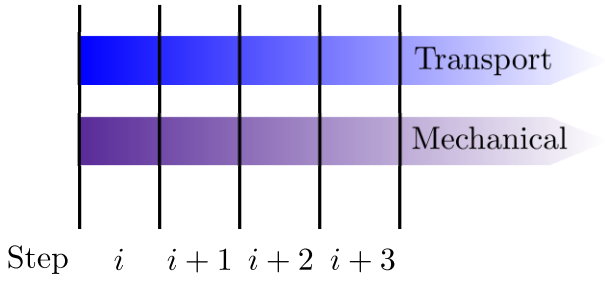

Figure 3.23: Staggered solution for coupled model.

One assumption of this coupled approach is that it is assumed that at a boundary the total normal stress and the fluid pressure are equal. This corresponds to a boundary where the only loading is due to fluid loading. In the coupled approach, there are two cases in which a boundary condition applied in one of the models influences the response of the other model. In the first case, an applied fluid pressure along a boundary can result in a force acting on the mechanical model. The alternative is to apply a mechanical displacement at the boundary and obtain from this the corresponding fluid pressure.

Along the boundary between an inclusion and the porous material, transport nodes are placed (see Figure 3.24a) and to each of these transport nodes a fluid pressure is applied as a boundary condition. Mechanical nodes are also placed along the boundary. Each of these mechanical nodes have two corresponding transport nodes from which the fluid pressure is used to calculate the mechanical load applied. Figure 3.24b shows a close up detail of the application of this type of boundary condition.

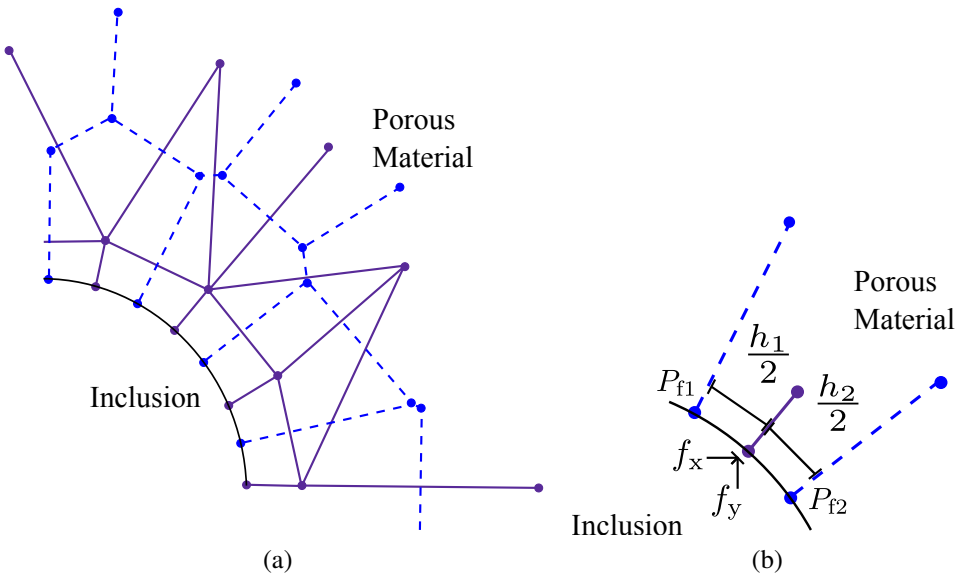

Figure 3.24: (a) Dual mesh near the interface between the inclusion and the porous material. (b) Detail showing the application of a mechanical force due to fluid pressures.

The following equation is used to determine the load applied to a mechanical node due to the application of a fluid pressure as a boundary condition in the transport model.

$$\mathbf{f} = P_{f1} h_1 \mathbf{v} + P_{f2} h_2 \mathbf{v} \tag{3.35}$$

where $\mathbf{f} = \{f_x, f_y\}^T$ is the vector of applied loads at a mechanical node due to the fluid pressure and $\mathbf{v} = \{v_x, v_y\}^T$ contains the information for splitting the radial force into the corresponding vertical and horizontal forces. The applied fluid pressure of the transport model is transformed into applied forces at each mechanical node along the boundary by firstly converting the fluid pressure into a normal force by considering the distance from the transport node to the mechanical one and the out of plane thickness of the element. Next, the radial force is broken into the corresponding normal and shear forces. Finally, these forces are then applied as a boundary condition in the mechanical model.

Analyses carried out using the alternative boundary condition are driven by a prescribed displacement applied to small mechanical elements that are placed along the interface between the inclusion and the porous material. Figure 3.25a shows a sketch of these elements along the interface.

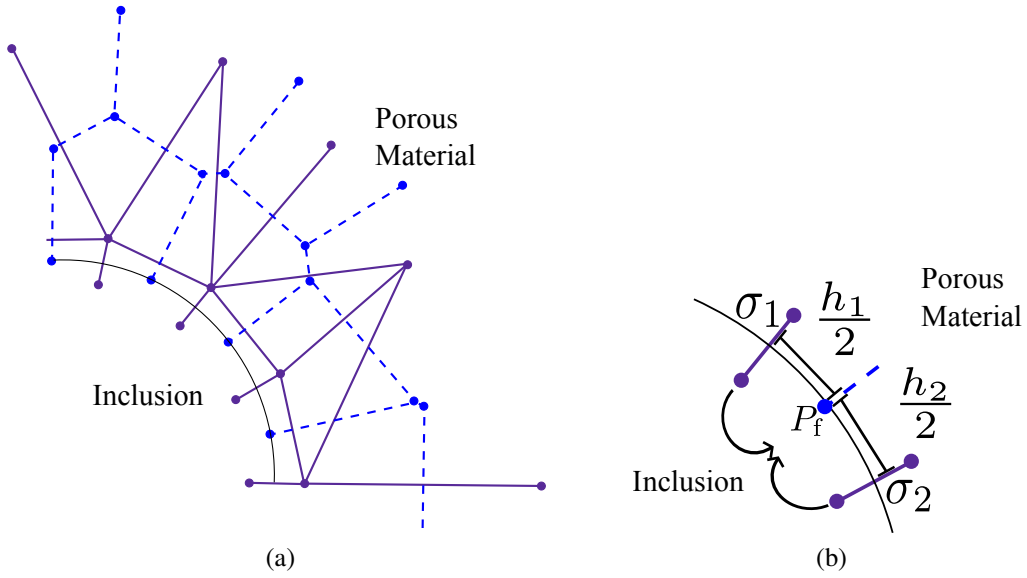

Figure 3.25: (a) Dual mesh near the interface between the inclusion and the porous material. (b) Detail showing the application of the fluid pressure due to mechanical stresses.

These elements are given a very high normal stiffness. However, their shear stiffness is very low to allow for the opening of cracks in the material near the interface. To these elements, an eigen-displacement is applied in the normal direction and is then converted to an eigenstrain. As the inclusion and the interface elements are both given very high stiffnesses, the applied eigen-displacement is equal to the total radial displacement in these elements.

The applied eigen-displacement causes a mechanical normal stress in each element. The normal mechanical stress is used to calculate the fluid pressure boundary condition in the transport model assuming that a layer of fluid separates the inclusion and the porous material (Figure 3.25b). The mechanical stress in these interface elements is converted to a boundary fluid pressure by the following equation

$$P_{\mathrm{f}} = \frac{\sigma_1^{\mathrm{m}} h_1 + \sigma_2^{\mathrm{m}} h_2}{h_1 + h_2} \tag{3.36}$$

3.5 Implementation within OOFEM

Analyses were carried out using the finite element code OOFEM (Object Orientated Finite Element Method) (Patzák and Rypl, 2012)). For the mechanical model, existing mechanical elements and constitutive laws were used. However, the constitutive laws were extended for considering the effect of fluid pressure on the mechanical effective stresses. For the transport model, flow elements were already available. However, the constitutive laws described in Section 3.2.3 were implemented by the author.

The key aspect of this work was the development of new coupling nodes that enable the exchange of information between models along the boundaries of a specimen. In this case, two types of coupling nodes were implemented that correspond to the conditions discussed in Section 3.4.

Chapter 4

Uncoupled Analyses

This chapter presents the initial work undertaken before coupling of the mechanical and transport models was enforced, in order to assess and verify each model individually. In the first part, analyses were carried out on notched concrete specimens that capture different modes of cracking using the mechanical model. An investigation of the mesh size dependence of load-crack-mouth-opening curves was carried out and the numerical results obtained were compared to experimental results reported in the literature.

In the second part of this chapter, transport analyses were carried out for a one-dimensional clay column to verify the implementation of the constitutive laws within the OOFEM software. These analyses allow for the assessment of the ability of this model for predicting moisture transport in unsaturated non-deforming porous materials. The mesh and step size dependence on the model results were also evaluated in this work.

4.1 Cracking of Concrete

Two tests were chosen to investigate the influence of mesh size on concrete fracture. In the first case, a four-point shear test of a single-edge notched specimen was analysed, as reported in Arrea and Ingraffea (1982). Next, a shear test of a double-edge notched specimen reported in Nooru-Mohamed (1992) was modelled. In both cases, these tests are characterised by curved fracture patterns.

For each fracture test, two-dimensional plane stress analyses were carried out using three different mesh sizes. A comparison of the influence of the different mesh sizes on the curved fracture pattern was carried out. A study of the effect of the randomness of the lattice elements on the fracture patterns and the load-displacement curves was also carried out for the four-point shear test simulation.

4.1.1 Single-edge notched specimen

The first simulation was the four-point shear test of a single-edge notched (SEN) beam tested by Arrea and Ingraffea (1982). The geometry of the specimen, along with the loading setup and the crack trajectories obtained in the experiments are shown in Figure 4.1. This test requires two loads to be applied to the specimen at specific loading positions along the top of the beam. This causes a crack to propagate from the top of the notch upwards towards the top of the specimen. In this work, the load was applied using indirect displacement control where the displacement was calculated as the difference of the vertical displacements at the bottom nodes on each side of the notch (referred to as the Crack-Mouth-Shear-Displacement (CMSD)) (Figure 4.1). The model parameters chosen for the lattice elements are presented in Table 4.1 and the out-of-plane thickness of the specimen is 152 mm. These values were determined based on material information reported in Jirásek and Grassl (2008) and using (3.27) and (3.28) in Section 3.3.3. If all the required parameters are not available for the specimen that is to be modelled, it is possible to calculate generic concrete material parameters based on documents such as The Model Code (FIB, 2012). The generic values determined will affect the results of any analyses undertaken. For example, the Young's modulus will affect the initial stiffness. If the value of this is determined incorrectly, then the numerical results could either overpredict or underpredict the stiffness of the specimen. The onset of cracking is influenced by the parameters ε_0, c and q (Section 3.3). The model parameter w_f is influenced by the fracture energy G_F (3.33) and effects the post cracking behaviour of the specimen. The fluid pressure P_f was assumed zero throughout the beam, therefore the Biot coefficient b is not considered in this work.

Table 4.1: Model parameters for single-edge notched shear test specimen.

ε_0	E [GPa]	γ	c	q	w_f [mm]
76.53×10^{-6}	36.58	0.3898	10.0	2.0	4.5×10^{-2}

Analyses were carried out using three different levels of mesh refinements in which the d_min values were chosen as 5 mm, 10 mm and 15 mm, corresponding to the labels Fine, Medium

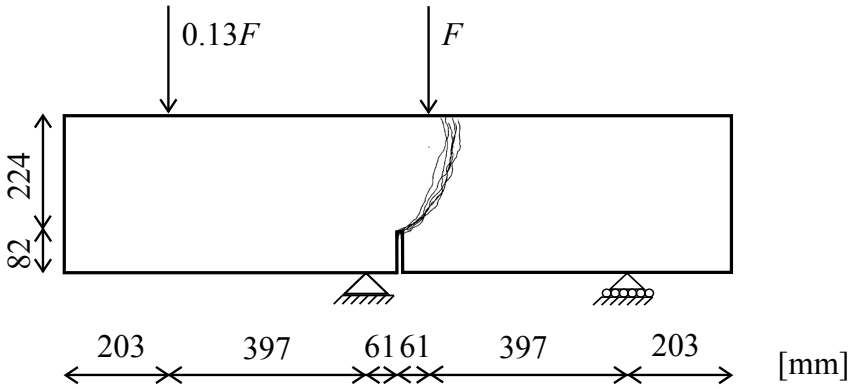

Figure 4.1: Geometry and loading for a four-point shear test of a a single-edge notched (SEN) concrete beam (Arrea and Ingraffea, 1982).

and Coarse respectively in Figure 4.3. The meshes used are shown in Figure 4.2. In each case, a very coarse mesh is specified for the outer thirds of the beam as little damage occurs in these areas.

4.1.2 Comparison between numerical and experimental results

An investigation of the effect of varying mesh refinements on the resulting load-CMSD curves was carried out in this work. A comparison between the load-CMSD curves for the three meshes and the experimental results reported in Arrea and Ingraffea (1982) is presented in Figure 4.3. For the elastic range of the load-CMSD curve, there is very good agreement between the numerical and experimental results. It can also be seen that within this range, the numerical curves obtained are independent of the mesh size used.

However, as the analyses continue and damage occurs, there is a slight dependence on the element size used in the mesh. Despite this, the numerical results continue to show good agreement with the range of experimental results, at least for the initial part of the falling branch.

Figure 4.4 shows the failure patterns obtained from the analysis. Only the area in the immediate vicinity of the crack is shown. In this figure, the blue lines super-imposed onto the meshed specimen show the fracture patterns obtained during experimental testing. The red lines show cross-sections of elements in which damage occurs at this time step. The grey lines show elements that have been damaged in a previous time step but the damage is not increasing in the present step.

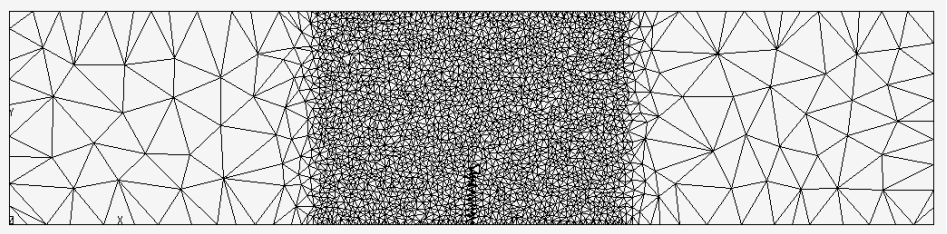

(a)

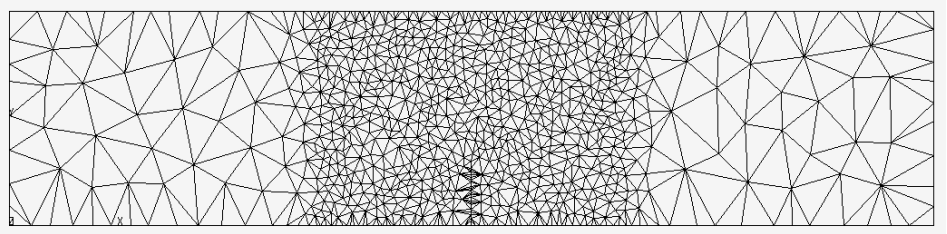

(b)

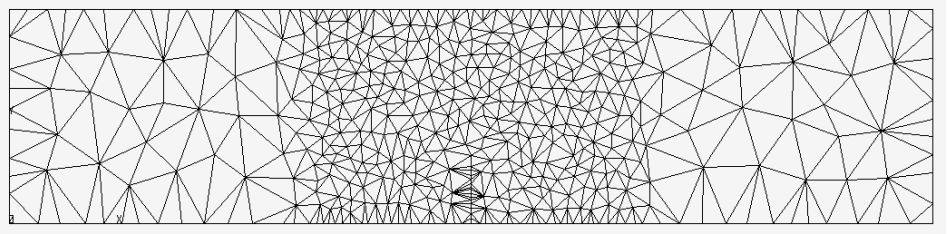

(c)

Figure 4.2: Mechanical lattices: (a) fine, (b) medium and (c) coarse.

Investigation of Figure 4.4 shows that in each case there is very good agreement between the fracture patterns obtained from the analysis and the experimental crack patterns.

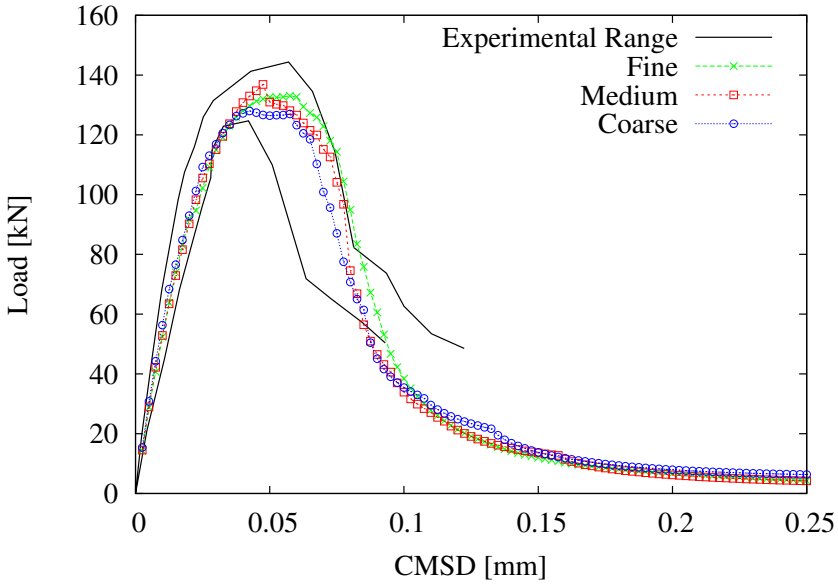

Figure 4.3: Influence of mesh refinement on the load-CMSD curves.

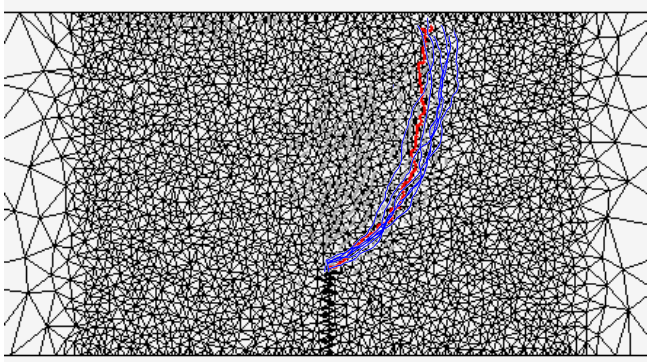

(a)

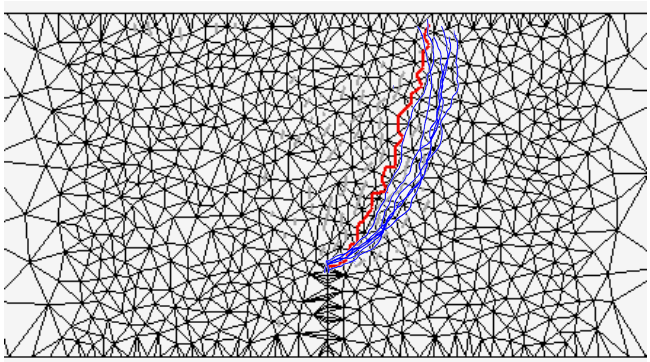

(b)

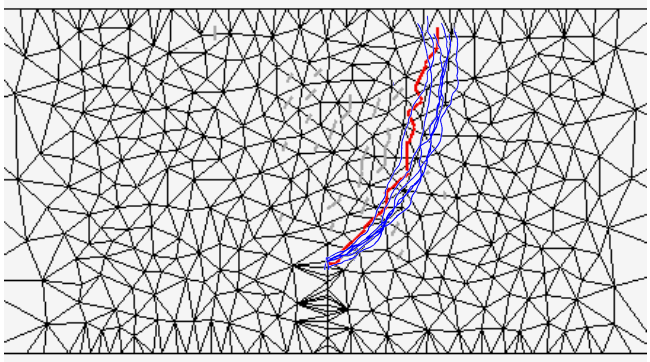

(c)

4.1.3 Investigation of dependence on mesh

A study of the effect of the randomness of the mesh on the resulting load-CMSD curves was carried out on this specimen. Two additional meshes, of the same level of mesh refinement as the medium mesh, i.e. the same $d_{\min}$ was used for generating the meshes, are presented in Section 4.5, were created and the load-CMSD curves obtained during this study are presented in Figure 4.5. The new meshes, although created using the random point generation process outlined in Section 3.1, did not vary much from mesh to mesh. Investigation of Figure 4.5 highlights that before the peak load is reached, the results are almost independent of the mesh used. As the analysis continues, there is some dependence on the randomness of the mesh used. However, towards the end of the analysis, the curves obtained using different meshes are no longer dependent of the randomness of the mesh.

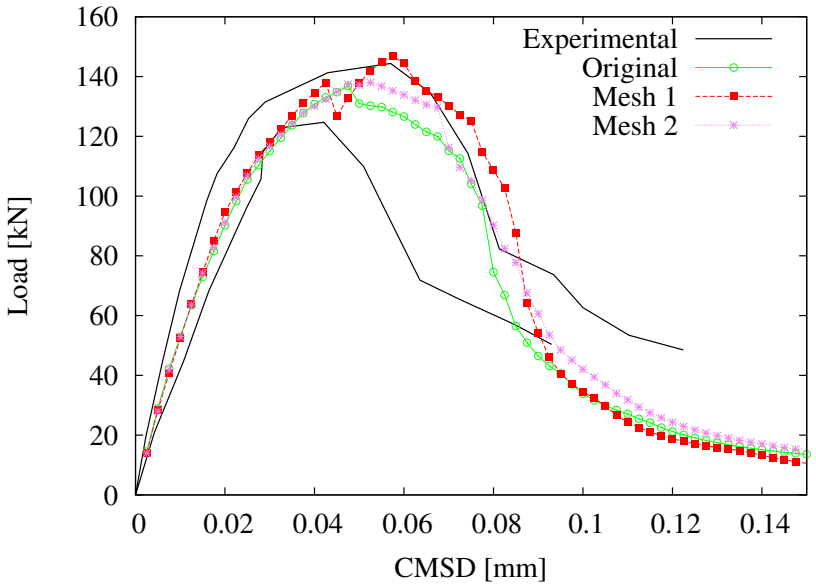

Figure 4.5: Load-CMSD curves for alternative meshes.

4.1.4 Double-edge notched specimen

In the second simulation a double-edge notched (DEN) shear test that was originally performed by Nooru-Mohamed (1992) was analysed. The geometry, experimental setup and resulting fracture patterns reported in the experimental work are presented in Figure 4.6 and the model parameters used in the analyses are shown in Table 4.2. The out-of-plane thickness of the specimen was 50 mm. The values of the parameters in Table 4.2 differ to those presented in Table 4.1, Section 4.1.1 as the material parameters reported in the literature differed. For example, the Poisson's ratio used differed, which led to a difference in the γ values.

Table 4.2: Model parameters for DEN shear test specimen.

ε_0	E [GPa]	γ	c	q	w_f [mm]
53.79×10^{-6}	36.25	0.3333	10.0	2.0	4.5×10^{-5}

These analyses are independent of the transport analysis and therefore the Biot coefficient b is not considered in this work.

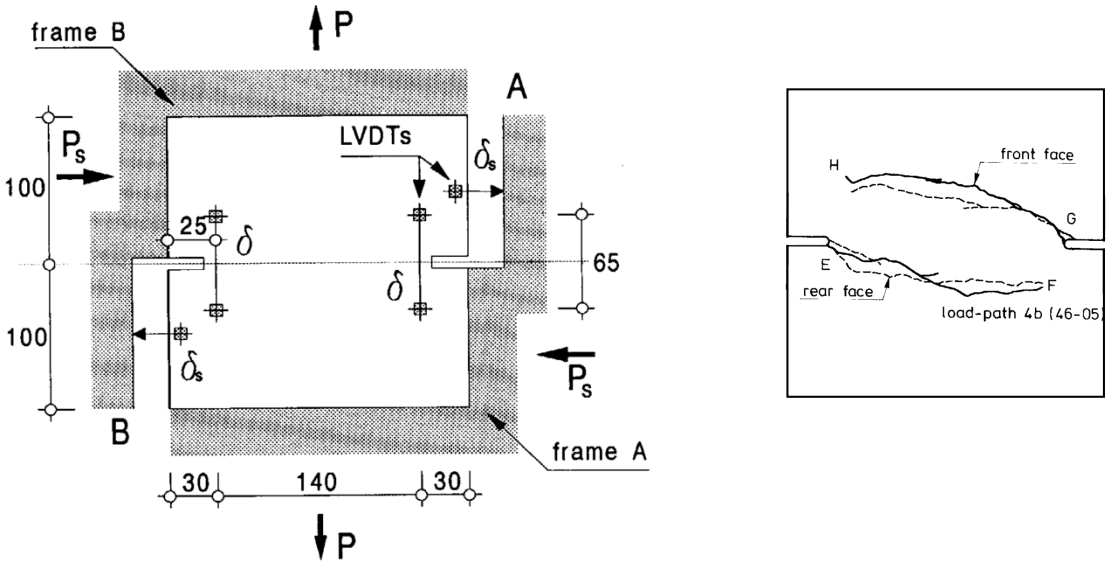

(a) (b)

Figure 4.6: Shear test of a double-edge notched (DEN) concrete beam (Nooru-Mohamed, 1992): (a) specimen geometry and loading set-up and (b) fracture patterns.

For this test, there are two stages of loading. During the first stage, the specimen is loaded by an increasing shear force, P_s, until a value of 10 kN is reached. In the second stage, this shear force is kept constant and the specimen is stretched under displacement control in the vertical direction which generates a reaction force P.

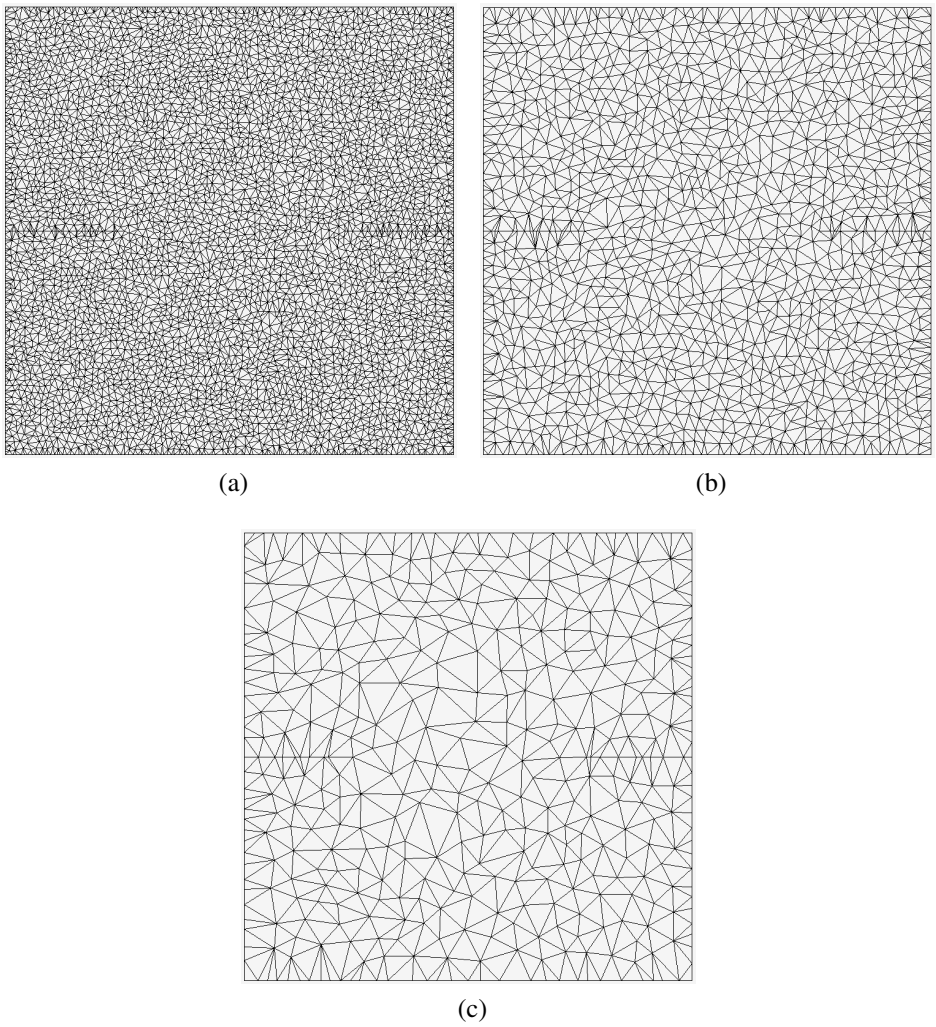

Figure 4.7: Meshes (a) fine, (b) medium and (c) coarse.

As with the previous analyses, three different levels of mesh refinements (see Figure 4.7) were used to investigate the influence of mesh size on the load-displacement curve and the fracture patterns for the DEN specimen. A comparison between the load-displacement curve for each mesh and the experimental results is shown in Figure 4.8. Reasonable agreement between the numerical and experimental results can be seen in Figure 4.8. The predicted initial stiffness is less than that measured in the experiments. It is possible that during the first part of the analysis, when the shear force is applied to the specimen, a small amount of displacement occurs which is captured in Figure 4.8. The maximum load predicted by the numerical load falls within the experimental ranges, however it occurs at a larger displacement than that reported in the experiments.

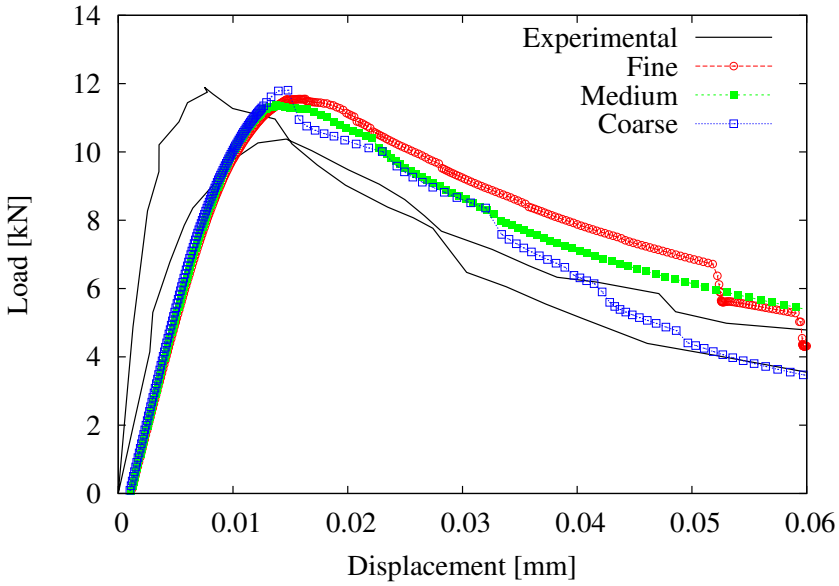

Figure 4.8: Load-displacement curves for a DEN specimen.

The crack trajectories obtained during the analyses are compared to the experimental ones in Figure 4.9. In Figure 4.9 the blue lines represent the crack patterns observed during experiments, while the red lines are the fracture patterns obtained from the numerical analyses. For all three mesh refinements, very good agreement between the numerically predicted and experimental fracture patterns is achieved. However, the fracture patterns obtained for the coarse mesh refinement do not extend as far as the experimental cracks.

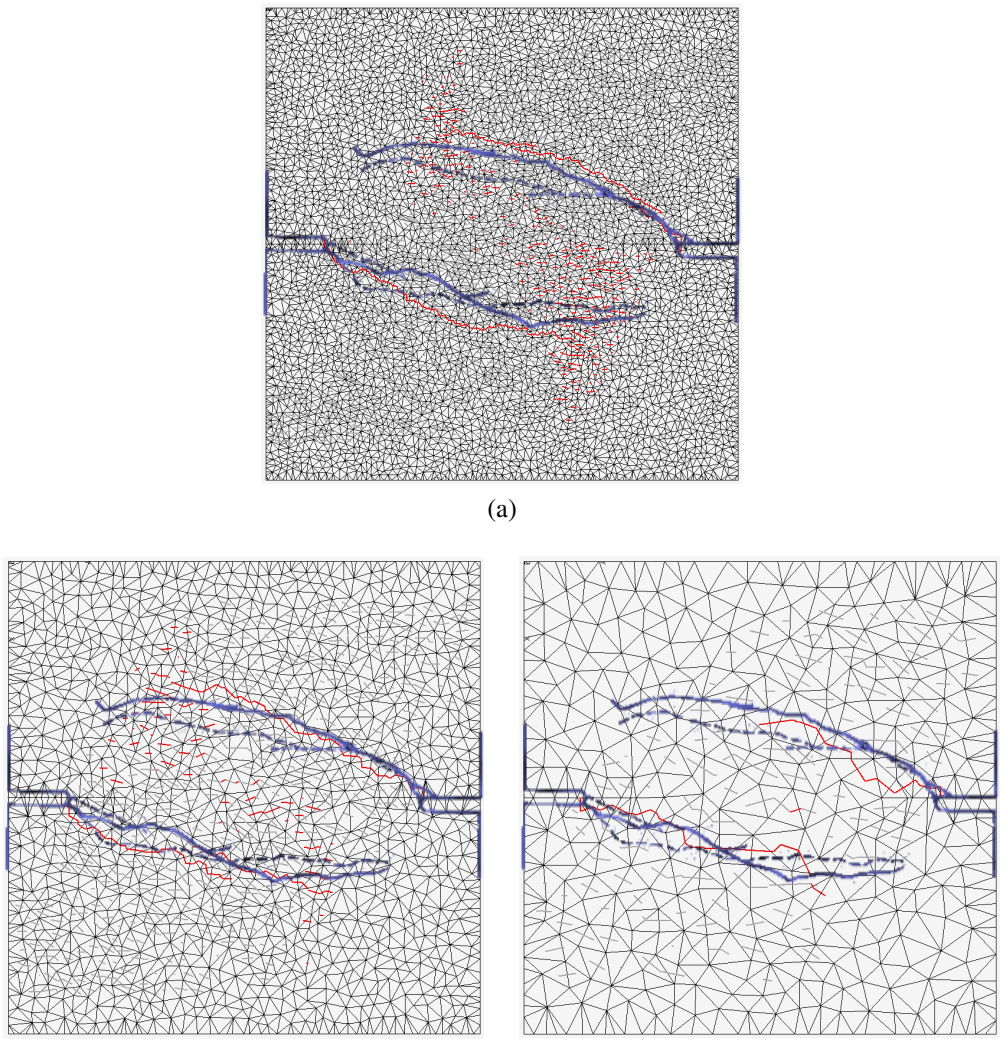

(a) (b) (c)

Figure 4.9: Comparison of numerical and experimental fracture patterns for different mesh refinements for a displacement of 0.04 mm: (a) fine, (b) medium and (c) coarse mesh.

4.2 Moisture Transport Through Unsaturated Porous Material

In the second part of the uncoupled work, an investigation of both the original and modified version of the van Genuchten model described in Section 3.2.3 was undertaken.

4.2.1 Specimen geometry and boundary conditions

Analyses were carried out on a 1000 mm tall soil column (Figure 4.10a), with initial conditions (at $t = 0$) corresponding to a hydrostatic fluid pressure distribution (no flow of water)

and an imposed fluid pressure of 0.0981 MPa (tension) at the bottom of the column (Figure 4.10b). This value of initial capillary pressure at the base of the column corresponds to an imposed pressure head of -1000 cm as specified in Vogel et al. (2000). The boundary conditions specified for the subsequent analysis, and shown in Figure 4.10c, were as follows: a zero pressure head at the bottom of the column combined with a zero flux at the top of the column, leading to infiltration of the column with water entering from the base.

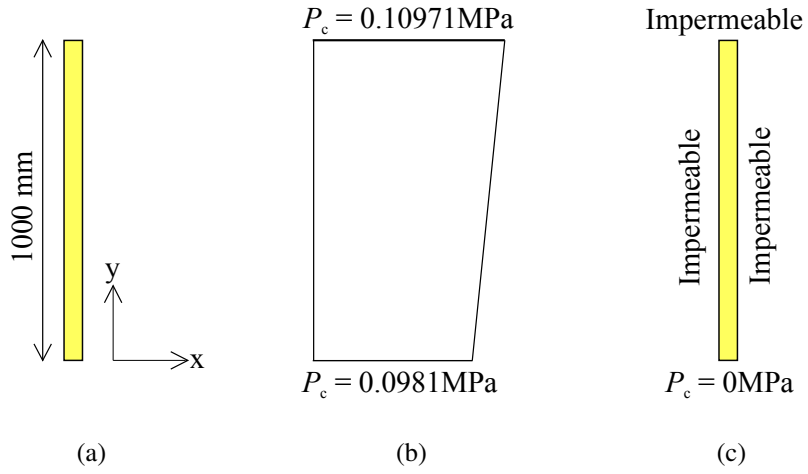

Figure 4.10: One-dimensional soil column: (a) geometry, (b) initial fluid pressure distribution at $t = 0$ and (c) boundary conditions for $t > 0$; according to (Vogel et al., 2000).

Table 4.3 below lists the values chosen for the required parameters for both the original and modified version of the van Genuchten model. These values were taken from the work carried out in Vogel et al. (2000), some of which was based on previous work carried out by Carsel and Parrish (1988). Cracking is not considered in these analyses and therefore the tortuosity factor ξ and the maximum equivalent crack width $\bar{w}_{c,max}$ are not considered in this work.

Table 4.3: Transport material parameters for soil.

θ_s	θ_r	θ_m	μ [MPa s]	κ_i [mm^2]	m	a [MPa]
0.380	0.068	0.3803	1×10^{-9}	5.6634×10^{-8}	0.0826	0.0123

Figures 4.11 to 4.13 present the corresponding variations of volumetric water content θ, wa-

ter capacity c and relative conductivity κ_R with capillary pressure P_c for both the original and modified versions of the van Genuchten model. It is important to note that the modified van Genuchten model assumes a value of θ_m that is very close to the value of θ_s, resulting in a very small air-entry capillary pressure $P_{c(aev)} = 1.962 \times 10^{-4}$ MPa (previously discussed in detail in Section 3.2.3). Therefore, it is very difficult to see any difference between the variations of volumetric water content θ with capillary pressure P_c predicted by the original and modified versions of the van Genuchten model (Figure 4.11). In Figure 4.12, when the modified version of the van Genuchten model is used and the air-entry capillary pressure $P_{c(aev)} = 1.962 \times 10^{-4}$ MPa, the specimen is regarded as fully saturated and the capacity becomes zero. Likewise, in Figure 4.13, up to the the air-entry capillary pressure, the specimen is fully saturated and therefore the relative conductivity is 1. After this point, air breaks into the specimen, causing the degree of saturation to fall and causing the relative conductivity to reduce also.

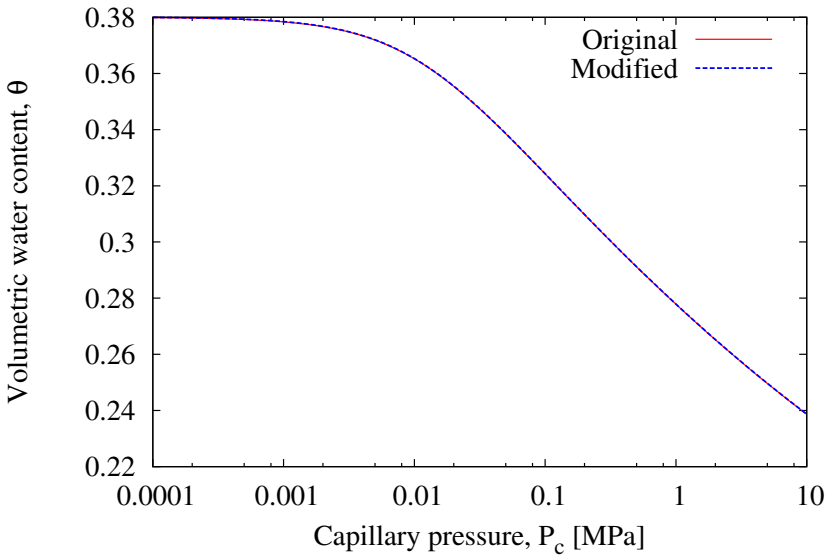

Figure 4.11: Volumetric water content versus capillary pressure.

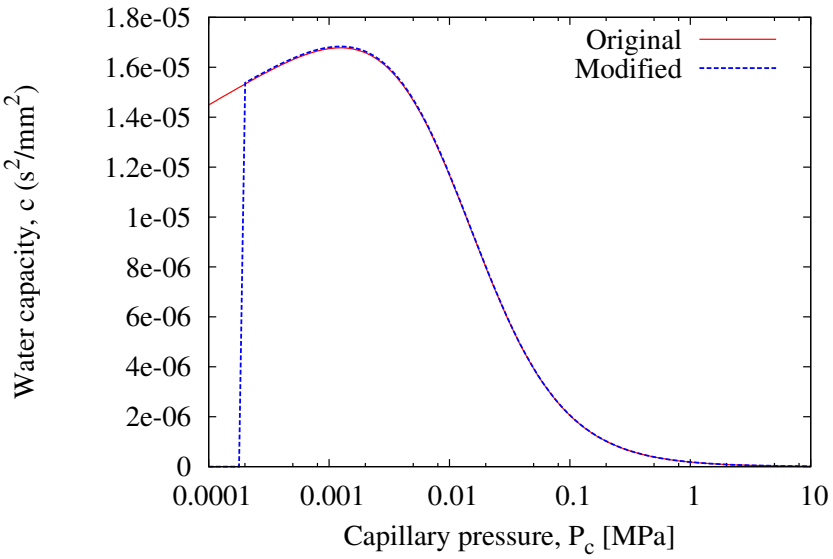

Figure 4.12: Water capacity versus capillary pressure.

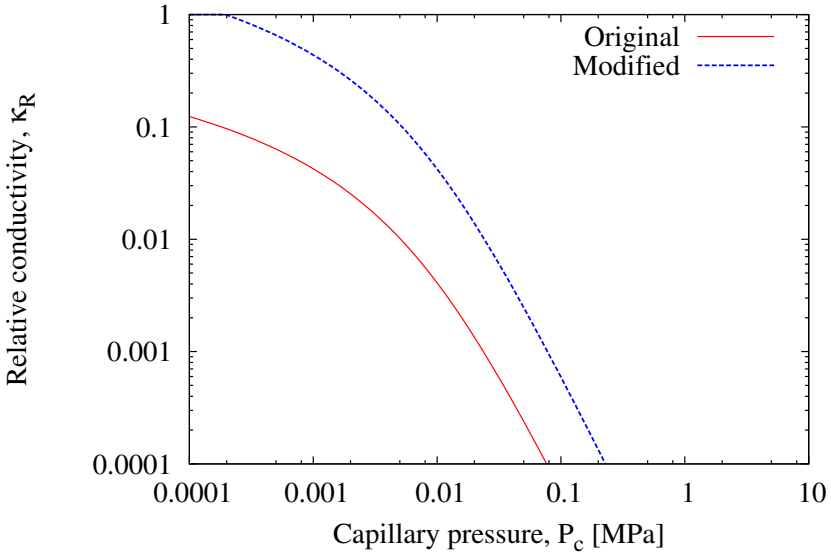

Figure 4.13: Relative conductivity versus capillary pressure.

4.2.2 Comparison of infiltration rates

Analyses were carried out using both the original and modified versions of van Genuchten's model and the results obtained were compared to those presented in Vogel et al. (2000). Vogel et al. (2000) used the one-dimensional Galerkin finite element program HYDRUS to carry out their numerical work. A comparison between the pressure distribution along

the soil column predicted by the present model and that presented by (Vogel et al., 2000) when the original version of the van Genuchten model is used is presented in Figure 4.14. Examination of Figure 4.14 highlights that the locations predicted for the wetting front the present model are slightly behind those predicted by the alternative numerical formulation presented by Vogel et al. (2000) for each time presented. However, Figure 4.15 shows that when the modified version of the van Genuchten model is used, the wetting fronts predicted by the present model are in much better agreement with those presented in Vogel et al. (2000). Furthermore, Vogel et al. (2000) noted that due to the non-linear nature of the original van Genuchten conductivity function, numerical instability problems can arise. However, the use of the modified van Genuchten model overcame these numerical problems. This is one of the reasons for choosing to use the modified version rather than the original version of the van Genuchten model.

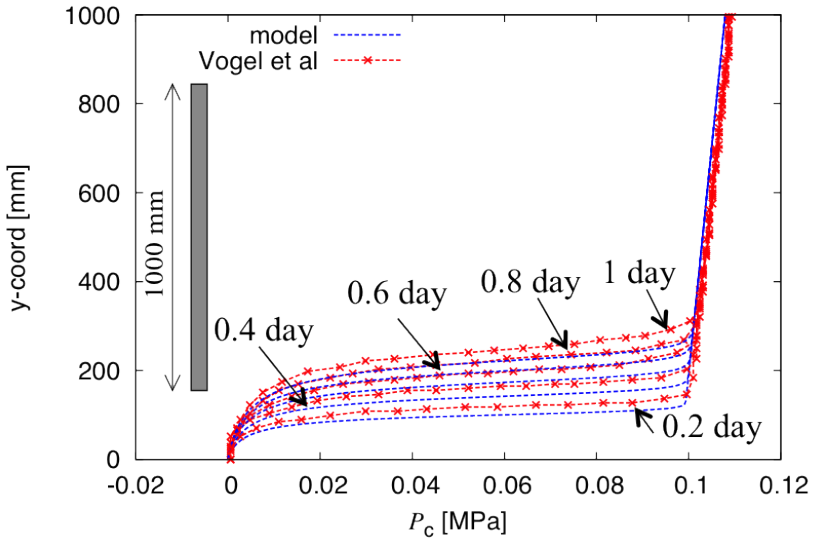

Figure 4.14: Comparison of capillary pressure distribution at different times as predicted by the present model and by Vogel et al. (2000) using the original van Genuchten model.

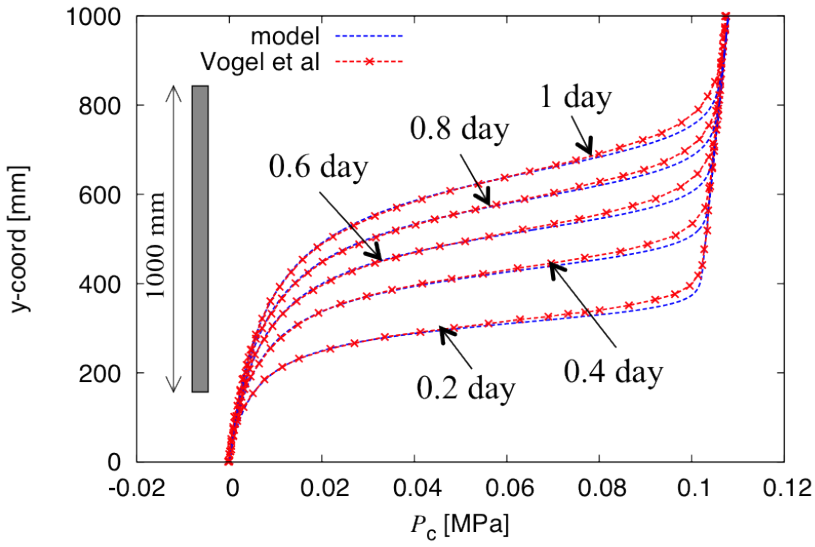

Figure 4.15: Comparison of capillary pressure distribution at different times as predicted by the present model and by Vogel et al. (2000) using the modified van Genuchten model.

4.2.3 Mesh dependence

The dependence of the predicted infiltration rates on the level of mesh refinement was also investigated as part of this work. Three different levels of mesh refinement were considered in which the element lengths were 2.5 mm, 5 mm and 10 mm. These lengths correspond to the labels Fine, Medium and Coarse respectively in Figures 4.16 and 4.17 below. The predicted infiltration rate over time, as calculated at the bottom of the soil column, for both the original and modified version of the van Genuchten models are presented in Figures 4.16 and 4.17, respectively. In both cases, very good agreement between the numerical results and the alternative numerical results presented by Vogel et al. (2000) is achieved. However, a closer inspection of Figure 4.16 shows large oscillations occurring at the early stages of the analyses. The infiltration rate also appears to be dependent on the mesh size used during the early stages of the analyses. Further investigation of these oscillations will be presented later in this section.

Figure 4.17 presents the predicted infiltration rate over time when the modified version of the

van Genuchten model is used. In this case, it appears that the oscillations are greatly reduced and the results are independent of the level of mesh refinement much earlier than when the original van Genuchten model is used.

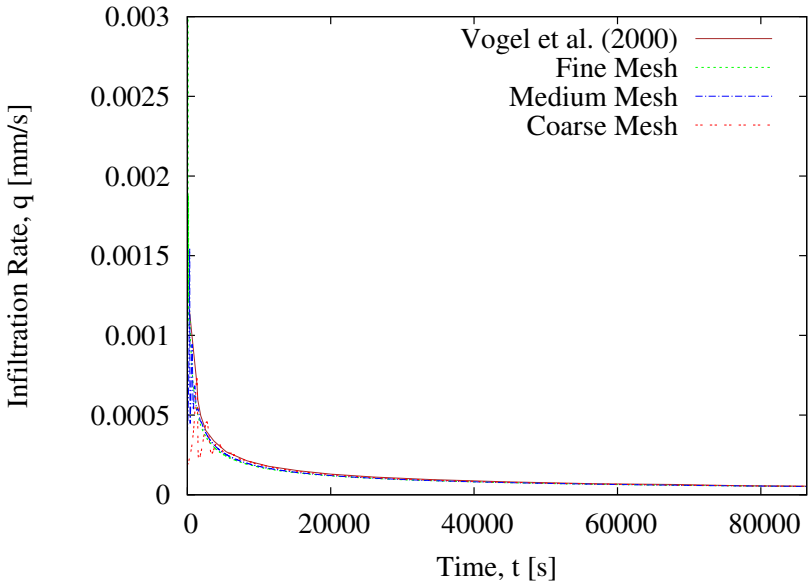

Figure 4.16: Comparison between the infiltration rate for one-dimensional soil column as predicted by the present model and by Vogel et al. (2000) using the original van Genuchten model.

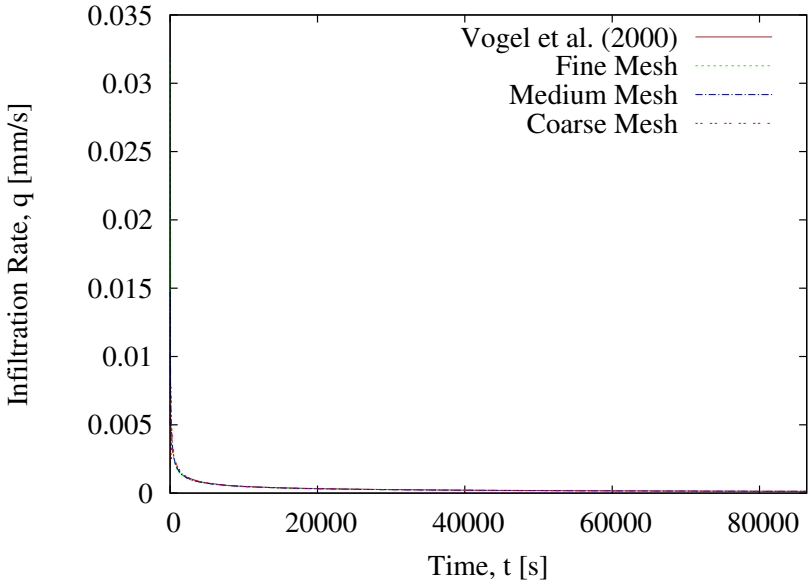

Figure 4.17: Comparison between the infiltration rate for one-dimensional soil column as predicted by the present model and by Vogel et al. (2000) using the modified van Genuchten model.

A closer investigation of the initial infiltration rate (up to a time of 3500 seconds) was carried out using both versions of the van Genuchten model as this is the range in which the oscillations occur during the analyses. Inspection of Figure 4.18 shows large oscillations of the infiltration rate occur at the start of the analysis when the original van Genuchten model is used. In this time range a slight dependence on the level of mesh refinement can be seen. In the case of the coarse mesh, the oscillations continue for longer than for the fine and medium meshes. As time increases, these oscillations smooth out and results no longer depend on mesh size (Figure 4.18).

However, when the modified van Genuchten model is used, oscillations are greatly reduced and only occur for the coarser mesh and then only for a very short initial period (Figure 4.19). Figure 4.19 shows clearly that after about 500 seconds no oscillations occur. The results also become independent of mesh size much sooner than when the original van Genuchten model is used. The oscillations occur due to the shape of the conductivity function which, for the original van Genuchten model, is highly non-linear near saturation. There is less non-linearity in the shape of the conductivity function in the modified van Genuchten model.

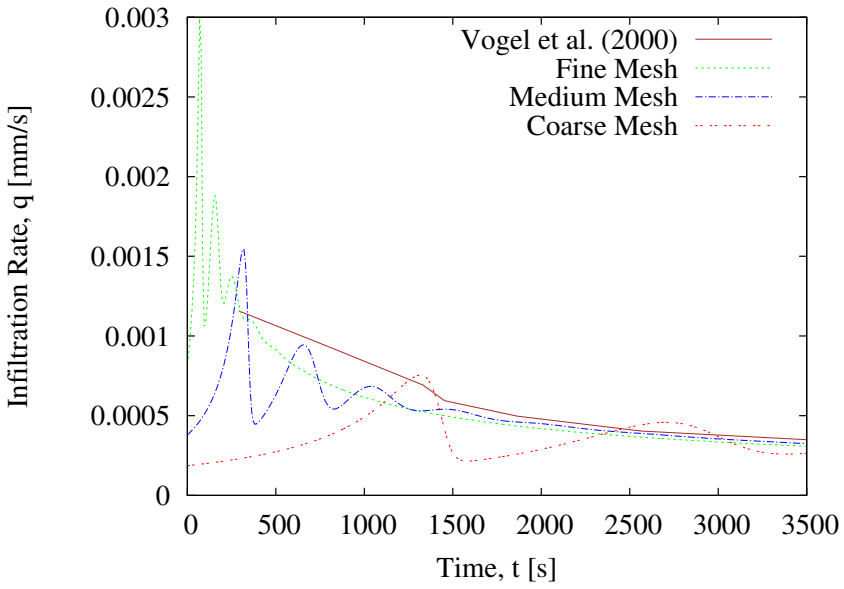

Figure 4.18: Comparison between the initial infiltration rate for one-dimensional soil column as predicted by the present model and by Vogel et al. (2000) using the original van Genuchten model.

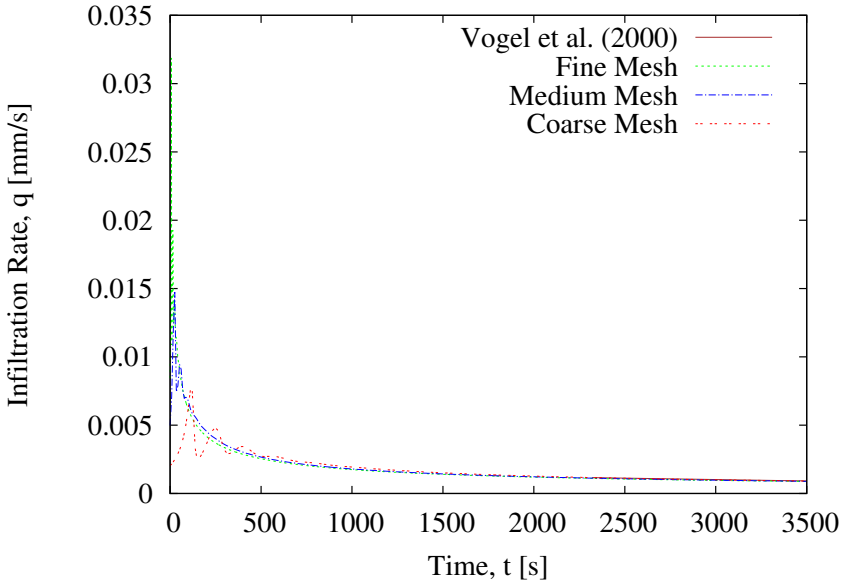

Figure 4.19: Comparison between the initial infiltration rate for one-dimensional soil column as predicted by the present model and by Vogel et al. (2000) using the modified van Genuchten model.

4.2.4 Effect of the time step size on the infiltration rate

An additional study of the influence of different time steps was carried out on the one-dimensional soil column using both the original and modified versions of the van Genuchten model. In this study a constant mesh refinement corresponding to the medium mesh in Section 4.2.3 was used. Three times steps were chosen that correspond to 4.32, 8.64 and 17.28 seconds. The predicted infiltration rates over time for the original and modified version of the van Genuchten model are presented in Figures 4.20 and 4.21 respectively. Inspection of these two figures show that in both cases, the curves are independent of the time step size used for the range shown in these figures.

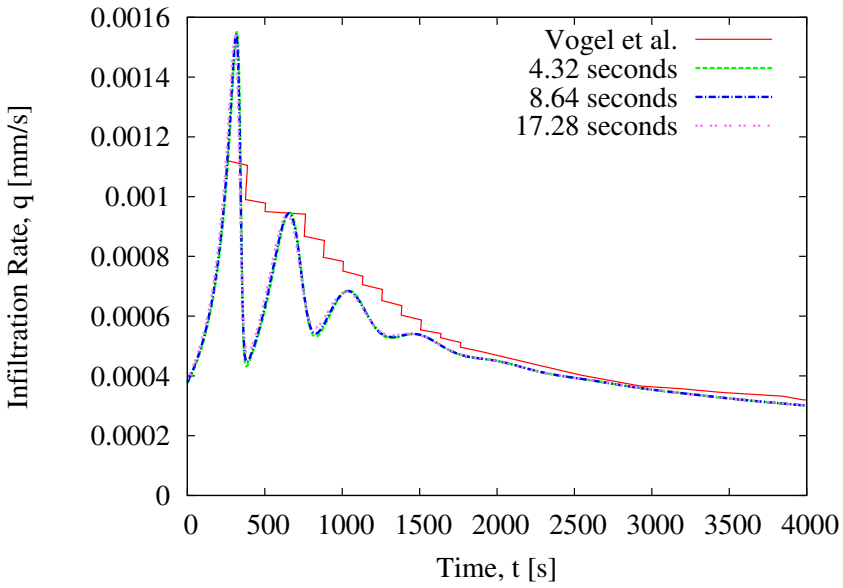

Figure 4.20: Comparison between the infiltration rate versus capillary pressure for different times step lengths using the original van Genuchten model.

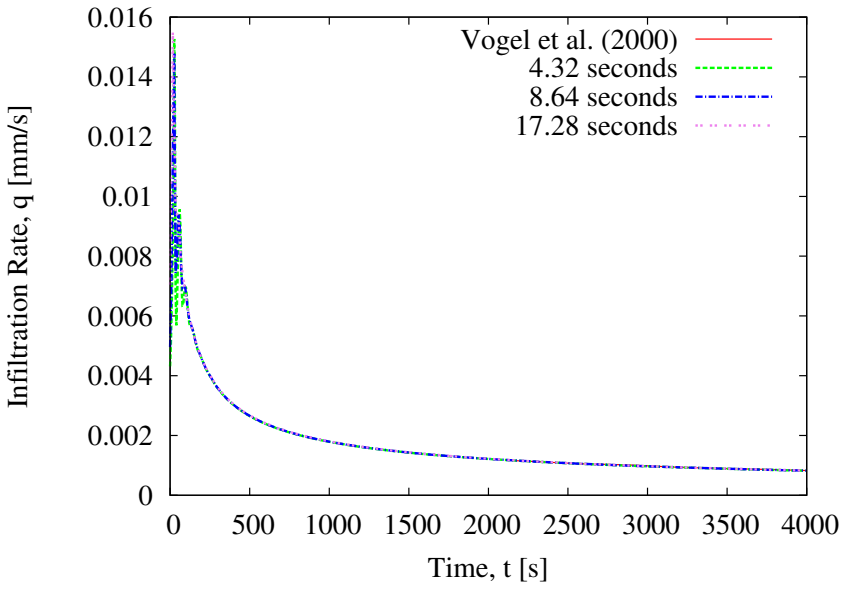

Figure 4.21: Comparison between the infiltration rate versus capillary pressure for different times step lengths using the modified van Genuchten model.

4.3 Discussion

Uncoupled analyses were carried out using the mechanical and transport models presented in Chapter 3 of this thesis. Firstly, mechanical analyses were carried out. For both the

single-edge notched specimen and the double-edge notched specimen, the mechanical model used in the coupled approach proposed in this work captures well the physical phenomena observed during experimental testing. In both cases, reasonably mesh independent load versus CMSD curves and fracture patterns were obtained from the analyses.

Secondly, the implementation of the transport constitutive laws within the OOFEM software was verified and the proposed transport model was investigated using a one-dimensional soil column. Very good agreement was achieved for both the original and modified versions of the van Genuchten model compared to the alternative numerical results presented by Vogel et al. (2000). These analyses also showed the results of the transport model to be independent of both the element length and the time step for the ranges used during analyses.

Chapter 5

2D Analysis of Transport in Uncracked and Cracked Concrete

In order to further verify the capability of the transport model presented in Chapter 3, experiments by Wittmann et al. (2008) were simulated. In this work, two analyses are carried out. Firstly, a transport analysis is carried out on an uncracked concrete specimen and secondly, an analysis of a cracked reinforced concrete specimen is presented. In this two part investigation, an analysis is carried out first on an uncracked concrete specimen. Next, a mechanical three-point bending test is carried out on a similar reinforced concrete specimen to introduce cracking. Then, an analysis of infiltration of water into the cracked specimen is undertaken. For both the uncracked and cracked specimens, the numerical results are compared to experimental results reported in Wittmann et al. (2008). The effect of cracking on the permeability of the transport elements is considered in this analysis. This is the first instance of coupling between the individual mechanical and transport models.

5.1 Moisture Transport Through Unsaturated Concrete

Wittmann et al. (2008) carried out a two-part experimental investigation of moisture transport through uncracked and cracked concrete. In the first part of this work, the measurement of capillary infiltration through an uncracked concrete beam whose bottom surface was put in contact with water was investigated. In this section the specimen geometry and boundary conditions are presented, followed by a comparison between the numerical and experimental results.

5.1.1 Specimen geometry and boundary conditions

The specimen geometry according to Wittmann et al. (2008) is presented in Figure 5.1. The red dashed line in Figure 5.1 indicates the location at which the change in water content is measured during the analysis for comparison with the experimental results (Section 5.1.2).

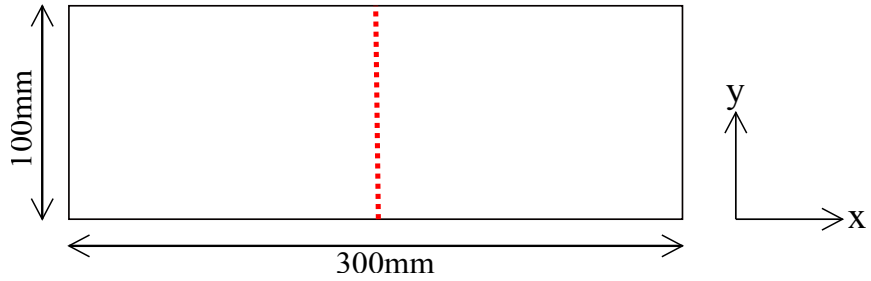

Figure 5.1: Specimen geometry for the concrete beam.

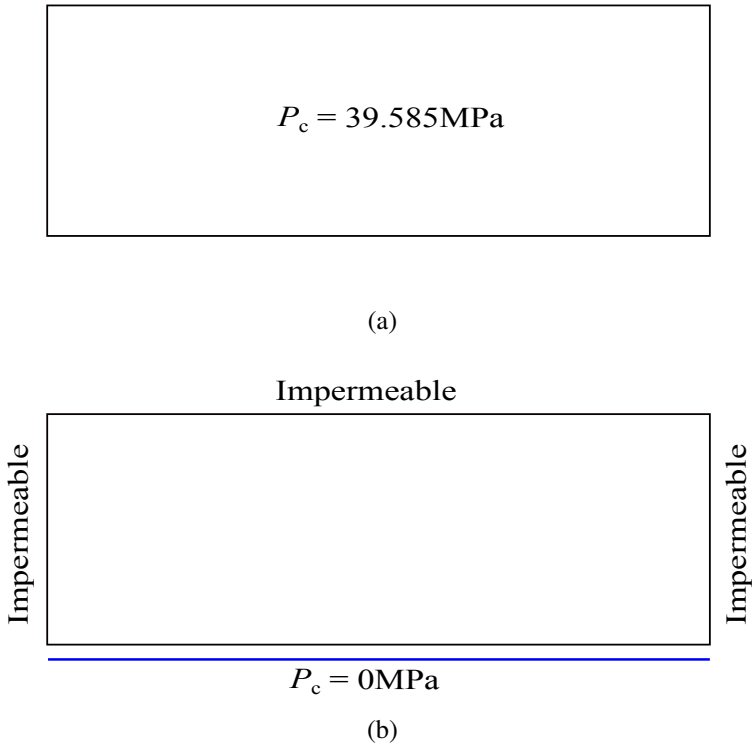

Figure 5.2: (a) Initial boundary conditions for the concrete beam at $t = 0$ and (b) boundary conditions for t ≥ 0.

Table 5.1 presents the parameters used for the analysis. The values of θ_s, θ_r and θ_m were taken from Wittmann et al. (2008), while the values of m and a were determined by Baroghel-Bouny et al. (1999). Cracking is not considered in this test, therefore values for ξ and $\bar{w}_{c,max}$

are not required. Also, the effect of gravity is negligible and therefore is also not considered in this work. The values of the material parameters presented in Table 5.1 vary greatly from those presented in Table 4.3, Section 4.2. The reason for this is that the material composition of the concrete differs from that of the soil.

Table 5.1: Transport material parameters for an unsaturated concrete beam.

θ_s	θ_r	θ_m	μ [MPa s]	κ_i [mm^2]	m	a [MPa]
0.092	0.000	0.0921	1×10^{-9}	1.0×10^{-13}	0.4396	18.6237

The boundary conditions applied are as follows. Prior to the start of the infiltration process, a uniform capillary pressure of 39.585 MPa is assumed throughout the beam (Figure 5.2a). This value corresponded to an assumed effective degree of saturation of 50%. At time zero, the water pressure along the bottom of the beam is changed to zero (i.e. fully saturated condition) while the top and side boundaries are assumed to be impermeable to water (see Figure 5.2b). In a similar manner to the previous case of a 1D soil column, this leads to upward capillary infiltration.

The mesh used is shown in Figure 5.3. As discussed in Section 3.1, the transport elements are placed along the edges of the Voronoi cells.

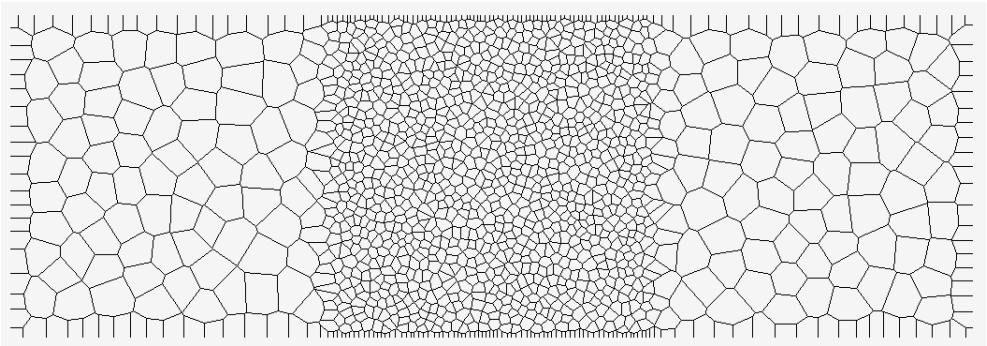

Figure 5.3: Transport mesh for the specimen.

5.1.2 Comparison between numerical and experimental results

A comparison of the changes in water content predicted by the proposed transport model over the depth of the beam (along the centre line of the specimen) at different times against

the experimental results presented by Wittmann et al. (2008) is shown in Figure 5.4. In this work, the term "water content" refers to the mass of water in grams per cm^3 of specimen. Investigation of Figure 5.4 indicates that, at the beginning of the infiltration process, the model agrees reasonably well with the measured increase of water content. This was expected as the value of intrinsic permeability κ was chosen to fit experimental results at an early time.

However, at later stages of the analysis it is observed that the increase of water content is over-predicted. It is still unclear why this over-prediction occurs. There are a number of possible causes of this over-prediction. Firstly, the material is treated as a homogeneous material and therefore the presence of aggregates is ignored. In reality, the presence of aggregates has been shown to slow down the movement of moisture through the specimen (Wang and Ueda, 2011). An alternative explanation for this over-prediction is the possibility that chemical reactions occurred within the experimental specimen due to the presence of the water, which could reduce the permeability of the material. These types of reactions are not taken into account in this study.

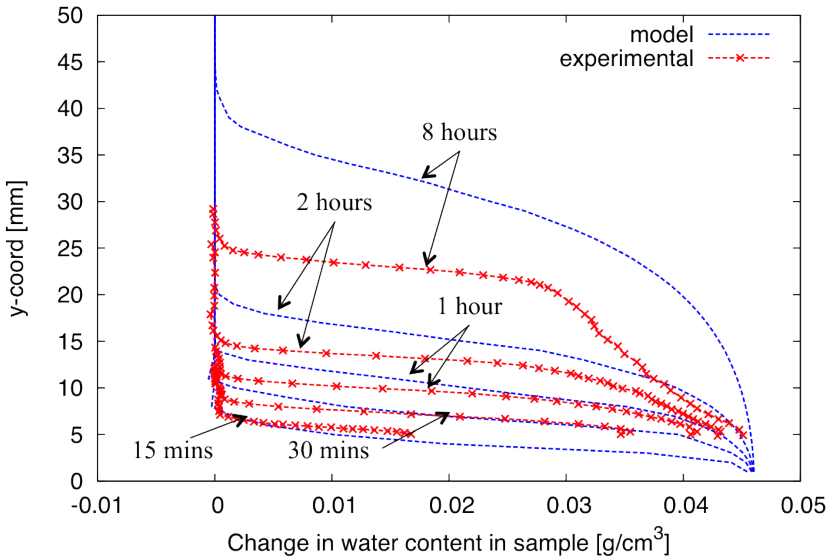

Figure 5.4: Change in water content versus depth of beam.

In Figure 5.5 the contour plots of the capillary pressure obtained for four different time steps during the analysis are presented. In this figure, only the central part of the specimen is shown. At the beginning of the analysis, when the time is zero, the specimen is partially saturated (a degree of saturation of 50% is assumed). Only the very bottom of the specimen

is in contact with the water, corresponding to full saturation. As the analysis progresses the water infiltrates upwards through the specimen.

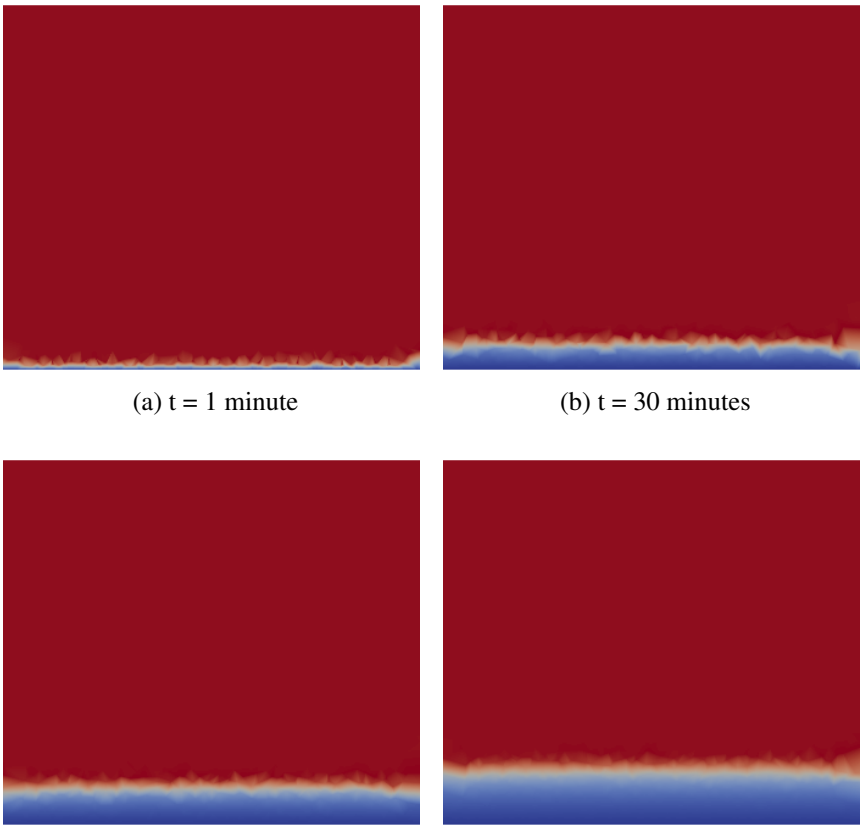

(a) t = 1 minute (b) t = 30 minutes

(c) t = 1 hour (d) t = 2 hours

Figure 5.5: Contour plots of the distribution of capillary pressure for four time steps for an uncracked concrete beam. Red corresponds to $P_c = 39.585\,\text{MPa}$ ($S_e = 0.5$) and blue corresponds to $P_c = 0\,\text{MPa}$ ($S_e = 1$).

Further investigation of the performance of the model is presented in Figure 5.6, in which a comparison between the water penetration depths obtained from the model and the experimental results with respect to the square root of time is shown. In this work, the water penetration depth is defined as the distance from the bottom of the beam to the level at which the water content $\theta = 0.01\,\text{g/cm}^3$. Investigation of Figure 5.6 further confirms the over-prediction of infiltration by the model. A linear relationship between the penetration depth and the square root of time is predicted by the model. This is to be expected as this model is based on the theory of capillary action. Furthermore, Zhang et al. (2011) have investigated this effect also and shown that a linear relationship can be observed for a limited amount of time at least. However, the experimental curve indicates that the measured relationship

between the penetration depth and the square root of time is not linear.

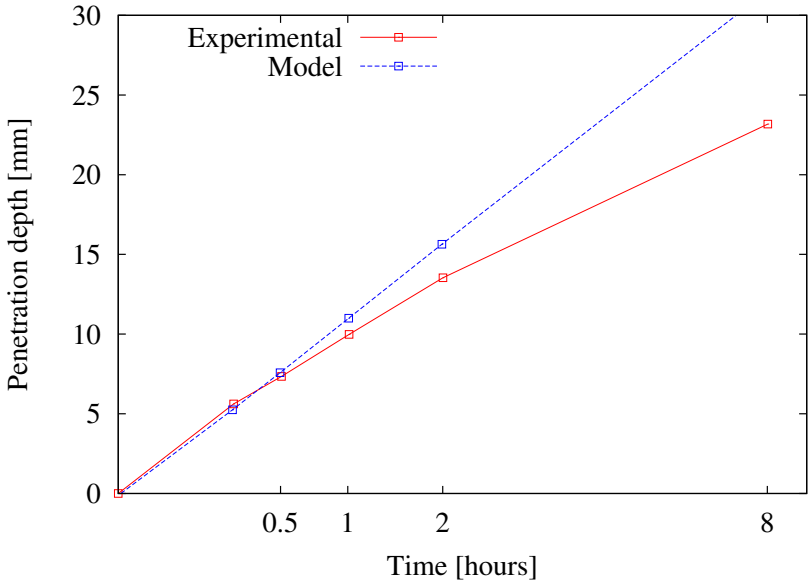

Figure 5.6: Water penetration depth versus the square root of time.

5.1.3 Comparison between 1D and 2D analyses

To further verify the results obtained from the two-dimensional analysis, a simple one-dimensional model of the same problem (i.e. using the same parameter values given in Table 5.1) was analysed. Figure 5.7 shows the change in water content calculated at time 30 minutes by the two-dimensional and one-dimensional models, respectively. Although not identical, Figure 5.7 indicates that the two profiles are very similar which illustrates that the two-dimensional network of pipe elements can correctly reproduce the one-dimensional solution. Figure 5.7 also shows a slight reduction in water content for both the 1D and 2D cases. It is possible that this is caused by a numerical problem in the approach used.

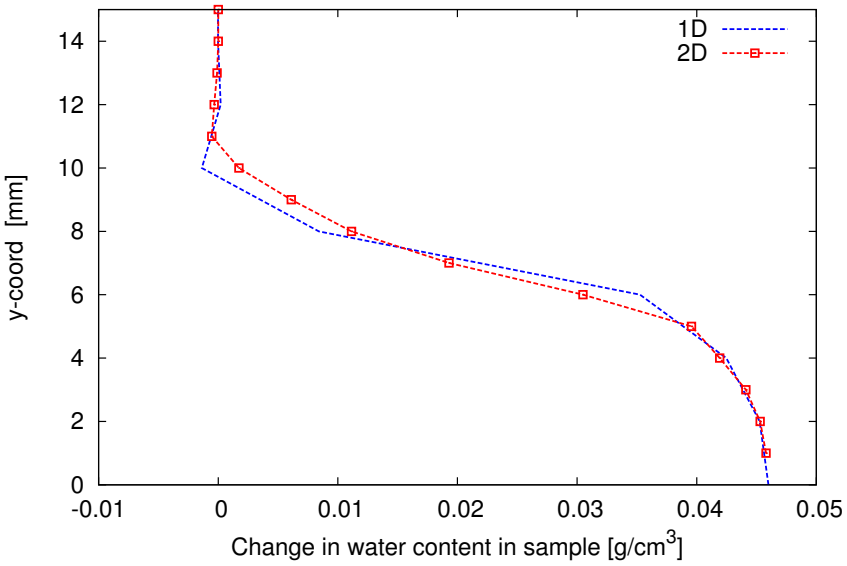

Figure 5.7: Comparison of 1D and 2D results for time equal to 30 minutes.

5.2 Moisture Transport Through Cracked Reinforced Concrete

This section presents the simulations of the second part of the experiments in Wittmann et al. (2008), where moisture transport through cracked reinforced concrete was measured.

5.2.1 Loading set-up and boundary conditions

Firstly, a three point bending test was carried out on a reinforced beam containing two rebars. This created one main crack that propagated centrally from the bottom of the specimen towards the top (Figure 5.8a). Afterwards, the bottom surface of the beam was exposed to water and the change in water content in the beam was recorded at regular intervals of time (Figure 5.8b). The out-of-plane thickness of the specimen is 25 mm and the two rebars (thick red lines in Figure 5.8a) are 8 mm in diameter .

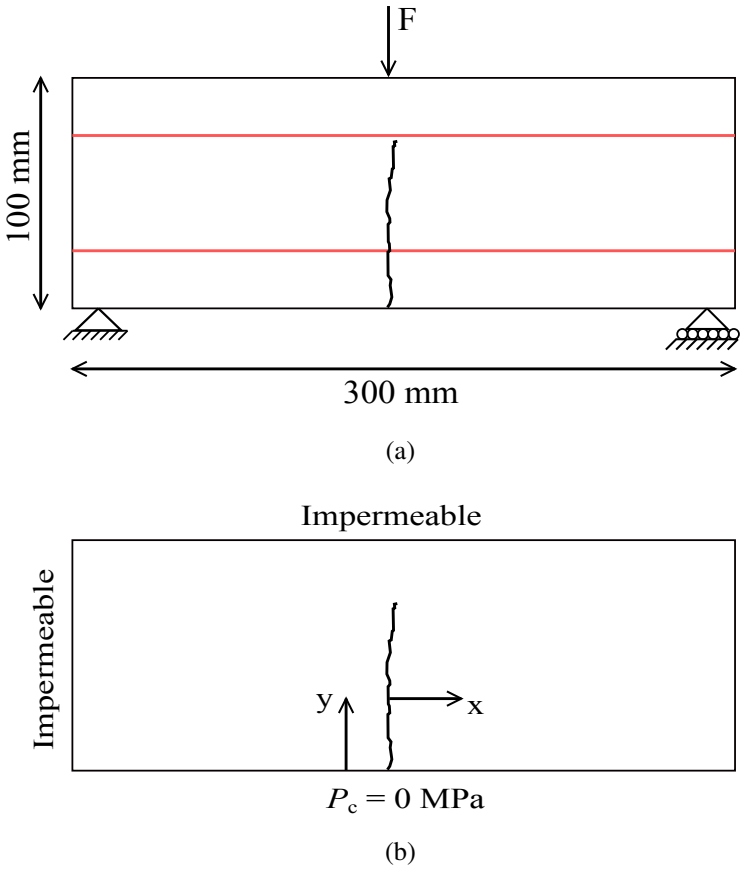

Figure 5.8: Cracked concrete specimen: (a) geometry and loading setup for the three-point bending test beam. The two red lines indicate the rebars. (Wittmann et al. (2008)) and (b) boundary conditions for transport model.

This test was recreated in two stages. Firstly, the mechanical model was used to simulate the three-point bending test until a maximum equivalent crack opening of $\bar{w}_c = 0.35\,\text{mm}$ was achieved. The model parameters used in this analysis are presented in Table 5.2 below and are based on information available in the literature. This analysis does not take into account the influence of fluid pressure, i.e. $b = 0$. The mechanical and transport lattices used during analysis are presented in Figures 5.9a and 5.9b respectively. In both cases, a finer mesh refinement is used in the central third of the specimen.

Table 5.2: Mechanical model parameters for a concrete specimen.

	ε_0	E [GPa]	γ	w_f[mm]	c	q
Concrete	73.437×10^{-6}	48.42	0.3333	1.5202×10^{-2}	20	2
Reinforcement	2.38×10^{-3}	210	0	1.5202×10^{20}	1	1

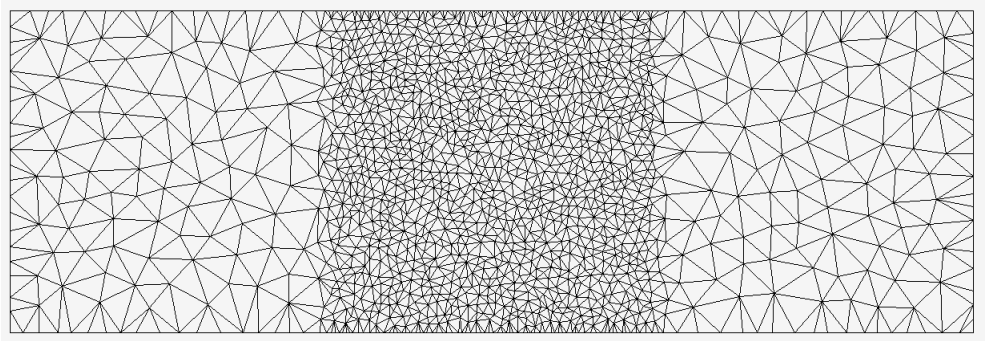

(a)

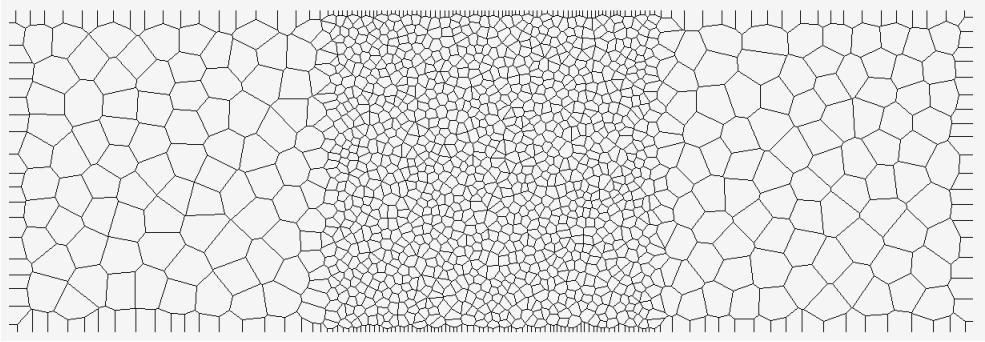

(b)

Figure 5.9: Lattices for the: (a) mechanical and (b) transport analyses.

The fracture pattern obtained from the analysis when a crack width of 0.35 mm is achieved is presented in Figure 5.10. As expected, and in agreement with the experimental results, one single crack propagates upwards along the centre of the beam. Once the required equivalent crack was achieved, the crack widths from all individual elements were determined and recorded.

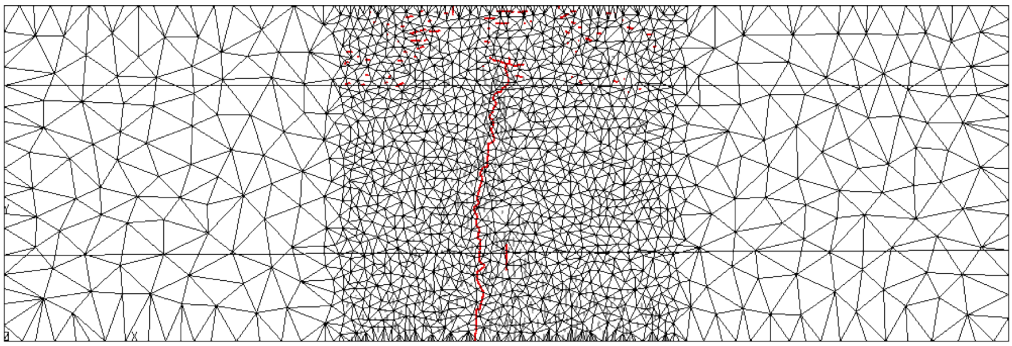

Figure 5.10: Fracture patterns obtained during analysis when a crack width of 0.35 mm is achieved.

The load-crack mouth opening displacement (CMOD) curve obtained from the analysis is presented in Figure 5.11. In the early stages of the analysis, the maximum strength of the concrete is reached and the load decreases slightly. However after this point, the reinforcement allows for additional load to be carried by the beam. A comparison between the maximum load obtained from the load-CMOD curve and the maximum load as calculated using Eurocode was carried out to determine the accuracy of the maximum load predicted. Based of the process outlined in Mosley et al. (2007), the maximum predicted load was 10388 N, which is 13.4% less than the maximum load obtained in the analysis. The process used to determine the maximum predicted load considers partial safety factors. This might explain the difference between the maximum predicted load and the maximum load determined numerically.

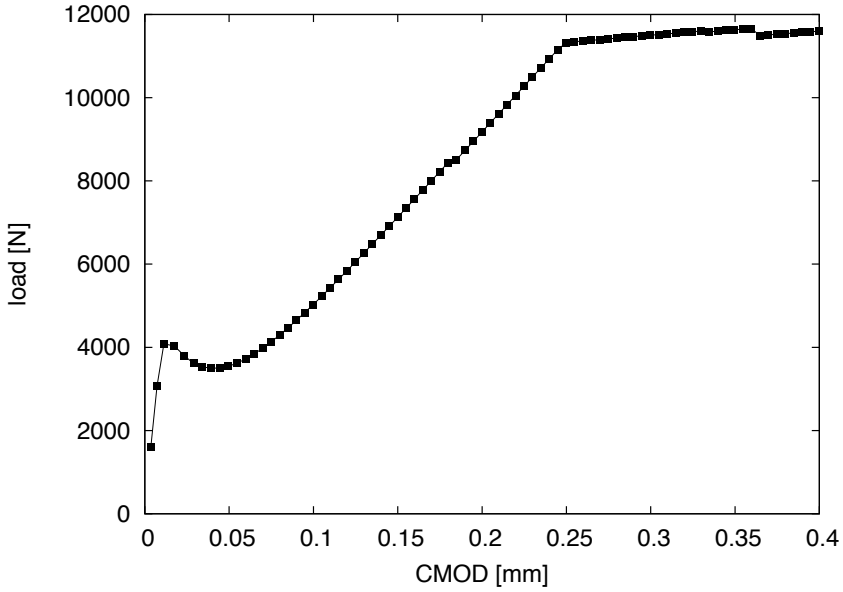

Figure 5.11: Load-CMOD curve obtained from the mechanical analysis.

In the next stage, a transport analysis was carried out on the cracked specimen. The crack widths at a CMOD of 0.35 mm were used to calculate the conductivity from (3.8) in Section 3.2.3. This is the first time in this work that coupling between the mechanical and transport models was considered. The model properties used for the transport analysis are the same as those used in Table 5.1, Section 5.1. In addition to those parameters, the maximum equivalent crack width $\bar{w}_{c,max} = \infty$ was used along with a tortuosity factor $\xi = 0.001$.

5.2.2 Comparison between numerical and experimental results

A comparison between the change in water content predicted by the transport model and the experimental results reported by (Wittmann et al., 2008) over the length of the beam determined at the mid-height are presented in Figure 5.12. In this case, the zero x-coordinate was chosen at the centre of the crack (Figure 5.8b). Inspection of Figure 5.12 shows that the change of water content within and around the crack is over-estimated by the model. However, the numerical model captures well the penetration depth into the surrounding concrete. One possible explanation for the over-prediction of the water content within the crack is that the tortuosity factor is too high and therefore, moisture movement along cracked elements is greater than it should be.

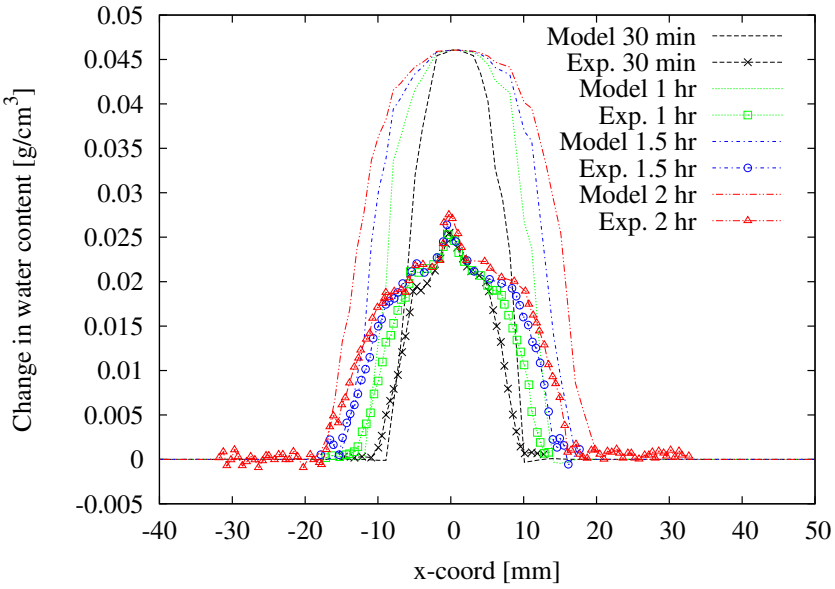

Figure 5.12: Change of water content versus the x-coordinate along the mid-height of the cracked beam.

Figure 5.13, presents contour plots for four different time steps during the analysis. In this figure only the central part of the beam is presented. Inspection of Figure 5.13 shows that the crack acts as a conduit for the additional ingress of moisture into the specimen. There is a visible increase in the moisture content in the area surrounding the crack.

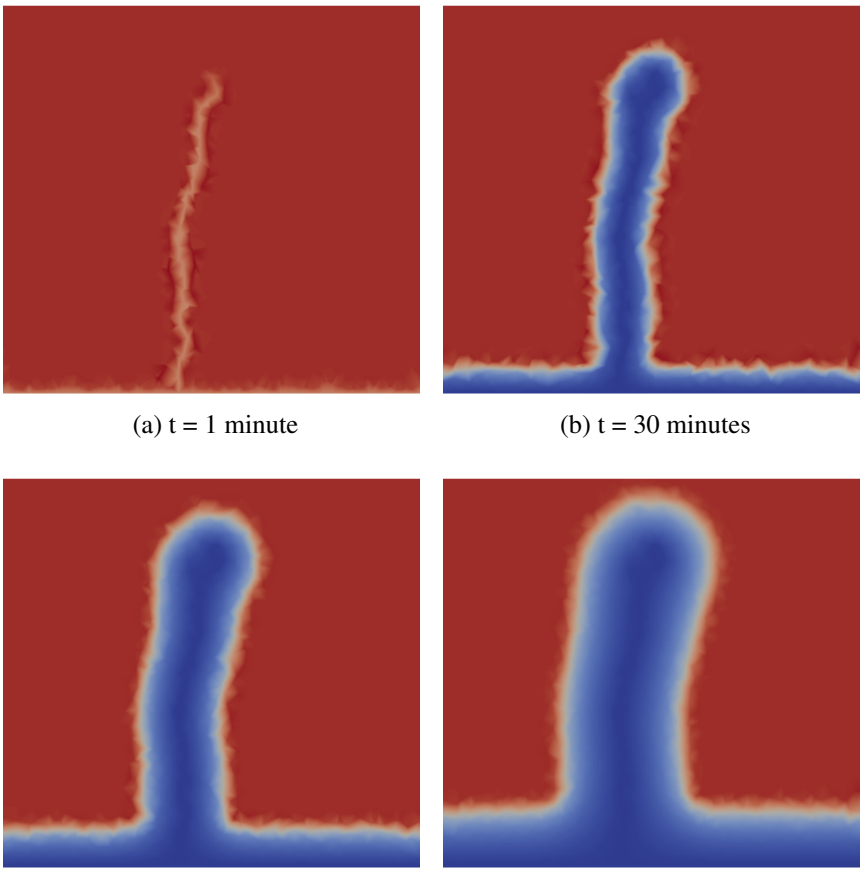

(a) t = 1 minute (b) t = 30 minutes

(c) t = 1 hour (d) t = 2 hours

Figure 5.13: Contour plot of the distribution of capillary pressure for the cracked beam. Red corresponds to $P_c = 39.585\,\text{MPa}$ ($S = 0.5$) and blue corresponds to $P_c = 0\,\text{MPa}$ ($S = 1$).

5.3 Discussion

The rate and extent of water transport in uncracked and cracked concrete due to capillary action was presented in this chapter. It was observed that for the case of uncracked concrete, the proposed transport model captures the water transport for the first few hours very well. This was expected as the value of intrinsic conductivity chosen gave good agreement between the numerical and experimental results during the early stages of the analysis. However, in the later stages of the analysis, the extent of water ingress deviates from the experimental results because the linear relation between water penetration and square root of time predicted by the model deviates from the experimental results for these later stages of the transport processes. Nevertheless, the transport model is capable of simulating water transport both within cracks and from cracks into the surrounding material.

Chapter 6

Analysis of a Thick-Walled Cylinder

In this chapter, the proposed coupled approach is verified by analysing an elastic plane stress thick-walled cylinder subjected to an internal pressure P_{fi} (Figure 6.1) and comparing the numerical results to an analytical solution. The analytical solution was derived as part of this work and the derivation is presented in the first section of this chapter. Previous work has been undertaken by (Shawki and El-Wahil, 1970).

Three different values of Biot's coefficient were considered in this work, corresponding to $b = 0$, 0.5 and 1. In the first instance, a comparison between the numerical results and the analytical solution for the pressure distribution across the cylinder was carried out. Next, an investigation of the effect of varying values of Poisson's ratio on the numerical results in the form of a comparison between the numerically predicted radial displacements and the corresponding analytical solution is presented. Finally, the error that occurs from using a staggered approach for the coupling of the mechanical and transport models is examined.

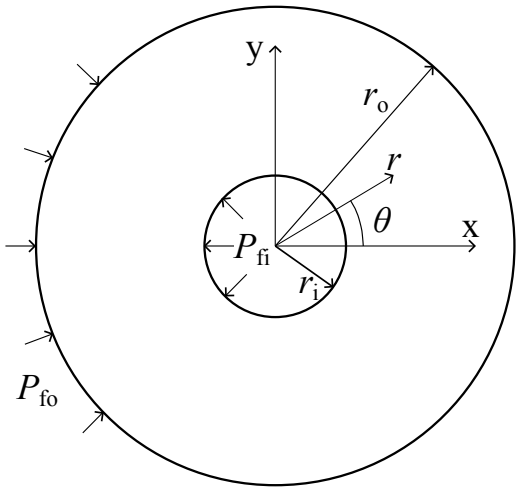

Figure 6.1: Thick-walled cylinder geometry.

6.1 Analytical Solution For the Elastic Response of a Thick-Walled Cylinder

Firstly, the fluid distribution across the cylinder is determined from assuming an internal fluid pressure $P_f(r = r_i) = P_{fi}$ and an external fluid pressure $P_f(r = r_o) = 0$. The radial component of the flux (i.e. the flow rate per unit area) q at a given radial distance r from the centre of the cylinder is

$$q = \frac{Q}{2\pi rt} \tag{6.1}$$

where Q is the total flow rate, r is the radius and t is the out of plane thickness. Alternatively, the radial component of the flux vector can be expressed in terms of conductivity and fluid pressure through Darcy's law as

$$q = \frac{\kappa}{\mu}\frac{dP_f}{dr} \tag{6.2}$$

where κ is the intrinsic hydraulic conductivity, μ is the viscosity and P_f is the fluid pressure (recalling compression negative according to the sign convention of continuum mechanics). Equating (6.1) and (6.2) leads to

$$q = \frac{Q}{2\pi rt} = \frac{\kappa}{\mu}\frac{dP_f}{dr} \tag{6.3}$$

Rearranging (6.3) to give an equation for determining the change in fluid pressure P_f gives

$$\mathrm{d}P_f = \frac{\mu}{\kappa}\frac{Q}{2\pi rt}\mathrm{d}r \tag{6.4}$$

Integrating (6.4) gives

$$P_{\mathrm{f}} = \frac{\mu Q}{2\kappa\pi t}\ln r + C_{\mathrm{i}} \tag{6.5}$$

where C_{i} is a constant of integration and is determined by imposing the boundary condition of fluid pressure at the outer boundary $P_{\mathrm{f}}(r = r_{\mathrm{o}}) = 0$ as

$$C_{\mathrm{i}} = -\frac{\mu Q}{2\kappa\pi t}\ln r_{\mathrm{o}} \tag{6.6}$$

Substituting (6.6) into (6.5) gives

$$P_{\mathrm{f}} = \frac{\mu Q}{2\kappa\pi t}\ln r - \frac{\mu Q}{2\kappa\pi t}\ln r_{\mathrm{o}} \tag{6.7}$$

which can be also be expressed as

$$P_{\mathrm{f}} = -\frac{\mu Q}{2\kappa\pi t}\ln\frac{r_{\mathrm{o}}}{r} \tag{6.8}$$

Next, an expression for the flow rate is determined. By imposing the boundary condition of fluid pressure at the inner boundary, $P_{\mathrm{f}}(r = r_{\mathrm{i}}) = P_{\mathrm{fi}}$ in (6.8), the total flow rate Q is

$$Q = -\frac{2\kappa\pi t}{\mu\ln\dfrac{r_{\mathrm{o}}}{r_{\mathrm{i}}}}P_{\mathrm{fi}} \tag{6.9}$$

Substituting (6.9) into (6.8), an expression for the fluid pressure is obtained as

$$P_{\mathrm{f}} = \frac{\ln\dfrac{r_{\mathrm{o}}}{r}}{\ln\dfrac{r_{\mathrm{o}}}{r_{\mathrm{i}}}}P_{\mathrm{fi}} \tag{6.10}$$

which is a function of the radius r, inner radius r_{i}, outer radius r_{o} and the internal fluid pressure P_{fi}. Equation (6.10) can be expressed in a dimensionless form by introducing the following dimensionless variables; $\bar{r} = r/r_{\mathrm{i}}$, $\bar{r}_{\mathrm{o}} = r_{\mathrm{o}}/r_{\mathrm{i}}$, $\bar{P}_{\mathrm{f}} = P_{\mathrm{f}}/E_{\mathrm{c}}$ and $\bar{P}_{\mathrm{fi}} = P_{\mathrm{fi}}/E_{\mathrm{c}}$. Thus, (6.10) becomes

$$\bar{P}_{\mathrm{f}} = \bar{P}_{\mathrm{fi}}\frac{\ln\dfrac{\bar{r}_{\mathrm{o}}}{\bar{r}}}{\ln\bar{r}_{\mathrm{o}}} \tag{6.11}$$

Next, an expression for the radial displacement caused by the seepage force due to fluid flow is derived. The equilibrium equation for axisymmetric conditions, is given as

$$\frac{\mathrm{d}\sigma_{\mathrm{r}}}{\mathrm{d}r} + \frac{\sigma_{\mathrm{r}} - \sigma_{\theta}}{r} = 0 \tag{6.12}$$

where σ_r and σ_θ are the total radial and tangential stress respectively and are defined as

$$\sigma_\mathrm{r} = \sigma_\mathrm{r}^\mathrm{m} + bP_\mathrm{f} \tag{6.13}$$

and

$$\sigma_\theta = \sigma_\theta^\mathrm{m} + bP_\mathrm{f} \tag{6.14}$$

in which b is the Biot's coefficient. Substituting (6.13) and (6.14) into (6.12), the equilibrium equation can be expressed in terms of effective stresses as

$$\frac{\mathrm{d}\sigma_\mathrm{r}^\mathrm{m}}{\mathrm{d}r} + \frac{\sigma_\mathrm{r}^\mathrm{m} - \sigma_\theta^\mathrm{m}}{r} + b\frac{\mathrm{d}P_\mathrm{f}}{\mathrm{d}r} = 0 \tag{6.15}$$

Substituting the expression for P_f from (6.10) into (6.15) gives

$$\frac{\mathrm{d}\sigma_\mathrm{r}^\mathrm{m}}{\mathrm{d}r} + \frac{\sigma_\mathrm{r}^\mathrm{m} - \sigma_\theta^\mathrm{m}}{r} + b\frac{\mathrm{d}}{\mathrm{d}r}\left(\frac{\ln\dfrac{r_\mathrm{o}}{r}}{\ln\dfrac{r_\mathrm{o}}{r_\mathrm{i}}}P_\mathrm{fi}\right) = 0 \tag{6.16}$$

Next, Hooke's law for plane stress conditions is used to relate the effective radial and tangential stresses to the corresponding strains as

$$\sigma_\mathrm{r}^\mathrm{m} = \frac{E_\mathrm{c}}{1-\nu^2}\left(\varepsilon_\mathrm{r} + \nu\varepsilon_\theta\right) \tag{6.17}$$

$$\sigma_\theta^\mathrm{m} = \frac{E_\mathrm{c}}{1-\nu^2}\left(\varepsilon_\theta + \nu\varepsilon_\mathrm{r}\right) \tag{6.18}$$

Using the definition of radial and tangential strain in terms of radial displacement u gives

$$\varepsilon_\mathrm{r} = \frac{\mathrm{d}u}{\mathrm{d}r} \tag{6.19}$$

$$\varepsilon_\theta = \frac{u}{r} \tag{6.20}$$

Using (6.17) to (6.20) in (6.16) gives the following differential equation for the radial displacement u

$$\frac{d^2u}{dr^2} + \frac{du}{dr}\frac{1}{r} - \frac{u}{r^2} - b\frac{P_\mathrm{fi}}{E_\mathrm{c}}\frac{1-\nu^2}{\ln\dfrac{r_\mathrm{o}}{r_\mathrm{i}}}\frac{1}{r} = 0 \tag{6.21}$$

The above differential equation can now be written using dimensionless variables. The dimensionless variables are chosen as $\bar{u} = u/r_\mathrm{i}$, $\bar{r}_\mathrm{o} = r_\mathrm{o}/r_\mathrm{i}$, $\bar{r} = r/r_\mathrm{i}$, $\bar{P}_\mathrm{fi} = P_\mathrm{fi}/E_\mathrm{c}$ and ν. Setting these expressions into the differential equation, a dimensionless differential equation is ob-

tained as

$$\frac{d^2\bar{u}}{d\bar{r}^2}+\frac{d\bar{u}}{d\bar{r}}\frac{1}{\bar{r}}-\frac{\bar{u}}{\bar{r}^2}-b\bar{P}_{\mathrm{fi}}\frac{1-\nu^2}{\ln\bar{r}_{\mathrm{o}}}\frac{1}{\bar{r}}=0 \tag{6.22}$$

The normalised radial displacement $\bar{u}$ can be expressed as a function of the normalised radial coordinate $\bar{r}$ from the solution of (6.22) as

$$\bar{u}=\frac{1}{2}b\bar{P}_{\mathrm{fi}}\frac{1-\nu^2}{\ln\bar{r}_{\mathrm{o}}}\bar{r}\ln\bar{r}+\frac{C_1}{\bar{r}}+C_2\bar{r} \tag{6.23}$$

where C_1 and C_2 are the constants of integration, determined by imposing two boundary conditions in terms of stresses, strains or displacements. The tangential and radial strains are calculated from (6.23) as

$$\varepsilon_{\mathrm{r}}=\frac{\mathrm{d}\bar{u}}{\mathrm{d}\bar{r}}=\frac{1}{2}b\bar{P}_{\mathrm{fi}}\frac{1-\nu^2}{\ln\bar{r}_{\mathrm{o}}}(\ln\bar{r}+1)+\frac{C_1}{\bar{r}^2}+C_2 \tag{6.24}$$

and

$$\varepsilon_{\theta}=\frac{u}{r}=\frac{1}{2}b\bar{P}_{\mathrm{fi}}\frac{1-\nu^2}{\ln\bar{r}_{\mathrm{o}}}\ln\bar{r}+\frac{C_1}{\bar{r}^2}+C_2 \tag{6.25}$$

Similarly, the tangential and radial dimensionless stresses $\bar{\sigma}_{\mathrm{r}}^{\mathrm{m}}=\sigma_{\mathrm{r}}^{\mathrm{m}}/E_{\mathrm{c}}$ and $\bar{\sigma}_{\theta}^{\mathrm{m}}=\sigma_{\theta}^{\mathrm{m}}/E_{\mathrm{c}}$, are calculated using Hooke's law in (6.17) and (6.18) and the strain definitions in (6.24) and (6.25), giving

$$\bar{\sigma}_{\mathrm{r}}^{\mathrm{m}}=\frac{\varepsilon_{\mathrm{r}}+\nu\varepsilon_{\theta}}{1-\nu^2}=\frac{1}{2}b\bar{P}_{\mathrm{fi}}\frac{1}{\ln\bar{r}_{\mathrm{o}}}[(1+\nu)\ln\bar{r}+1]-\frac{1}{1+\nu}\frac{C_1}{\bar{r}^2}+\frac{1}{1+\nu}C_2 \tag{6.26}$$

and

$$\bar{\sigma}_{\theta}^{\mathrm{m}}=\frac{\varepsilon_{\theta}+\nu\varepsilon_{\mathrm{r}}}{1-\nu^2}=\frac{1}{2}b\bar{P}_{\mathrm{fi}}\frac{1}{\ln\bar{r}_{\mathrm{o}}}[(1+\nu)\ln\bar{r}+\nu]+\frac{1}{1+\nu}\frac{C_1}{\bar{r}^2}+\frac{1}{1+\nu}C_2 \tag{6.27}$$

Now, the two constants of integration are determined by imposing a constraint where the effective radial stress in (6.26) is equal to $(1-b)\,\bar{P}_{\mathrm{fi}}$ at the inner boundary ($\bar{\sigma}_{\mathrm{r}}^{\mathrm{m}}(\bar{r}=1)=(1-b)\,\bar{P}_{\mathrm{fi}}$) and zero at the outer boundary ($\bar{\sigma}_{\mathrm{r}}^{\mathrm{m}}(\bar{r}=\bar{r}_{\mathrm{o}})=0$). Thus

$$C_1=\frac{1}{2}b\bar{P}_{\mathrm{fi}}\frac{\bar{r}_{\mathrm{o}}^2}{1-\bar{r}_{\mathrm{o}}^2}(1+\nu)^2+(1-b)\,\bar{P}_{\mathrm{fi}}\frac{\bar{r}_{\mathrm{o}}^2}{1-\bar{r}_{\mathrm{o}}^2}(1+\nu) \tag{6.28}$$

and

$$C_2=\frac{1}{2}b\bar{P}_{\mathrm{fi}}\left[\frac{\bar{r}_{\mathrm{o}}^2}{1-\bar{r}_{\mathrm{o}}^2}\left(1-\nu^2\right)-\frac{1-\nu}{\ln\bar{r}_{\mathrm{o}}}\right]+(1-b)\,\bar{P}_{\mathrm{fi}}\frac{1-\nu}{1-\bar{r}_{\mathrm{o}}^2} \tag{6.29}$$

Substituting (6.28) and (6.29) into (6.23), and rearranging, the following expression for the dimensionless displacement $\bar{u}$ is obtained

$$\bar{u} = b\bar{P}_{\mathrm{fi}}\frac{1-\nu^2}{2}\left[\frac{\bar{r}_{\mathrm{o}}^2}{1-\bar{r}_{\mathrm{o}}^2}\left(\frac{1+\nu}{1-\nu}\frac{1}{\bar{r}}+\bar{r}\right)-\bar{r}\frac{\dfrac{1}{1+\nu}-\ln\bar{r}}{\ln\bar{r}_{\mathrm{o}}}\right] + (1-b)\,\bar{P}_{\mathrm{fi}}\frac{\bar{r}_{\mathrm{o}}^2}{1-\bar{r}_{\mathrm{o}}^2}\left(\frac{1+\nu}{\bar{r}}+\frac{\bar{r}(1-\nu)}{\bar{r}_{\mathrm{o}}^2}\right) \tag{6.30}$$

Furthermore, substituting (6.28) and (6.29) into (6.26) and (6.27) results in expressions for the dimensionless radial and tangential stresses (equations (6.31) and (6.32) respectively).

$$\bar{\sigma}_{\mathrm{r}}^{\mathrm{m}} = \frac{1}{2}b\bar{P}_{\mathrm{fi}}(1+\nu)\left[\frac{\bar{r}_{\mathrm{o}}^2}{1-\bar{r}_{\mathrm{o}}^2}\left(1-\frac{1}{\bar{r}^2}\right)+\bar{r}\frac{\ln\bar{r}}{\ln\bar{r}_{\mathrm{o}}}\right]+(1-b)\,\bar{P}_{\mathrm{fi}}\frac{1}{1-\bar{r}_{\mathrm{o}}^2}\left(1-\frac{\bar{r}_{\mathrm{o}}^2}{\bar{r}^2}\right) \tag{6.31}$$

$$\bar{\sigma}_{\theta}^{\mathrm{m}} = \frac{1}{2}\bar{P}_{\mathrm{fi}}(1+\nu)\left[\frac{\bar{r}_{\mathrm{o}}^2}{1-\bar{r}_{\mathrm{o}}^2}\left(1+\frac{1}{\bar{r}^2}\right)+\frac{\ln\bar{r}}{\ln\bar{r}_{\mathrm{o}}}-\frac{1}{\ln\bar{r}_{\mathrm{o}}}\frac{1-\nu}{1+\nu}\right] + (1-b)\,\bar{P}_{\mathrm{fi}}\frac{1}{1-\bar{r}_{\mathrm{o}}^2}\left(1-\frac{\bar{r}_{\mathrm{o}}^2}{\bar{r}^2}\right) \tag{6.32}$$

Inspection of (6.30) indicates that Biot's coefficient strongly influences the displacement field. For example, in the limit situation of a cylinder with an infinitely large outer radius ($\bar{r}_{\mathrm{o}} \to \infty$), (6.30) gives for Terzaghi's effective stress theory (Terzaghi, 1925) ($b = 1$)

$$\bar{u} = -\bar{P}_{\mathrm{fi}}\frac{1+\nu^2}{2}\left(\frac{1+\nu}{1-\nu}\frac{1}{\bar{r}}+\bar{r}\right) \tag{6.33}$$

whereas, for $b = 0$, or an impermeable inner boundary which would give $P_{\mathrm{f}} = 0$ throughout the cylinder and hence the same result

$$\bar{u} = -\bar{P}_{\mathrm{fi}}\frac{1+\nu}{\bar{r}} \tag{6.34}$$

6.2 Comparison Between Analytical and Numerical Solutions

An elastic thick-walled cylinder subjected to an internal fluid pressure under plane stress conditions is analysed in this section (Figure 6.1). The boundary conditions assumed during the analysis are as follows: a fluid pressure P_{fi} (and equal total stress) is applied along the

inner radius of the cylinder r_i and at the outer radius r_o the fluid pressure is zero (and the total stress). In the case of this example, $r_i/r_o = 1/7$. A quarter of the mechanical and transport lattices are shown in Figures 6.2a and 6.2b, respectively. A minimum distance of $0.017r_o$ was used to generate the mesh.

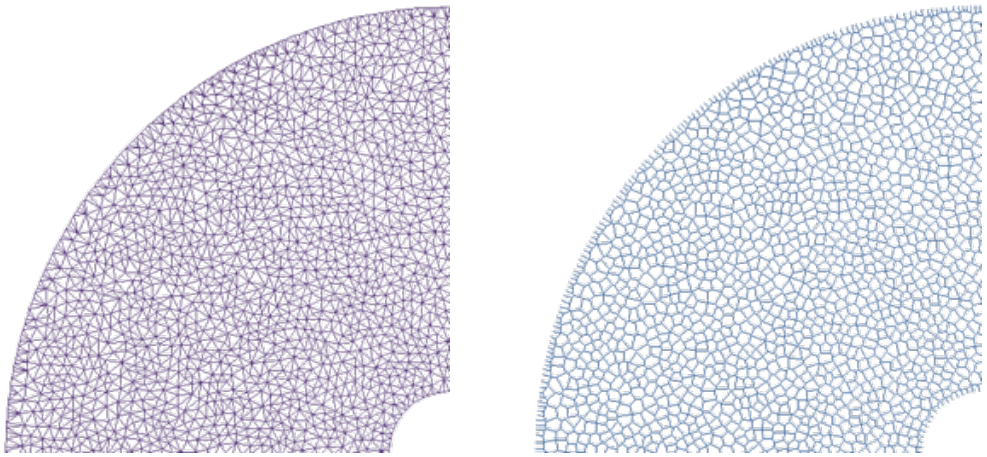

(a) (b)

Figure 6.2: Quarter of the lattice mesh used in analyses: (a) mechanical lattice and (b) transport lattice for a cylinder containing a hole in the centre.

6.2.1 Fluid pressure distribution

In the first instance, the fluid pressure distribution predicted by the proposed coupled approach is compared to the analytical solution presented in (6.11). In Figure 6.3, the numerical results are presented as average values determined over small intervals of radial coordinates of the cylinder. An investigation of Figure 6.3 shows excellent agreement between the numerical and analytical solutions for the fluid pressure distribution.

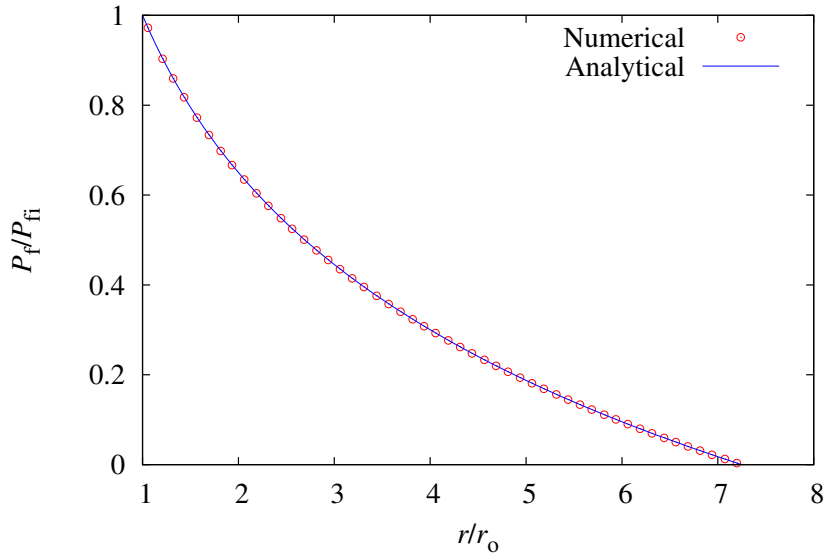

Figure 6.3: Comparison of numerical and analytical results for the normalised fluid pressure distribution.

6.2.2 Effect of Poisson's ratio on numerical results

The numerical results for the radial displacement were compared to the analytical solutions for three different values of Poisson's ratio: $\nu = 0$, 0.1 and 0.2 and Biot's coefficient of $b = 0$, 0.5 and 1 in Figures 6.4 to 6.6. In each of these figures, the numerical results are presented in the form of average values determined over small intervals of radial coordinates of the cylinder. Note that values of $\bar{u}/\bar{P}_{fi}$ are negative, so that positive (tensile) values of the inner fluid pressure P_{fi} lead to negative (inward) values of radial displacement u, whereas negative (compressive) values of P_{fi} lead to positive (outward) values of u.

Investigation of Figures 6.4 to 6.6 shows that the lattice model reproduces well the analytical solutions for the radial displacements of the thick-walled cylinder. This agreement is particularly good for $\nu = 0$ and $\nu = 0.1$ (Figures 6.4 and 6.5). As the value of Poisson's ratio is increased, the level of accuracy of the numerical results reduces. Perhaps, this results from the equations for the model parameters E and γ that are used to relate the continuum properties of the specimen to the local properties of the lattice element (Section 3.3.3, Equations (3.27) and (3.28)). As stated earlier in this report, an irregular mesh is used and therefore (3.27) and (3.28) are used only as an approximation.

The response of the cylinder is strongly influenced by the Biot's coefficient value. For a negative (compressive) value of P_{fi}, when a value of $b = 1$ is assumed for the Biot coefficient, the cylinder stretches in the radial direction. However, for the same situation and $b = 0$, a compression of the cylinder occurs in the radial direction. This is the case regardless of the value of Poisson's ratio used in the analysis.

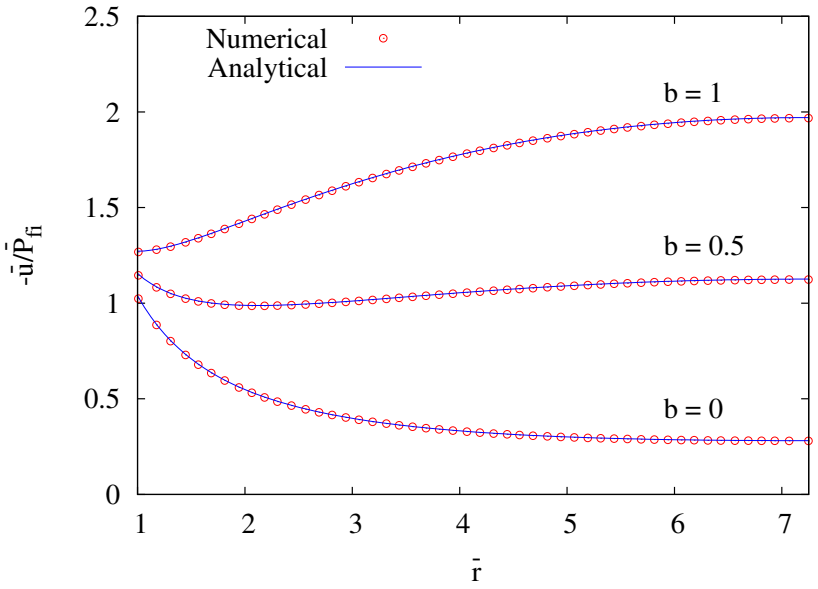

Figure 6.4: Comparison of numerical and analytical normalised radial displacements for a Poisson's ratio $\nu = 0$ and Biot's coefficient $b = 0$, 0.5 and 1.

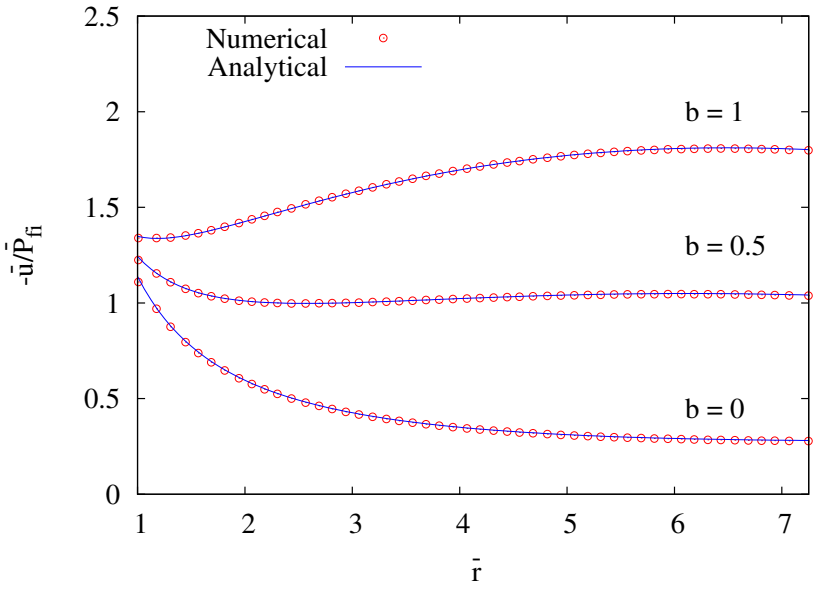

Figure 6.5: Comparison of numerical and analytical normalised radial displacements for a Poisson's ratio $\nu = 0.1$ and Biot's coefficient $b = 0$, 0.5 and 1.

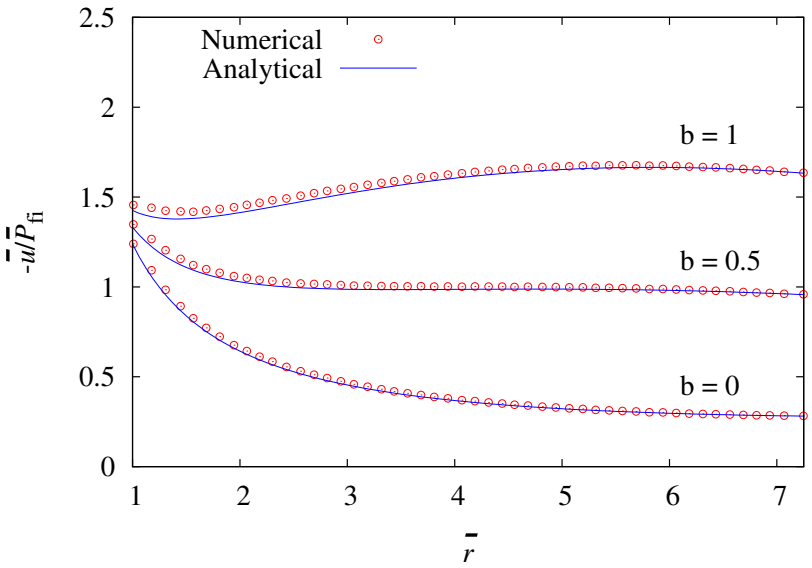

Figure 6.6: Comparison of numerical and analytical normalised radial displacements for a Poisson's ratio $\nu = 0.2$ and Biot's coefficient $b = 0$, 0.5 and 1.

The numerical results without averaging are presented in Figures 6.7 to 6.9. In these figures, the red symbols represent the numerical value determined at each node within the specimen. Investigation of Figures 6.7 and 6.8 indicates that at every node the agreement between the numerically predicted radial displacement and the analytical solution is excellent. However, inspection of Figure 6.9 shows that when $\nu = 0.2$ the radial displacements recorded at each node are slightly more varied than when a Poisson's ratio of either $\nu = 0$ or $\nu = 0.1$ is used.

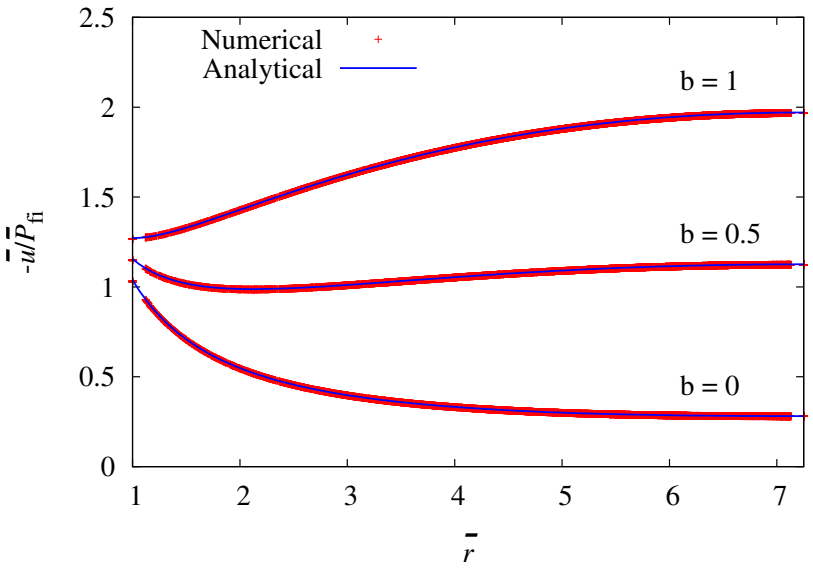

Figure 6.7: Comparison of numerical and analytical normalised radial displacements for a Poisson's ratio $\nu = 0$ and Biot's coefficient $b = 0$, 0.5 and 1.

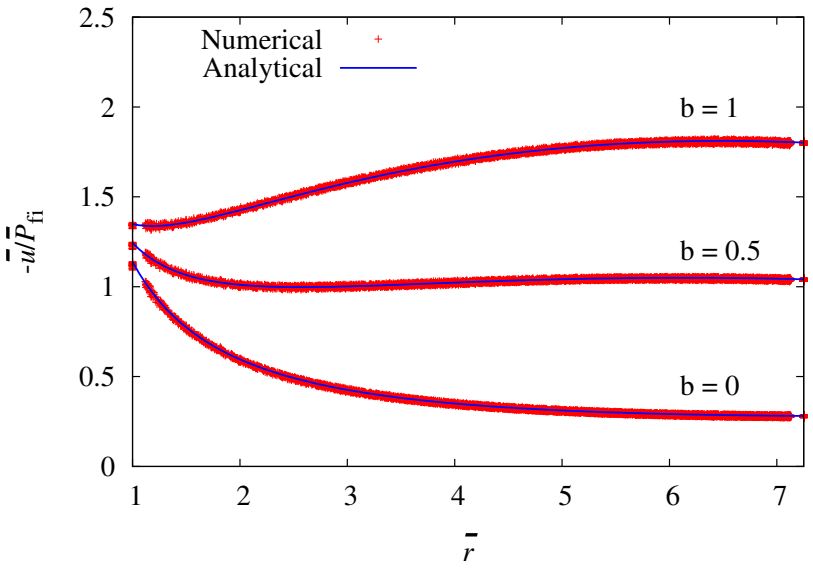

Figure 6.8: Comparison of numerical and analytical normalised radial displacements for a Poisson's ratio $\nu = 0.1$ and Biot's coefficient $b = 0$, 0.5 and 1.

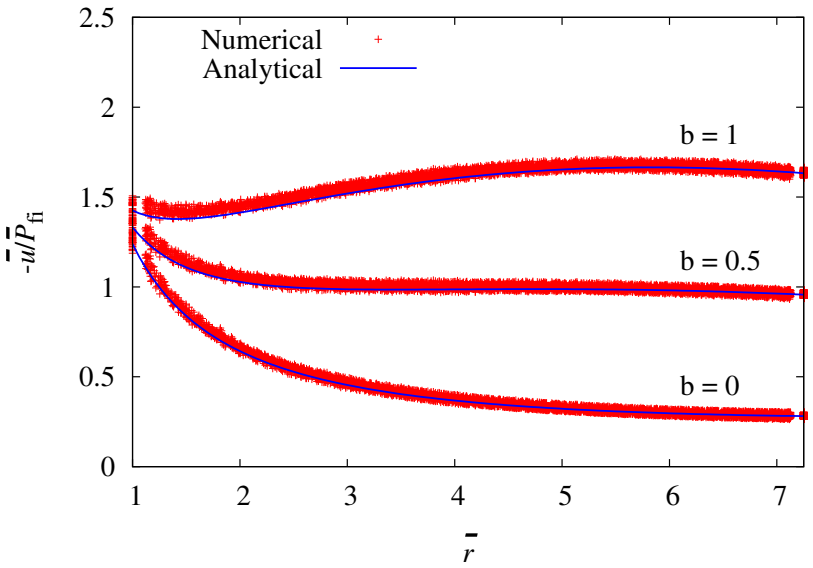

Figure 6.9: Comparison of numerical and analytical normalised radial displacements for a Poisson's ratio $\nu = 0.2$ and Biot's coefficient $b = 0$, 0.5 and 1.

6.3 Assessment of Errors in the Applied Staggered Approach

In the staggered approach used in this work, each model is solved individually and information is only exchanged at the beginning of each time step, resulting in an error. The effect of this staggered approach on the resulting fluid pressure is investigated in this work.

In Section 6.2, a fluid pressure was applied as a boundary condition resulting in deformation of the mechanical mesh. Now an alternative approach is considered in which an Eigen-strain is applied to the interface elements crossing the boundary between the inclusion and the matrix, resulting in a fluid pressure in the transport model (Section 3.4). In this case, an Eigen-displacement corresponding to the radial displacement determined at the inner boundary of the cylinder in Section 6.2, is applied as a boundary condition in the mechanical model. A quarter of the mechanical and transport meshes are shown in Figures 6.10a and 6.10b, respectively. Unlike the previous cylinder case in Section 6.2, this cylinder contains an inclusion in the centre. The inclusion is considered for the mechanical mesh but it is not included as part of the transport mesh (Figure 6.10). As with the previous case in Section 6.2, a minimum distance of $0.017r_o$ was used to generate the mesh. The Biot coefficient was chosen as $b = 1.0$ and a Poisson's ratio of $\nu = 0$ was used. In this case, the Eigen-displacement

is applied over one time step only and held constant for the rest of the analysis.

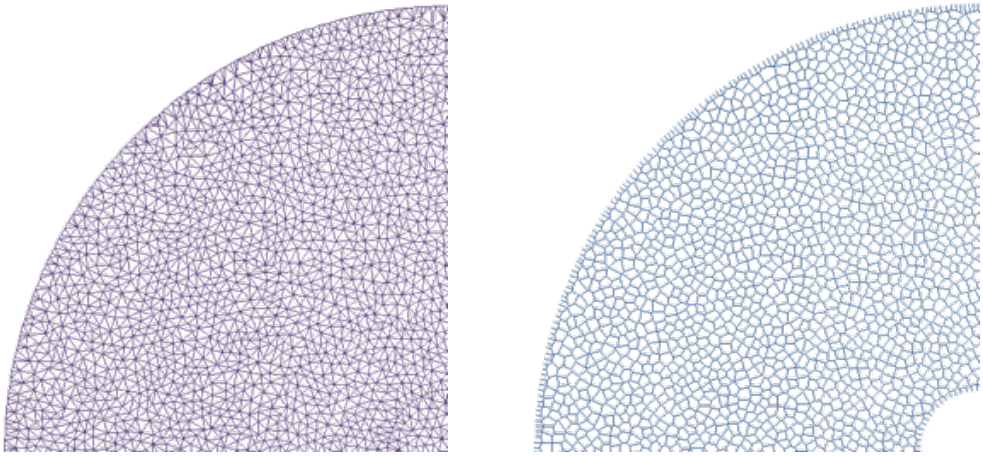

(a) (b)

Figure 6.10: Quarter of the lattice mesh used in analyses: (a) mechanical lattice and (b) transport lattice for a thick-walled cylinder containing an impermeable inclusion.

Figure 6.11 highlights the error encountered when an Eigen-displacement is applied as a boundary condition. Investigation of Figure 6.11 indicates that initially the error is very large. However as the analysis continues, the error reduces and converges to the correct solution. In this case, the term convergence relates to the results of iterations during which the boundary conditions are unchanged. The error can be reduced greatly by applying the Eigen-displacement in much smaller increments.

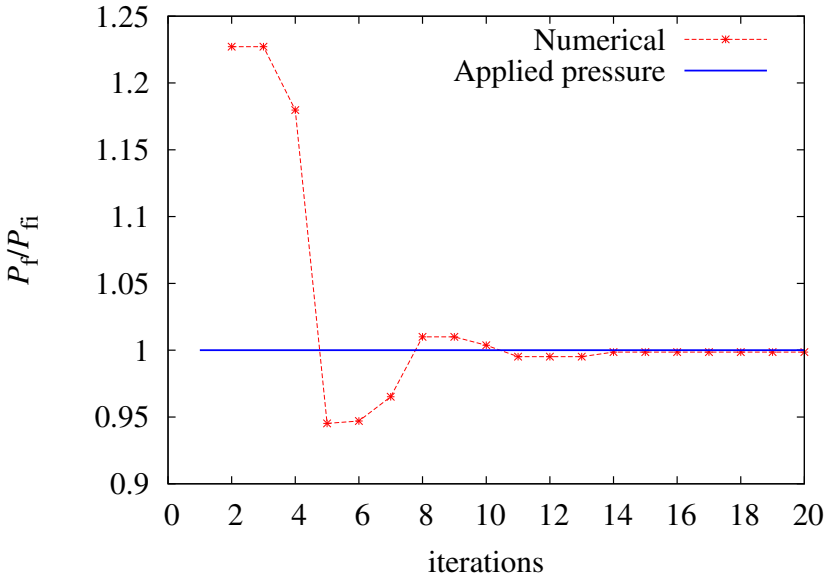

Figure 6.11: Error obtained using staggered approach.

6.4 Discussion

The coupled approach proposed in this work was verified by comparing the numerical results with analytical solutions derived in Section 6.1 of this chapter. Three different values of Biot's coefficient were considered corresponding to $b = 0$, 0.5 and 1.

In the first instance, a comparison between the numerical results and the analytical solution for the pressure distribution across the cylinder was carried out. In this case, excellent agreement between the numerical results and the analytical solution was obtained.

A comparison between the numerically predicted radial displacements and the corresponding analytical solution was presented for varying values of Poisson's ratio. Excellent agreement was achieved between the numerical results and the analytical solutions when the value of Poisson's ratio was taken either as 0 or 0.1. As the value of Poisson's ratio was increased to 0.2, the level of agreement reduces slightly. This is expected as it is one of the limitations of the lattice approach.

Finally, the error encountered from using the staggered approach was investigated. When

a large Eigen-displacement is applied, the error obtained is initially large. However, as the error reduces as the analysis continues and the correct solution is achieved.

Chapter 7

Corrosion-Induced Cracking of Reinforced Concrete

In this section, the proposed coupled lattice approach is applied to the plane stress analysis of corrosion-induced cracking of reinforced concrete specimens with both single and multiple reinforcement bars. In the proposed approach, the cracking of the concrete is captured by the mechanical model and the transport model describes the flow of the corrosion products into the pores and cracks.

The corrosion products are assumed to behave as a fluid and therefore require properties such as viscosity. A value of viscosity is determined for a specimen containing a single reinforcement bar based on experiments reported by Andrade et al. (1993). The value of viscosity determined during the study is applied to an additional analysis to assess the ability of the proposed model for predicting corrosion-induced cracking in a specimen containing multiple rebars. A comparison between numerical and experimental results is presented. Finally a sensitivity study is presented. An investigation of the effect of parameters such as the viscosity of the corrosion products and the tortuosity of the cracks on the time to cracking is presented.

7.1 Assumptions and Limitations of Proposed Approach

A number of assumptions and simplifications are made as part of this approach and are as

follows:

- Firstly, compression of the corrosion products is not considered in this work. It is assumed that the stiffness of the corrosion products is not dependent on time or the amount of corrosion formed.
- The material is assumed to be fully saturated.
- The Biot coefficient is set to zero.
- The viscosity of the corrosion products is time-independent.
- At the rebar/concrete boundary, the mechanical stresses are equal to the fluid pressure. This assumes that the rebar and concrete are separated by a layer of corrosion products.

7.2 Application of Corrosion Products

In this approach, an eigen-displacement u_{cor} is applied to the mechanical elements that cross the rebar-concrete interface to initiate the corrosion process (Figure 7.1). This eigen-displacement is applied using the method discussed in Section 3.4. The inclusion (steel rebar) and the interface elements are both given high stiffnesses relative to the stiffness of the surrounding concrete. Therefore, the resulting radial displacement in these elements is equal to the applied eigen-displacement. The applied eigen-displacement results in a mechanical normal stress $\sigma_{\text{n}}^{\text{m}}$ in the concrete surrounding the rebar.

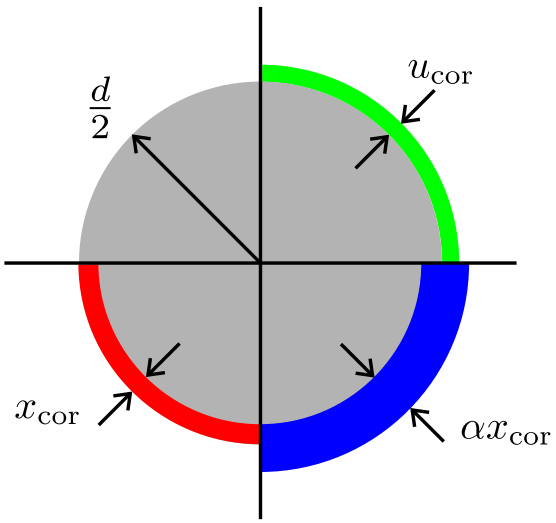

Figure 7.1: Geometry of a reinforcement bar with corrosion layers.

The resulting mechanical stress σ_n^m is then used as a boundary condition for the transport model assuming that a layer of corrosion products separates the rebar and the concrete. By using (3.36) in Section 3.4, the mechanical stress is transformed to a fluid pressure and it is this fluid pressure that drives the transport model and thus results in the penetration of corrosion products into the concrete.

In Figure 7.1, the total radial thickness of corrosion products generated during the analysis is shown as αx_{cor} and comprises three parts; the applied eigen-displacement u_{cor}, the attack penetration depth x_{cor} and the equivalent thickness of corrosion products penetrating the pores f, which gives in incremental form

$$\alpha \Delta x_{cor} = \Delta x_{cor} + \Delta u_{cor} + \Delta f \tag{7.1}$$

In (7.1), the parameter α is the corrosion expansion coefficient, i.e. the ratio of the volume of corrosion products to the volume of reinforcement steel consumed in producing these corrosion products.

7.3 Calculation of Attack Penetration Depth

During the process of corrosion of the reinforcing steel, part of the steel is consumed and transformed into corrosion products. This reduction in steel radius is referred to as the attack penetration depth x_{cor} (Figure 7.1). The numerical analyses presented in this chapter are compared to experimental accelerated corrosion tests in which a current is applied to initiate the corrosion process. Assuming that the entire applied current density i_{cor} is consumed in the corrosion process, the amount of corrosion products generated can be related to the attack penetration depth x_{cor} through Faraday's law where

$$\Delta x_{cor} = 0.0315 i_{cor} \Delta t \tag{7.2}$$

in which 0.0315 is a conversion factor for converting the applied current density $\mu A/\text{cm}^2$ to a length in mm as used by Molina et al. (1993), i_{cor} is the corrosion current density and Δt is the increment of time in seconds. The conversion factor 0.0315 is determined from parameters such as the molar mass of steel, the anodic reaction valence, Faraday's constant and the density of steel. The value of 0.0315 as presented by Molina et al. (1993) is valid for specific values of the parameters outlined previously. With (7.2), the applied current

density reported in experimental work can be used to calculate the attack penetration depth for comparison with numerical results.

In (7.1), both Δx_{cor} and Δf are dependent on the time increment Δt. The change in the amount of corrosion products flowing into the pores surrounding the rebar is defined as

$$\Delta f = Q\Delta t \tag{7.3}$$

where Q is the rate of corrosion products penetrating the pores. Substituting (7.2) and (7.3) into (7.1) leads to

$$0.0315 i_{\text{cor}} \Delta t \alpha = 0.0315 i_{\text{cor}} \Delta t + \Delta u_{\text{cor}} + Q\Delta t \tag{7.4}$$

Rearranging (7.4), for the time increment Δt gives

$$\Delta t = \frac{\Delta u_{\text{cor}}}{0.0315 i_{\text{cor}} (\alpha - 1) - Q} \tag{7.5}$$

At each step in the analysis, the time increment Δt corresponding to the current eigen-displacement Δu_{cor} is determined based on the rate of corrosion products penetrating the pores Q.

7.4 Determination of Viscosity of Corrosion Products

The proposed model assumes that the corrosion products behave as a fluid. Based on this assumption an appropriate value of viscosity for the corrosion products needs to be determined. This section discusses the approach for determining the value of viscosity.

7.4.1 Specimen geometry and boundary conditions

A reinforced concrete specimen with a single reinforcement bar was analysed based on experiments reported in Andrade et al. (1993). The geometry and loading setup are shown in Figure 7.2a. The out-of-plane thickness of the specimen is 380 mm. In the analyses, the crack opening was defined as the relative displacement between two nodes placed along the top of the specimen indicated by two circular dots in Figure 7.2a. In the mechanical model, the base of the specimen has a pinned support in the left hand corner and all other nodes along the base have roller supports (Figure 7.2a). For the transport model, the specimen is assumed to be fully saturated and along the external boundaries the pressure is assumed to be zero (Figure 7.2b). Along the boundary between the rebar and the concrete, an eigen-displacement is

applied which then results in a fluid pressure.

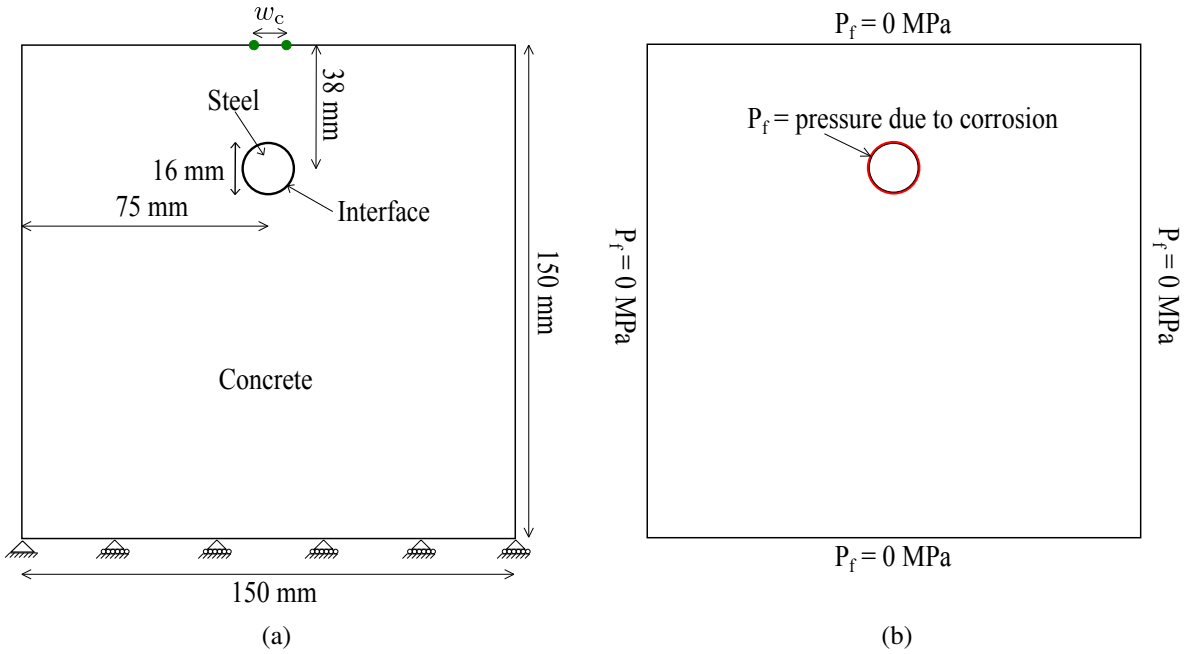

Figure 7.2: Concrete specimen containing a single reinforcing bar: (a) geometry (Andrade et al., 1993) and (b) boundary conditions.

The model input parameters for the concrete and rebar are shown in Table 7.1. The interface was given the same model parameters as the concrete, except for the parameter γ which controls the shear stiffness (Table 7.1). This parameter was chosen to be considerably smaller for the interface to allow cracks in the vicinity of the interface to open. The transport properties used during analyses are given in Table 7.2. In this work, as the height of the specimen is so small, the effect of gravity is negligible and therefore is not considered. Is is noted that the material parameters presented in Table 7.1 differ to those presented earlier in Table 4.1, Section 4.1.1 for example. These values are specific to each type of concrete and can also differ due to the availability of the values in the literature. In some cases, not all of the material parameters are available and may need to be calculated or assumed.

Table 7.1: Mechanical model parameters for a single reinforcement test.

	ε_0	E [GPa]	γ	w_f [mm]	c	q	b
Concrete	8.636×10^{-5}	36.995	1	5.6566×10^{-2}	20	2	0
Steel	8.636×10^{5}	262.5	1	-	-	-	0
Interface	8.636×10^{-5}	36.995	1.0×10^{-6}	5.6566×10^{-2}	50	2	0

Table 7.2: Transport model parameters for a single reinforcement test.

	κ_i $[\text{mm}^2]$	ξ	$\bar{w}_{c,max}$ [mm]
Concrete	1.0×10^{-10}	0.001	0.05
Interface	1.0×10^{-10}	0.001	0.05

Based on the procedure discussed in Section 7.4, the value of the viscosity of the corrosion products that lead to the x_{cor} achieving reasonable agreement with the results reported in the experimental works by Andrade et al. (1993) was determined as 2.0×10^{-2} MPa s. A value of the tortuosity factor ξ was chosen as 0.001 for use in future analyses based on previous work carried out by Grassl et al. (2013). Molina et al. (1993) assumed a rust expansion coefficient of $\alpha = 2$ for this test. Therefore, this value was also assumed in this work.

The lattices used for the mechanical and transport analyses are shown in Figure 7.3a and 7.3b respectively. A finer mesh refinement with $d_{min} = 2$ mm was used in the vicinity of the rebar where the majority of damage occurs. For the mechanical model, the complete specimen was meshed including the rebar (Figure 7.3a). The rebar was assumed to be impermeable to the fluid. Therefore, it was not meshed for the transport model (Figure 7.3b).

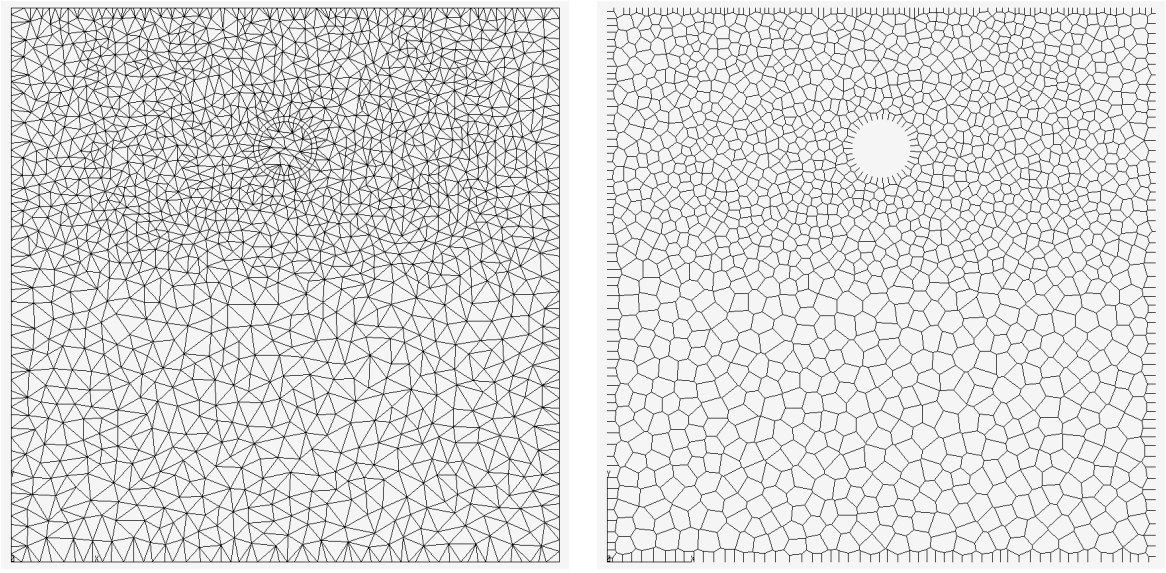

(a) (b)

Figure 7.3: Lattices for the: (a) mechanical and (b) transport analyses.

7.4.2 Comparison between numerical and experimental results

According to experiments reported by Andrade et al. (1993), the final attack penetration depth x_{cor} varies between approximately 68.0 μm and 72.0 μm. Andrade et al. (1993) also reported that a small layer of the rebar (14.9 μm) had been attacked before the test started. In order to conduct a fair comparison between the numerical results obtained from the proposed coupled approach and the experimental results, the initial experimental results were aligned with the predicted numerical results at an attack penetration depth x_{cor} of 14.9 μm.

Figure 7.4 shows a comparison of a purely mechanical model, the coupled approach and the experimental results reported by Andrade et al. (1993). When a purely mechanical model is applied, the crack widths obtained in the experiments are over-estimated.

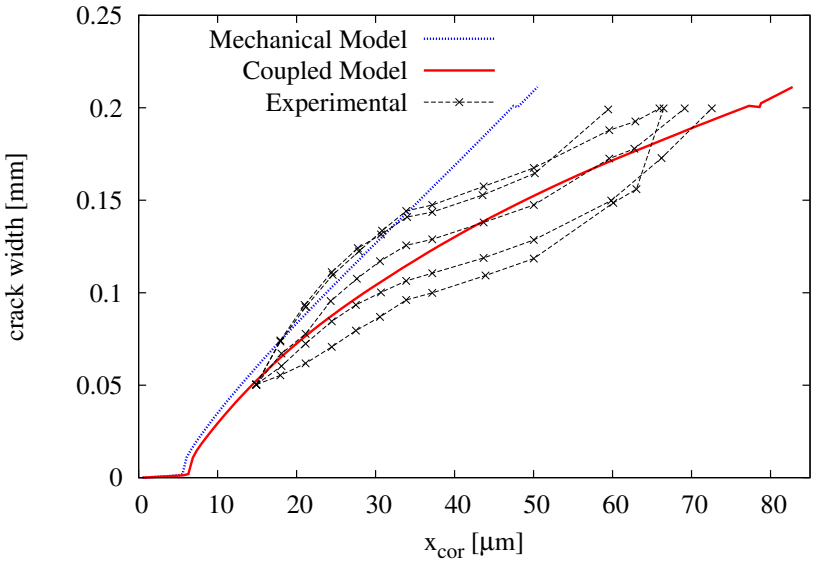

Figure 7.4: Comparison between numerical and experimental results presented by Andrade et al. (1993).

The amount of corrosion products that penetrate the concrete surrounding the rebar was also investigated. The ratio between the volume of corrosion products penetrating the pores and the total volume of corrosion products is presented in Figure 7.5 and is determined as

$$\frac{V_c^t}{V_c^{total}} = \frac{f}{\alpha x_{cor}} \tag{7.6}$$

where V_c^t is the volume of corrosion products that have penetrated the pores at a particular

time, V_c^{total} is the total volume of corrosion products that have been generated at this time, f is the total length of corrosion products penetrating the pores. In Figure 7.5, it can be seen that the percentage of the volume of corrosion products that has penetrated the pores varies greatly during the analysis. Initially the proportion of corrosion products that has penetrated the pores increases rapidly. As the analysis continues, there is a period (as x_{cor} ranges from 6.87 μm to 13.44 μm) when the rate at which the volume of corrosion products travel into the concrete reduces. When investigating the range of x_{cor} in which the percentage of corrosion products penetrating the pores reduces, it is important to note that this is a pressure driven problem. As the Eigen-displacement is applied, it generates stresses within the interface elements that cross the boundary between the rebar and the inclusion. These stresses drive the transport problem and thus cause the corrosion products to penetrate the pores surrounding the rebar (Section 3.4). As these stresses increase, they lead to cracking of the concrete specimen which in turn reduces the stresses acting on the interface elements. This reduction corresponds to the stage in the analysis when the specimen starts to crack and the stresses driving the transport problem reduce.

Finally, in the last part of the analysis, the volume of corrosion products penetrating micro-cracks increases dramatically. As the cracks are increasing in size, the resulting increase in permeability now allows for more corrosion products to penetrate into the pores and micro-cracks surrounding the rebar despite the reduction in pressure.

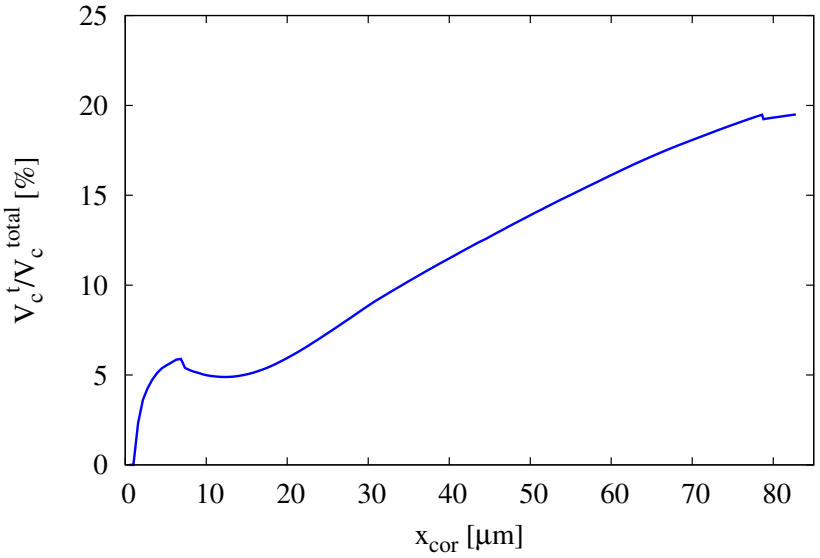

Figure 7.5: Percentage of corrosion products penetrating pores and micro-cracks for a reinforced specimen with a single rebar.

An investigation of the average fluid pressure in the transport elements along the rebar/concrete boundary was undertaken. The main reason for this was to verify the assumption that initially the mechanical stresses are the dominant force causing the corrosion products to penetrate the pores until cracking increases and the effect of cracks on the conductivity now dominates the flow problem, as presented in the previous paragraph. Figure 7.6 presents the average stresses and their corresponding attack penetration depths for the duration of the analysis. The average fluid pressure increases until the peak stress is reached at an attack penetration depth of approximately $6.29\,\mu$m. After this point the fluid pressure initially decreases rapidly before starting to decrease more gradually. This peak in pressure corresponds to the first peak in Figure 7.5.

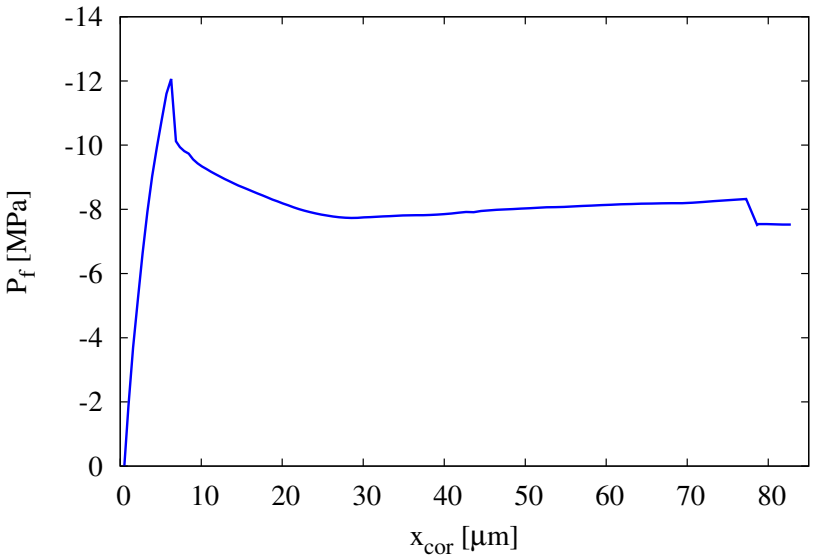

Figure 7.6: Average fluid pressure along the steel/concrete boundary for a singularly reinforced specimen.

The fracture patterns obtained for different values of x_{cor} during the analysis are shown in Figure 7.7. In the proposed approach, fracture is represented as solid red lines. The red lines indicate the cross-section of an element in which damage occurs in the current time step, grey lines show that damage has occurred in these elements but that the level of damage in the element is not increasing in the current time step. For $x_{\text{cor}} = 6.87\,\mu$m, there is already a single dominant crack that has reached the surface of the specimen. However, there are still a lot of smaller micro-cracks occurring around the rebar at this stage. By the end of the analysis at $x_{\text{cor}} = 82.79\,\mu$m, the crack propagating from the rebar to the surface of the concrete remains, but the micro-cracks present earlier have now been replaced by larger

cracks.

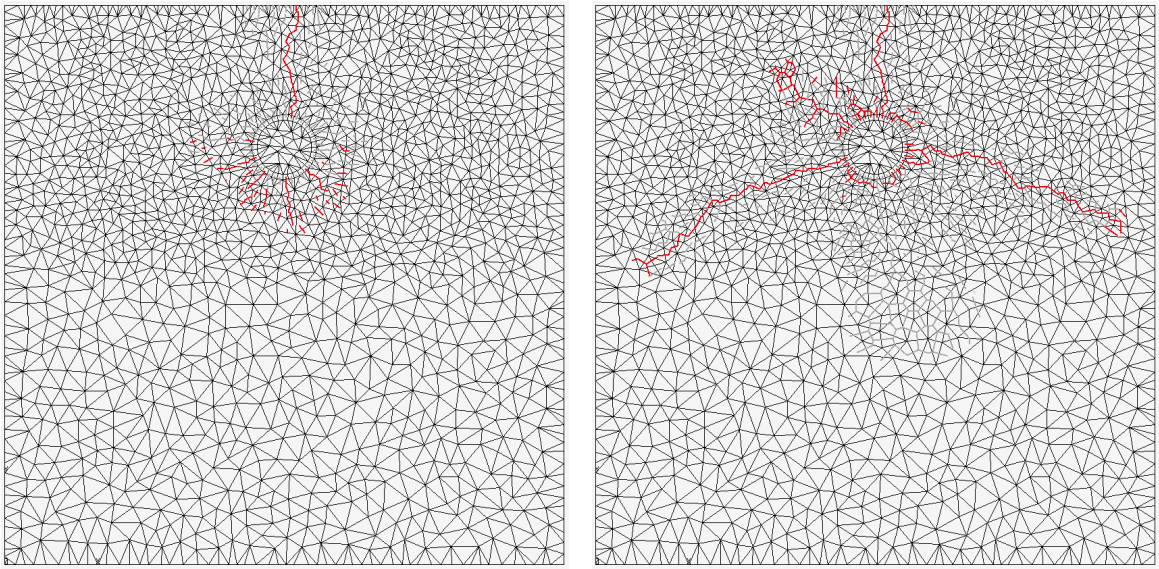

(a) (b)

Figure 7.7: Fracture patterns obtained during analyses for x_{cor} values of (a) 6.87 μm and (b) 82.79 μm.

The deformed meshes that correspond to the fracture patterns presented in Figure 7.7 are shown in Figure 7.8. In each case, the deformations have been magnified by a factor of 50. Although there is damage occurring within some of the elements at $x_{cor} = 6.87\,\mu$m, there deformations are almost invisible to the naked eye, even when a magnification factor is applied. At the end of the analysis, the deformations are much clearer, and the three main fracture patterns observed in Figure 7.8b are visible in the deformed mesh.

7.5 Modelling a Specimen with Multiple Reinforcement Bars

Next, the proposed coupled approach was applied to the prediction of crack widths in a concrete specimen with multiple rebars. The specimen details, a comparison between numerical and experimental results and the fracture patterns obtained for different attack penetration depths are presented in this section.

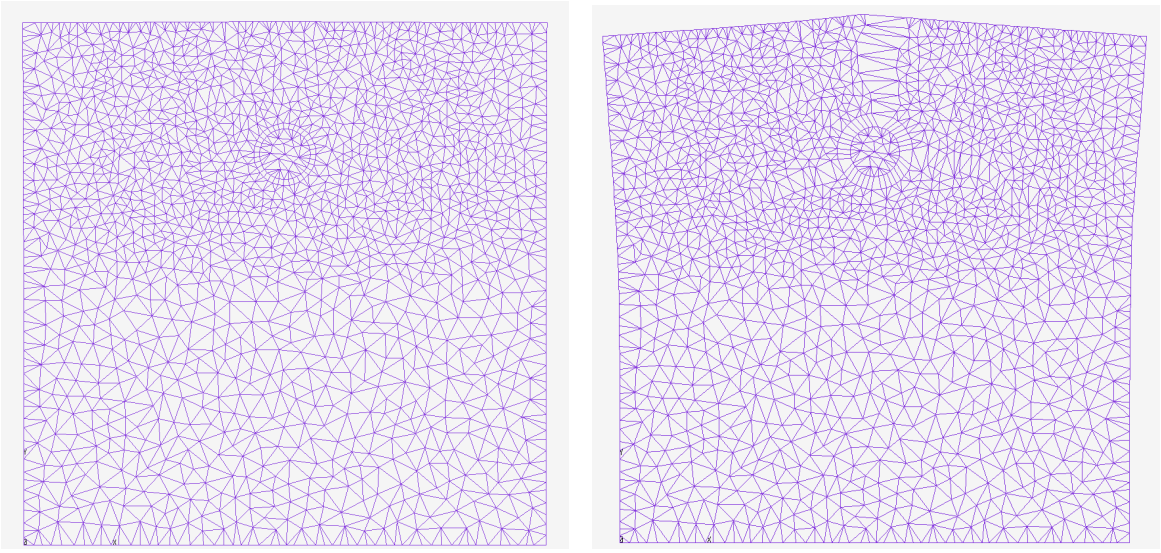

(a) (b)

Figure 7.8: Deformed mesh with a magnification factor of 50 obtained during analyses for x_{cor} values of (a) 6.87 μm and (b) 82.79 μm.

7.5.1 Specimen geometry and boundary conditions

To investigate the ability of the proposed model for predicting cracking in reinforced concrete specimens with multiple reinforcement bars, the experiments reported by Mullard and Stewart (2009a) were analysed. More specifically, the experimental test specimen III-20-16 was modelled. The specimen was a rectangular slab containing four equally spaced mild steel reinforcing bars (Figure 7.9). In this case, the eigen-displacement that drives the analysis is applied to the interface elements along the boundary between the rebar and concrete for each of the rebars (Figure 7.9b). The crack width, wc is determined by calculating the relative displacement between two nodes at the top of the specimen above the most right-hand rebar location (indicated as two green dots in Figure 7.9).

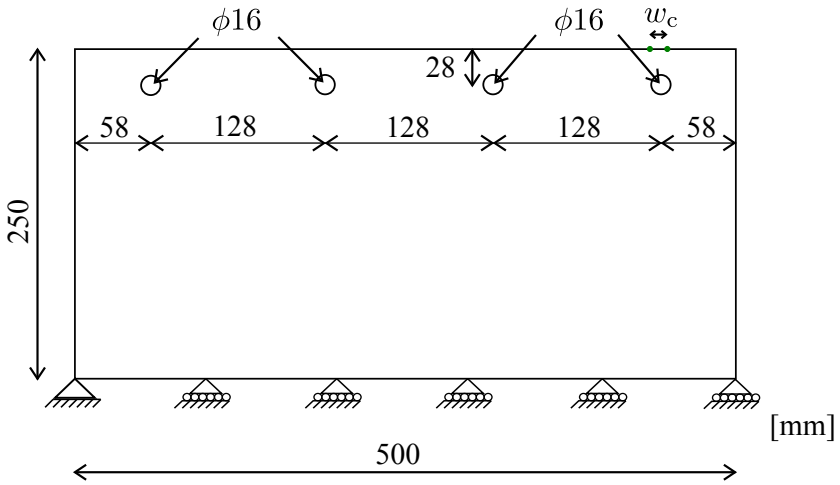

(a)

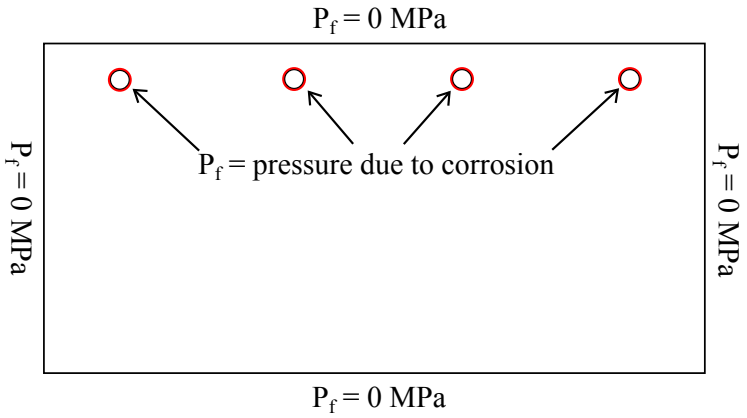

(b)

Figure 7.9: Concrete specimen containing four reinforcing bars: (a) geometry and loading setup according to Mullard and Stewart (2009a) and (b) boundary conditions.

The model parameters used during the analyses are presented in Tables 7.3 and 7.3 for the mechanical and transport models respectively. Where material information was unavailable, values were calculated using Model Code 2010 (FIB, 2012). The value of the viscosity of the corrosion products, the tortuosity factor ξ and the rust expansion coefficient α are the same as the single reinforced specimen i.e. $\mu = 2.0 \times 10^{-2}$ MPa s, $\xi = 0.001$ and $\alpha = 2$. The out-of-plane thickness of the specimen is 1000 mm.

Table 7.3: Mechanical model parameters for concrete specimen containing four rebars.

	f_t [MPa]	E [GPa]	γ	w_f[mm]	c	q
Concrete	3.195	36.995	1	5.6566×10^{-2}	20	2
Steel	-	262.5	1	-	-	-
Interface	3.195	36.995	1.0×10^{-6}	5.6566×10^{-2}	50	2

Table 7.4: Transport model parameters for concrete specimen containing four rebars.

	κ_i [mm^2]	ξ	$\bar{w}_{c,max}$ [mm]	μ[MPa s],
Concrete	1.0×10^{-10}	0.001	0.05	-
Interface	1.0×10^{-10}	0.001	0.05	-
Corrosion products	-	-	-	2.0×10^{-2}

As with the previous analyses, the mechanical mesh includes the concrete, rebar and interface elements (Figure 7.10a). The transport mesh only considers the concrete material as the rebars are assumed to be impermeable (Figure 7.10b).

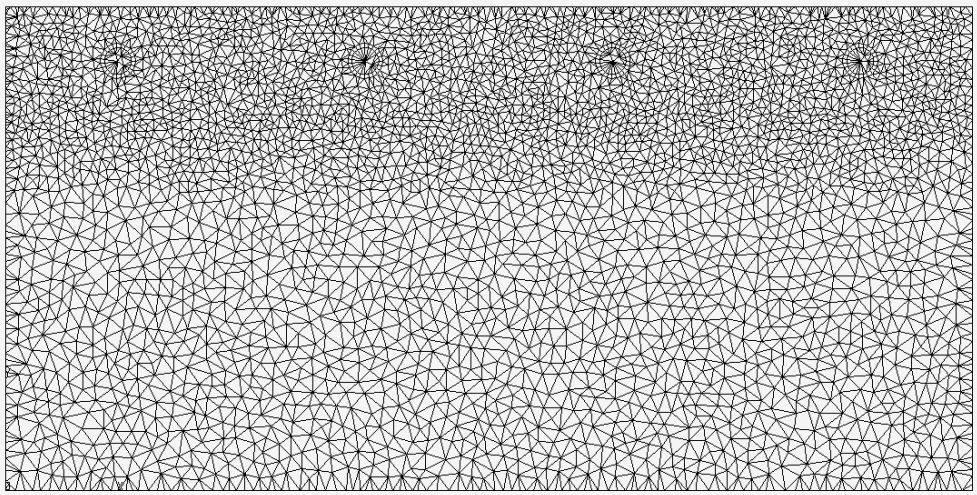

(a)

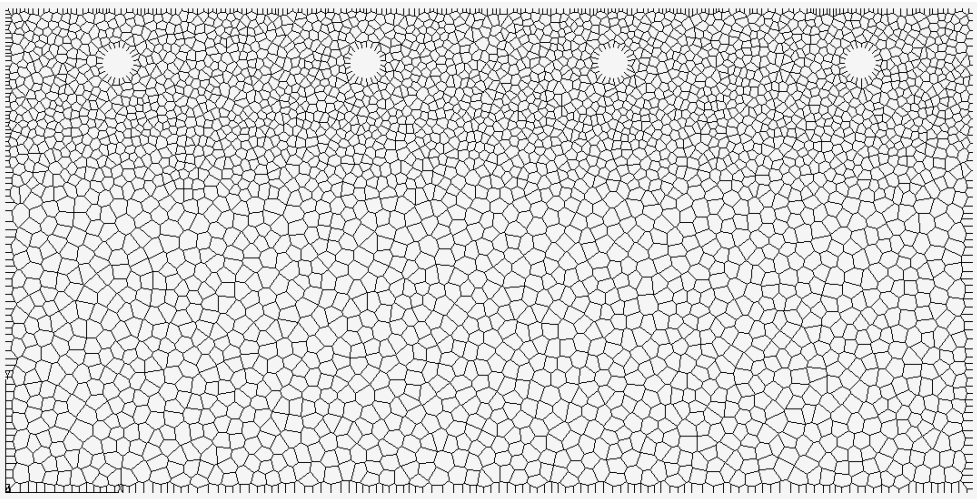

(b)

Figure 7.10: Lattices for the concrete specimen containing multiple reinforcement bars: (a) mechanical lattice and (b) transport lattice.

7.5.2 Comparison of numerical and experimental results

Figure 7.11 presents a comparison between the numerical results and the experimental results presented by Mullard and Stewart (2009a). Reasonable agreement between the numerical and experimental results was obtained.

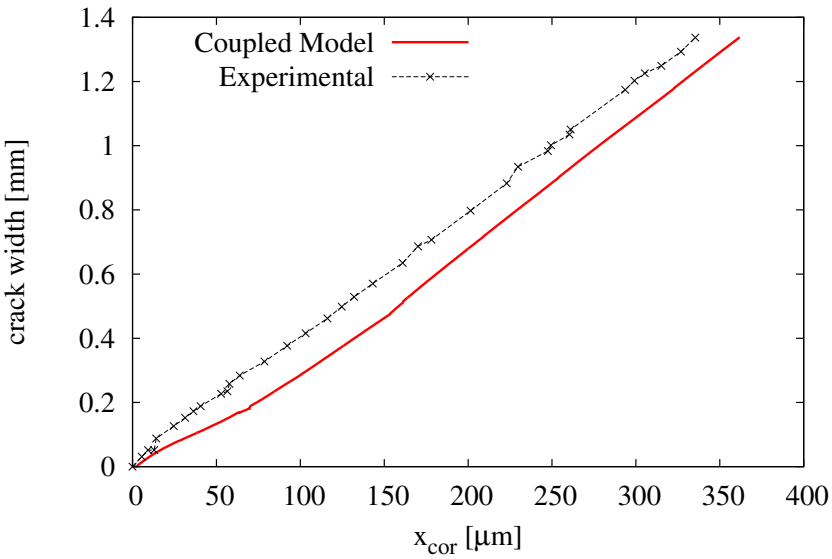

Figure 7.11: Comparison between numerical and experimental results for a specimen containing four rebars (Mullard and Stewart, 2009a).

The amount of corrosion products flowing into the pores was also investigated (Figure 7.13). The initial trend observed is similar to that of the single reinforcement bar specimen analysed in Section 7.4.2. As the cracks initiate, a reduction in the volume of corrosion products penetrating the pores occurs. As the analysis continues and the cracks grow and propagate, the resulting increase in permeability allows for a much greater proportion of the corrosion products to be transported into the concrete surrounding the rebar. However, this figure shows that as the analysis continues and the attack penetration depth increases towards $200\,\mu$m the amount of corrosion products penetrating the pores starts to reduce. This is expected as stresses in the interface elements is tending towards zero (Figure 7.13) and the conductivity has reached its maximum value.

In Figure 7.13, the average fluid pressure at the interface elements is presented. Similarly to results presented in Figure 7.6 the fluid pressure increases to a peak value and then starts to reduce (Figure 7.13). However, in this case the analysis is continued until an x_{cor} greater than $180\,\mu$m is achieved.

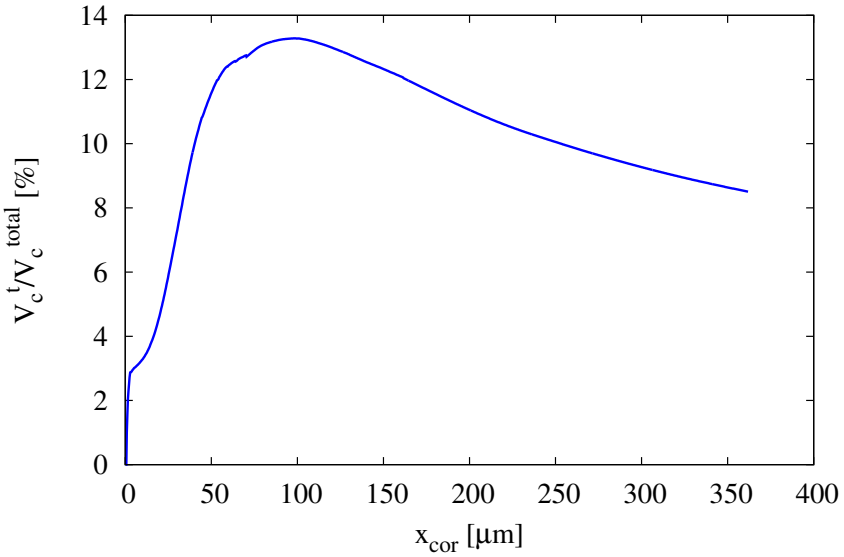

Figure 7.12: Percentage of corrosion products penetrating pores and micro-cracks for a specimen containing four rebars.

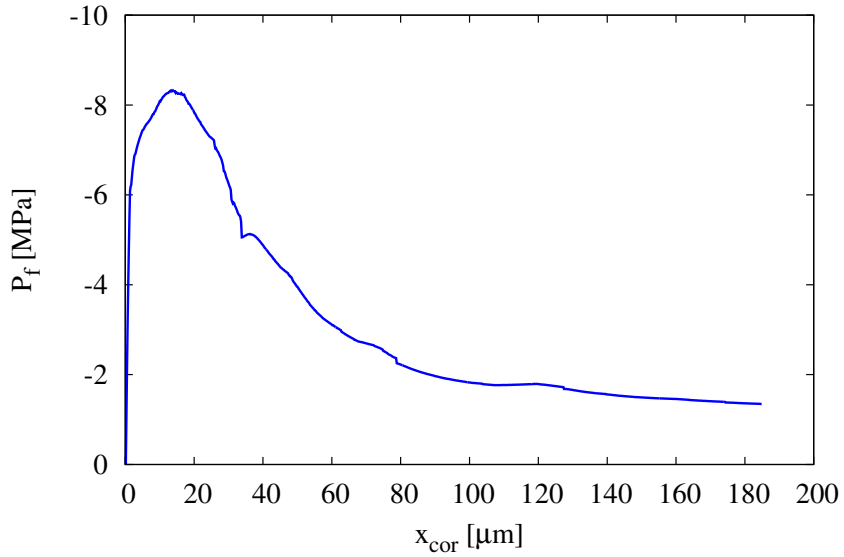

Figure 7.13: Average fluid pressure along the steel/concrete interface for a specimen containing four rebars.

The fracture patterns obtained at different attack penetration depths during the analysis are shown in Figure 7.14. During the early stages of the analysis, vertical cracks form above each of the rebars (Figure 7.14a). Also, as the analysis continues, the cracks propagate horizontally from each rebar, eventually forming one continuous crack (Figure 7.14). This

indicates that delamination of the concrete could occur above the rebars.

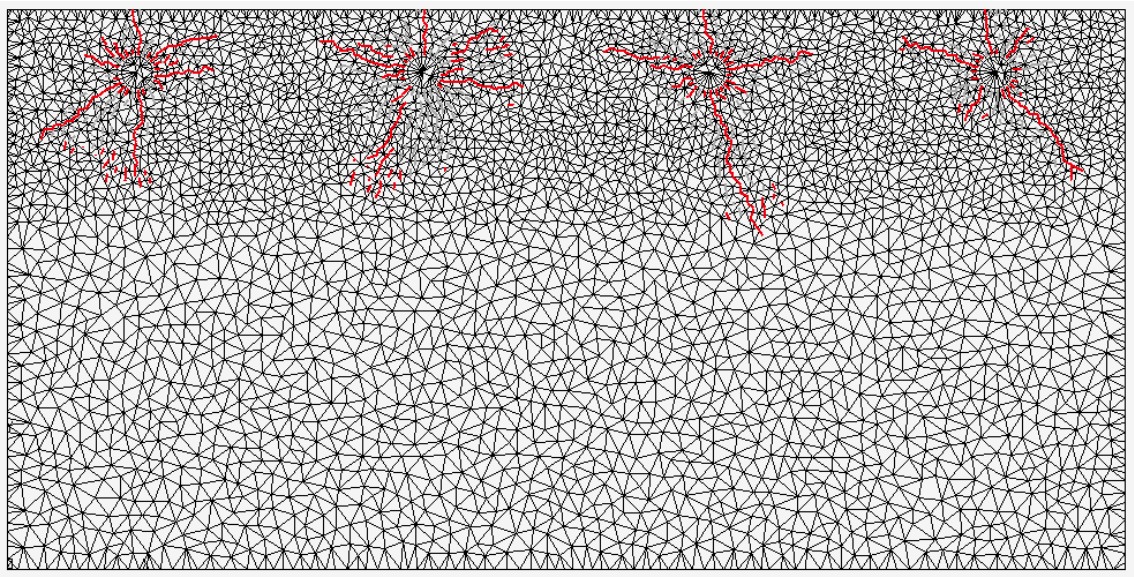

(a)

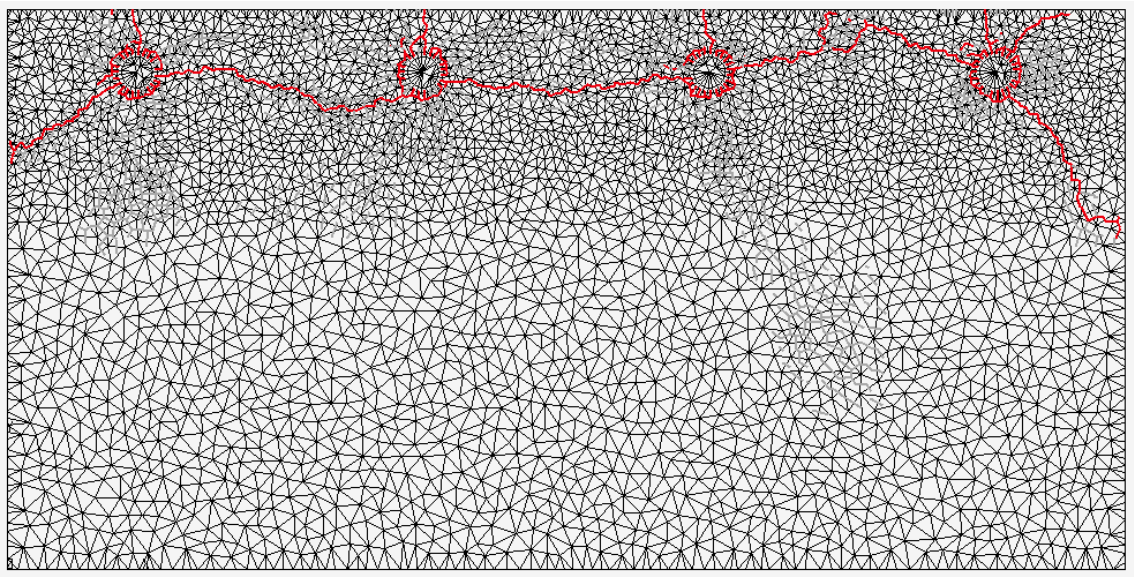

(b)

Figure 7.14: Fracture patterns obtained during analyses of a specimen containing multiple reinforcement bars for x_{cor} values of (a) 8.96 μm and (b) 184.86 μm.

The deformed meshes obtained that correspond to the fracture patterns presented in Figure 7.14 are shown in Figure 7.15. In each case, the deformations have been magnified by a factor of 5. During the early stages of the analysis, when $x_{\text{cor}} = 8.96\,\mu$m, little deformations can be seen (Figure 7.15a). The cracks above the external rebars continue to open, however, the

crack above the left-hand internal rebar closes and causes some unexpected deformations in the surrounding area (Figure 7.15b). One possible cause of this crack closing is the damage constitutive law that is used for describing the mechanical response of the material, which allows for the unloading of elements. A disadvantage of this type of constitutive law is that it allows for cracks to close.

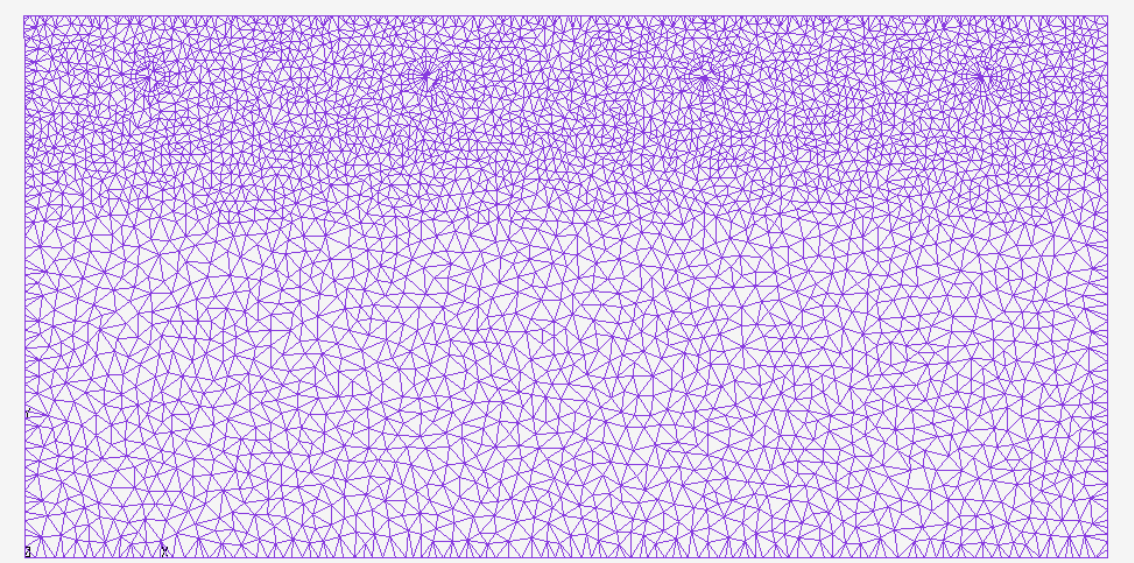

(a)

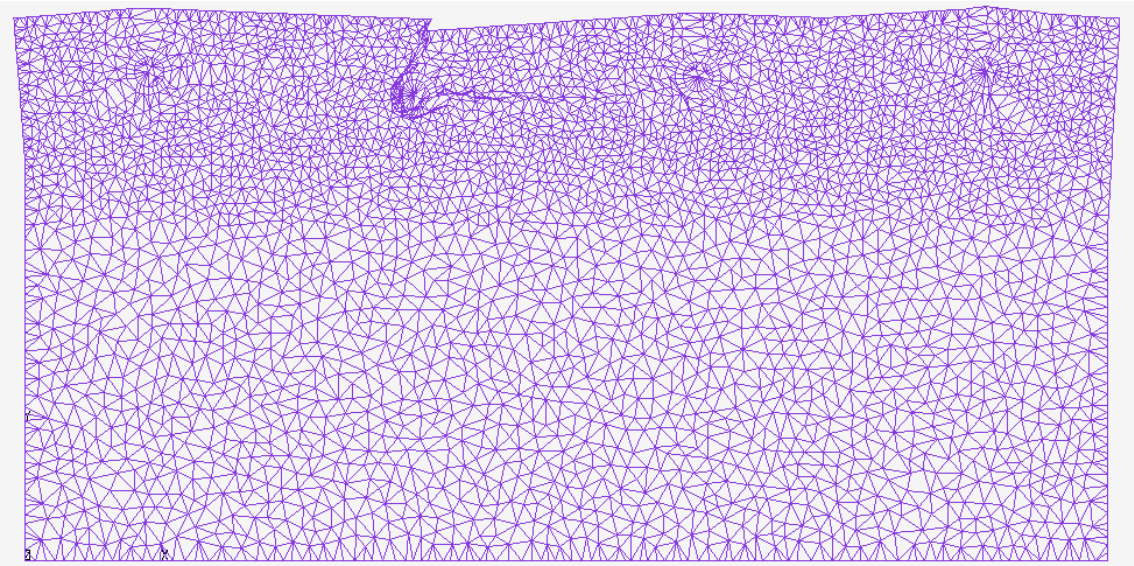

(b)

Figure 7.15: Deformed mesh with a magnification factor of 5 obtained during analyses of a specimen containing four reinforcement bars for x_{cor} values of (a) $8.96\,\mu$m and (b) $184.86\,\mu$m.

7.6 Sensitivity Study

7.6.1 Stiffness of the interface elements

Lattice elements crossing the boundary between the steel and concrete represent the average response of the two adjacent materials and the interface layer, which is much thinner than the length of the element. An alternative approach would have been to determine an equivalent stiffness based on the values used for both the concrete, the steel and potentially the corrosion layer for these interface elements. Considering the stiffness of the concrete and steel only, the equivalent stiffness of the interface elements is determined by

$$E_{\mathrm{i}} = \frac{2}{\frac{1}{E_{\mathrm{c}}} + \frac{1}{E_{\mathrm{s}}}} \tag{7.7}$$

where E_{i} is the equivalent stiffness of the interface elements.

Figure 7.16 presents a comparison between the two ways of modelling the stiffness of the interface elements. It highlights that the stiffness chosen for these interface elements has a negligible effect on the resulting crack width - attack penetration depth x_{cor} graph. When an equivalent stiffness was used convergency problems were encountered during the analysis. Therefore, to overcome these numerical difficulties, the decision was made to use the same stiffness as for the concrete elements.

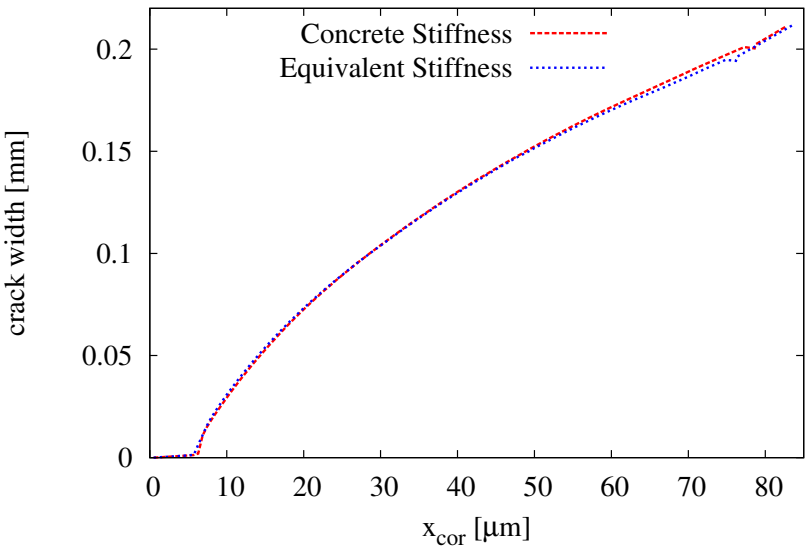

Figure 7.16: Influence of interface stiffness on crack width versus x_{cor}.

7.6.2 Investigation of the effect of viscosity on the time to cracking

Little information is known about the properties of corrosion products. An investigation of the effect of different values of viscosity on the time to cracking was carried out as part of this work. Figure 7.17 presents the relationship between crack widths and the x_{cor} for different values of dynamic viscosity. Some researchers have suggested that corrosion products could be given similar mechanical material properties to that of water (Molina et al., 1993). Expanding this assumption to the fluid properties, the dynamic viscosity μ would be 1×10^{-9}MPa s. If the viscosity of the corrosion products is assumed to be that of water, then an unrealistically large x_{cor} is required for cracking of the concrete to occur. Also, in the proposed approach for determining the time step, more corrosion products would be transported into the pores than are actually being produced according to (7.5).

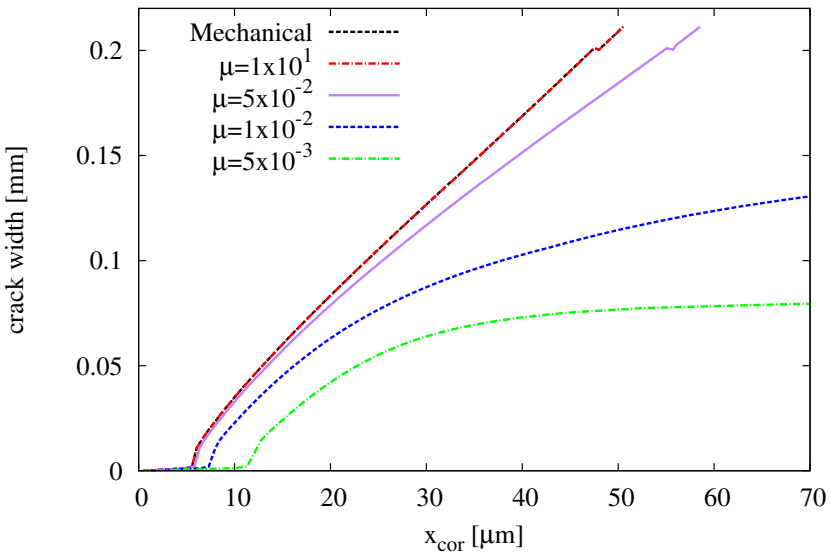

Figure 7.17: Effect of the viscosity on the crack width versus x_{cor}.

In Figure 7.17 it is shown that the dynamic viscosity of the fluid has a strong influence on the crack width versus x_{cor} curves. Increased viscosity leads to an increase of crack width for any given value of x_{cor}. If the value of dynamic viscosity is very large, then the volume of corrosion products transported into the concrete is so small that the response is identical to a purely mechanical analysis.

The ratio between the volume of corrosion products penetrating the pores and the total volume of corrosion products is presented in Figure 7.18 and is determined using (7.6). At any given value of x_{cor}, increased viscosity leads to a decrease in the percentage of corrosion products that has penetrated the pores. This is expected as the corrosion products with a lower viscosity can penetrate the pores easier than those with a higher viscosity, thus allowing a greater volume of corrosion products to penetrate into the concrete.

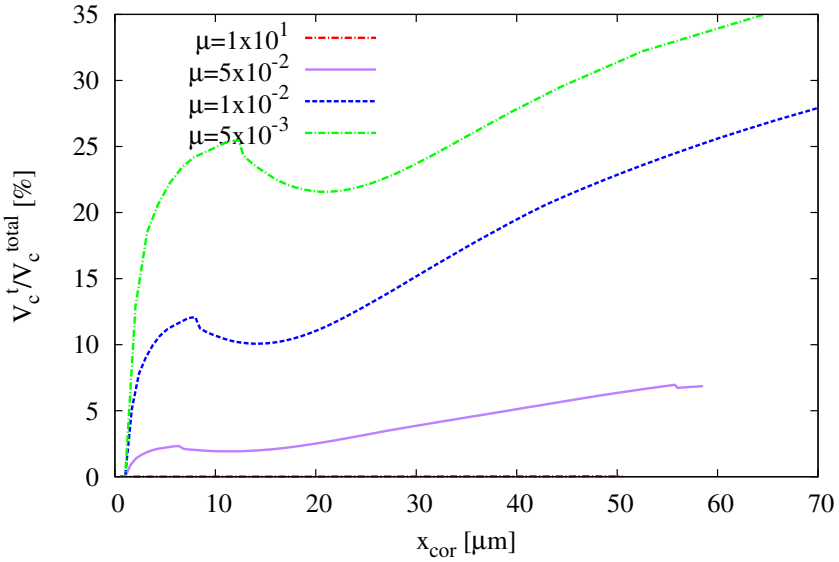

Figure 7.18: Ratio between volume of corrosion products penetrating the pores and the total volume of corrosion products being produced for different values of viscosity.

7.6.3 Investigation of the effect of the tortuosity factor on the time to cracking

The formation of cracks in the specimen causes a change in the hydraulic conductivity of the elements. One of the parameters influencing the change in conductivity due to cracking is the tortuosity factor ξ introduced in (3.8)), which takes into account the roughness of the crack surface. The effect of this parameter on the corrosion-introduced cracking process was studied. For these analyses, a constant value of the dynamic viscosity was chosen as 2.0×10^{-2} MPa s.

Four values of the tortuosity factor ξ were considered; 0, 0.001, 0.005 and 0.01. Figure 7.19 shows the influence of the tortuosity factor on the crack width versus x_{cor} curves. It can be seen that the tortuosity factor has a strong influence on the crack widths at a constant x_{cor}. As the value of the tortuosity factor increases, the crack width obtained at any given value of x_{cor} is reduced.

In Figure 7.19 the curves for $\xi = 0.005$ and 0.01 end at earlier x_{cor} values than the other curves. In both cases, the tortuosity factor allows for more corrosion products to penetrate the pores than actually being produced. For infinitesimal analysis steps, this would result in

infinite time increments in (7.4).

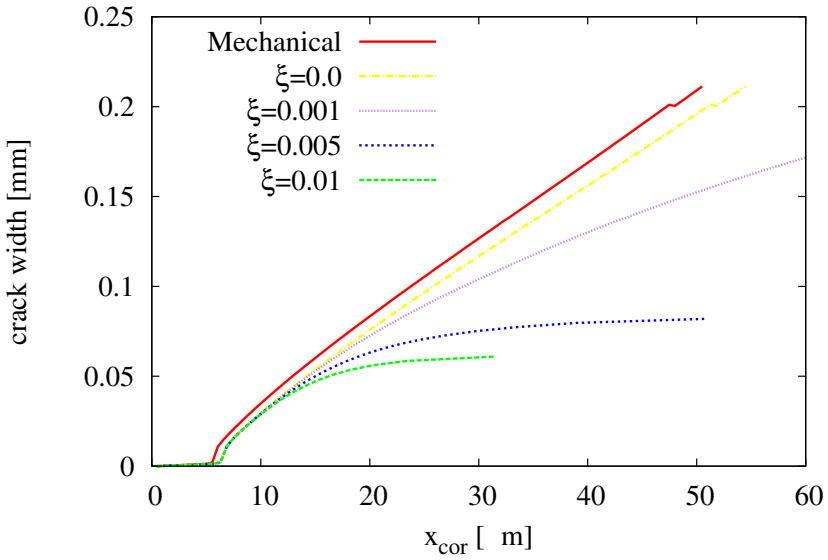

Figure 7.19: Effect of the tortuosity factor on the crack width versus x_{cor}.

In Figure 7.20, the ratio between the volume of corrosion products that has penetrated the pores and cracks surrounding the rebar and the total volume of corrosion products produced are shown for different tortuosity values. Initially, the curves are independent of the tortuosity factor. Then cracking occurs and the influence of the tortuosity factor on the proportion of corrosion products penetrating the pores is visible. This is expected as cracking increases the conductivity of the material, (see (3.8) in Section 3.2.3).

As the cracks increase, so too does the amount of corrosion products flowing into the pores and micro-cracks due to the increase in conductivity caused by cracking (3.8). As long as the crack width is increasing, the conductivity is increasing. Therefore, it was decided during this work to limit the effect of cracking on the cracked conductivity. This was achieved by limiting the equivalent crack width value that enters (3.8). In this work a limiting value of 0.05 mm was chosen.

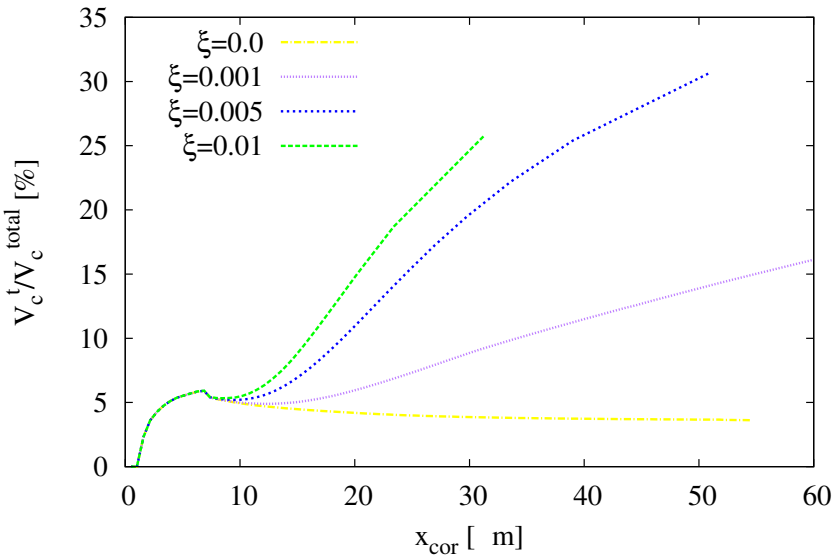

Figure 7.20: Ratio between volume of corrosion products penetrating the pores and the total volume of corrosion products being produced for different values of the tortuosity factor.

7.6.4 Effect of rust expansion coefficient on the time to cracking

In the present section, the effect of the rust expansion coefficient α on the attack penetration depth is considered. Previously in Section 7.4.1, a value of 2 was assumed for this coefficient as proposed by Molina et al. (1993). However, Mullard and Stewart (2009a) suggested a value for the rust expansion coefficient α of 2.79. Figure 7.21 compares both values of α on the resulting crack width - attack penetration depth curves and highlights the strong influence of the rust expansion coefficient value on the resulting crack width - attack penetration depth curves. When an expansion coefficient of 2 is assumed, the crack widths increase much more gradually than when an expansion coefficient of 2.79 is assumed.

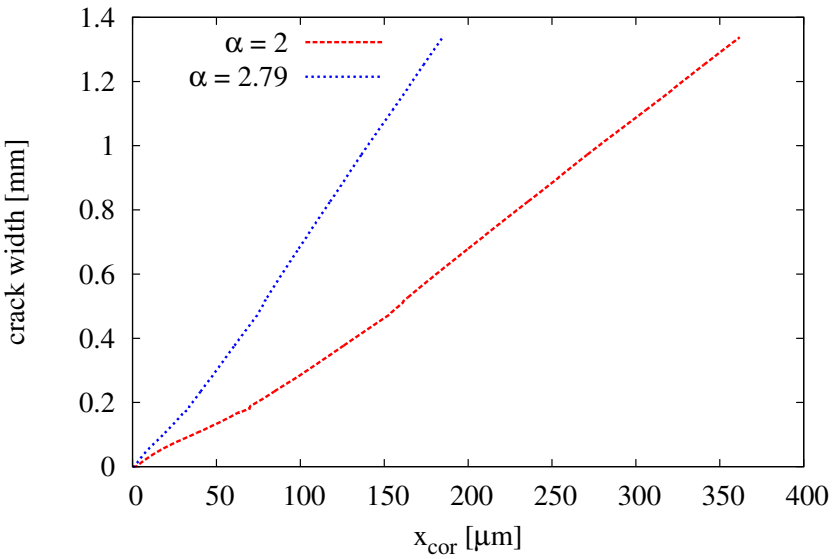

Figure 7.21: Effect of rust expansion coefficient α on the crack width versus x_{cor}.

7.7 Discussion

In this chapter the proposed coupled approach was applied to the modelling of corrosion induced cracking of reinforced concrete. The proposed approach requires that the corrosion products are assigned a value of viscosity. Therefore, using a singularly reinforced concrete specimen, a value for the viscosity was determined based on the experimental results. As expected, this led to very good agreement between numerical and experimental results being obtained for a concrete specimen containing a single reinforcement bar.

The effectiveness of the proposed approach as a predictive model was also investigated in this chapter. Analysis carried out on a specimen containing four reinforcement bars determined that for small attack penetration depths the proposed approach is in very good agreement with experimental results. As the analysis continued, however, the numerical approach underestimated the crack width when compared to experimental results.

A parametric study considering the effect of different values of viscosity and tortuosity factor on the resulting crack width-attack penetration depths was undertaken as part of this work. The dynamic viscosity of the fluid and the tortuosity factor ξ of the cracks both have a strong influence on the crack width versus x_{cor} curves. It was also seen that the rust expansion

coefficient α has a strong influence on the crack width versus x_{cor} curves. Both the viscosity of the fluid and the tortuosity factor can greatly influence the time at which cracking of the specimen occurs as these parameters influence the amount of corrosion products that penetrate the pores and microcracks. The rust expansion coefficientα also has influences the structural integrity of the specimen and can be determined from previous experimental works.

Chapter 8

Conclusions and Future Work

8.1 Conclusions

A review of existing coupled transport-mechanical lattice approaches highlighted the need for a model for predicting the durability of concrete. More specifically, one area that would benefit from an accurate coupled approach is corrosion-induced cracking of reinforced concrete. Corrosion-induced cracking is a difficult phenomenon to monitor and predict, therefore, repairs are sometimes carried out even when not necessary. Numerical approaches that can accurately predict this phenomenon could be used to inform practising engineers of when a repair is really necessary or if indeed a structure requires replacing.

This thesis proposes a coupled transport-mechanical approach that can be used for predicting the durability of reinforced concrete. In order to verify the individual models, uncoupled analyses were carried out using the mechanical and transport models presented in Chapter 3 of this thesis, allowing for the assessment of the quality and accuracy of the individual models. Firstly, analyses were carried out on two notched concrete specimens. In both cases, the mechanical model captures well the physical phenomena observed during experimental testing, in the form of fracture patterns and load-crack mouth opening displacement (CMOD) curves. The dependence of the results on the level of mesh refinement used was assessed through investigation of the load-CMOD curves obtained from the analyses. This showed

the model to be reasonably independent of the level of mesh refinement used. The ability of the model to accurately capture fracture patterns was also investigated. In both cases, the model was able to accurately predict the experimental crack patterns.

Secondly transport analyses were carried out on a one-dimensional soil column and an uncracked concrete specimen. For the case of the one-dimensional soil column, the numerical results were compared to the results predicted using an alternative numerical approach (Vogel et al., 2000). Very good agreement was achieved for both the original and modified versions of the van Genuchten model compared to the results presented by Vogel et al. (2000). More importantly, these analyses also showed the transport model to be reasonably independent of both the element length and the time step used during analyses shown in this work.

The transport analysis was carried out on an uncracked concrete specimen was used to illustrate that the two-dimensional network of pipe elements can correctly reproduce the one-dimensional solution. It was not possible to determine a value for the intrinsic permeability from the literature, therefore a value was chosen that allowed the numerical results to agree well with the experimental results at the early stages of the analysis. However, at later stages the numerical model over-predicts the change in water content over the depth of the beam. A simplified one-dimensional model of the concrete specimen was analysed and the results compared to that of the two-dimensional problem. Very good agreement between the one-dimensional and two-dimensional results was obtained.

Secondly, an analysis of a cracked reinforced concrete specimen was undertaken. In this two stage problem, a three-point bending test was performed on a mechanical specimen to achieve a specified crack width. Once the required crack width was achieved, the equivalent crack widths in the elements were imported into the transport model to account for the effect of cracking on the permeability of the material. A transport analysis was then performed on the cracked specimen. This was the first instance where coupling between the individual mechanical and transport models was considered. The importance of including the effect of cracking on the transport model was highlighted in this work as the crack acts as a conduit for additional ingress of water into the specimen.

One advantage of the proposed approach is that it could be used not only for modelling the

durability of concrete but also for examining crack propagation in the case of hydraulic fracture problems. To verify that the coupled transport-mechanical approach proposed in this work is suitable for modelling the interaction between the mechanical and transport properties of porous materials, numerical simulations of a thick-walled cylinder specimen subjected to an internal fluid pressure were carried out and the numerical results were compared to an analytical solution for the radial displacements of an elastic thick-walled cylinder, which was derived in the present study. This work is limited to a stationary flow problem with homogeneous properties for both the fluid and the solid. Three different values of Biot's coefficient were considered during this work; $b = 1$, 0.5 and 0. The effect of different values of Poisson's ratio ν on the resulting radial displacements was investigated in this work. For values of $\nu = 0$ and $\nu = 0.1$, excellent agreement between the numerical displacements and the analytical solution was achieved. As the value of Poisson's ratio ν was increased to 0.2, reasonable agreement between the numerical and analytical solutions was maintained, but the quality of the agreement is slightly reduced.

The proposed approach was applied to the problem of corrosion-induced cracking of reinforced concrete. Using a single reinforced concrete specimen, a value of viscosity of the corrosion products was determined leading to very good agreement between numerical and experimental results. This value of viscosity was then applied to the analysis of a specimen containing four reinforcement bars to investigate the effectiveness of the proposed approach as a predictive model. Reasonable agreement with experimental results was obtained. However, the proposed coupled approach underpredicts the crack width when compared to experimental results.

A parametric study considering the effect of different values of viscosity and tortuosity factor on the resulting crack width-attack penetration depths was undertaken as part of this work. The dynamic viscosity of the fluid and the tortuosity factor ξ of the cracks both have a strong influence on the crack width versus x_{cor} curves. It was also seen that the rust expansion coefficient α has a strong influence on the crack width versus x_{cor} curves. Analysis of this specimen also highlighted a short-coming of the damage constitutive law used in the coupled approach. The closing of existing cracks was observed during an investigation of the deformed mechanical mesh.

Consideration of the penetration of the corrosion products into the pores and micro-cracks

during analysis delays the time at which cracking of the specimen occurs and produces a more realistic representation of the physical phenomena that occur during the process of corrosion-induced cracking.

8.2 Future Work

The approach proposed in this thesis could be suitable for use by practising engineers for determining when repair of a structure is required. However, before the proposed approach is suitable for this purpose, further development of a number of areas would be necessary. In the first instance, the present damage law could be extended to include a plasticity approach, in a similar way to the work presented by Grassl and Rempling (2008). This could resolve the problem of cracks unrealistically closing during the numerical analysis as this is not always an accurate description of the physical phenomena.

It would also be beneficial to develop an advection model that could be combined with the proposed approach. This would allow for the monitoring of the penetration of the corrosion products into the pores and micro-cracks surrounding the rebar. Thus, further investigation of the effect of cracking on the penetration of the corrosion products could be carried out.

Further analyses could be carried out to determine a more accurate value for the viscosity of the corrosion products. At present, the value assumed is based only on the results of one experiment. For this value to be fully validated, further analyses would be required. It could also be advantageous to apply the proposed approach to real-life structures to assess the potential of the proposed approach.

The proposed coupled approach could also be applied to problems of hydraulic fracture in porous materials. Hydraulic fracturing is difficult to replicate experimentally, particularly on a large scale. Therefore a reliable numerical model would be of great benefit. For this purpose, it would be of benefit to extend the proposed approach to a three-dimensional model in order to capture effects of varying ground conditions.

References

Ababou, R., Millard, A., Treille, E., Durin, M., Plas, F., 1994. Continuum modeling of coupled thermo-hydro-mechanical processes in fractured rock, in: Computational Methods in Water Resources X, Kluwer Academic Publishers, Netherlands. pp. 651–658.

Aldea, C.M., Ghandehari, M., Shah, S.P., Karr, A., 2000. Estimation of water flow through cracked concrete under load. ACI Materials Journal 97, 567–575.

Alonso, C., Andrade, C., Diez, J.M., 1998. Factors controlling cracking of concrete affected by reinforcement corrosion. Materials and Structures 31, 435–441.

Andrade, C., Alonso, C., Molina, F.J., 1993. Cover cracking as a function of bar corrosion: Part I-Experimental test. Materials and Structures 26, 453–464.

Andrade, C., Figueiredo, E.P., 2012. Opciones Teoricas de actuacion en la marquesina del estadio de maracana (In Spanish), in: 4Âž Congreso de Patología y Rehabilitación de Edificios, PATORREB, Santiago de Compostela.

Arrea, M., Ingraffea, A.R., 1982. Mixed-mode crack propagation in mortar and concrete. Technical Report. Department of Structural Engineering, Cornell University. New York.

Asahina, D., Houseworth, J.E., 2013. Hydro-mechanical model for wetting/drying and fracture development in geomaterials. Computers & Geosciences 65, 13–23.

Bangert, F., Kuhl, D., Meschke, G., 2004. Chemo-hygro-mechanical modelling and numerical simulation of concrete deterioration caused by alkali-silica reaction. International Journal for Numerical and Analytical Methods in Geomechanics 28, 689–714.

Baroghel-Bouny, V., Mainguy, M., Lassabatere, T., Coussy, O., 1999. Characterization and identification of equilibrium and transfer moisture properties for ordinary and high-performance cementitious materials. Cement and Concrete Research 29, 1225–1238.

Bažant, Z.P., 1979. Physical model for steel corrosion in concrete sea structures - application. Journal of the Structural Division 105, 1155–1166.

Bažant, Z.P., Tabbara, M.R., Kazemi, M.T., Pijaudier-Cabot, G., 1990. Random particle model for fracture of aggregate or fiber composites. Journal of Engineering Mechanics 116, 1686–1705.

Beaton, J.L., Stratfull, R.F., 1963. Environmental influence of corrosion of reinforcing steel in concrete substructures. Technical Report. National Research Council. Washington (DC).

Berton, S., Bolander, J.E., 2006. Crack band model of fracture in irregular lattices. Computer Methods in Applied Mechanics and Engineering 195, 7172–7181.

Biot, M.A., 1941. General theory of three dimensional consolidation. Journal of Applied Physics 12, 155–164.

Bolander, J., Hong, G., 2003. Rigid Body Spring Network Modeling of Prestressed Concrete Members 5, 595–604.

Bolander, J.E., Berton, S., 2004. Simulation of shrinkage induced cracking in cement composite overlays. Cement and Concrete Composites 26, 861–871.

Bolander, J.E., Saito, S., 1998. Fracture analyses using spring networks with random geometry. Engineering Fracture Mechanics 61, 569–591.

Bolander, J.E., Shiraishi, T., Isogawa, Y., 1996. An adaptive procedure for fracture simulation in extensive lattice networks. Engineering Fracture Mechanics 54, 325–334.

Cabrera, J.G., 1996. Deterioration of concrete due to reinforcement steel corrosion. Cement and Concrete Composites 18, 47–59.

Caré, S., Nguyen, Q.T., L'Hostis, V., Berthaud, Y., 2008. Mechanical properties of the rust layer induced by impressed current method in reinforced mortar. Cement and Concrete Research 38, 1079–1091.

Carsel, R., Parrish, R., 1988. Developing joint probability distributions of soil water retention characteristics. Water Resources Research , 755–769.

Chatzigeorgiou, G., Picandet, V., Khelidj, A., Pijaudier-Cabot, G., 2005. Coupling between progressive damage and permeability of concrete: analysis with a discrete model. International Journal for Numerical and Analytical Methods in Geomechanics 29, 1005–1018.

Chernin, L., Val, D., Volokh, K., 2010. Analytical modelling of concrete cover cracking caused by corrosion of reinforcement. Materials and Structures 43, 543–556.

Chernin, L., Val, D.V., 2011. Prediction of corrosion-induced cover cracking in reinforced concrete structures. Construction and Building Materials 25, 1854–1869.

Clear, K.C., 1976. Time-to-corrosion of reinforcing steel in concrete slabs. Technical Report. Federal Highway Administration.

Cusatis, G., Bazant, Z., Cedolin, L., 2003. Confinement-Shear Lattice Model for Concrete Damage in Tension and Compression: I. Theory. Journal of Engineering Mechanics 129, 1439.

van Damme, L., Detournay, E., Cheng, A.H.D., 1989. A two-dimensional poroelastic displacement discontinuity method for hydraulic fracture. International Journal for Numerical and Analytical Methods in Geomechanics 13, 215–224.

Duffó, G.S., Morris, W., Raspini, I., Saragovi, C., 2004. A study of steel rebars embedded in concrete during 65 years. Corrosion Science 46, 2143–2157.

El Maaddawy, T., Soudki, K., 2007. A model for prediction of time from corrosion initiation to corrosion cracking. Cement and Concrete Composites 29, 168–175.

FIB, 2012. FIB-Model Code for Concrete Structures 2010. Technical Report. International Federation for Structural Concrete.

Fu, P., Johnson, S.M., Carrigan, C.R., 2013. An explicity coupled hygro-mechanical model for simulating hydraulic fracturing in arbitrary discrete fracture networks. International Journal for Numerical and Analytical Methods in Geomechanics , 2278–2300.

Galvez, J.C., Elices, M., Guinea, G.V., Planas, J., 1998. Mixed mode fracture of concrete under proportional and nonproportional loading. International Journal of Fracture , 267–284.

Gardner, D., Jefferson, A., Hoffman, A., 2012. Investigation of capillary flow in discrete cracks in cementitious materials. Cement and Concrete Research 42, 972–981.

Gawin, D., Pesavento, F., Schrefler, B.A., 2006. Hygro-thermo-chemo-mechanical modelling of concrete at early ages and beyond. Part II: shrinkage and creep of concrete. International Journal for Numerical Methods in Engineering 67, 332–363.

van Genuchten, M.T., 1980. A closed-form equation for predicting the hydraulic conductivity of unsaturated soils. Soil Society of America Journal 44, 892–898.

Grassl, P., 2009. A lattice approach to model flow in cracked concrete. Cement and Concrete Composites 31, 454–460.

Grassl, P., Davies, T., 2011. Lattice modelling of corrosion induced cracking and bond in reinforced concrete. Cement and Concrete Composites 33, 918–924.

Grassl, P., Fahy, C., Gallipoli, D., Bolander, J.E., 2013. A lattice model for liquid transport in cracked unsaturated heterogeneous materials, in: Van Mier, J., Ruiz, G., Andrade, C., Yu, R.C., Zhang, X. (Eds.), VIII International Conference on Fracture Mechanics of Concrete and Concrete Structures FraMCoS-8, Toledo.

Grassl, P., Jirásek, M., 2010. Meso-scale approach to modelling the fracture process zone of concrete subjected to uniaxial tension. International Journal of Solids and Structures 47, 957–968.

Grassl, P., Rempling, R., 2008. A damage-plasticity interface approach to the meso-scale modelling of concrete subjected to cyclic compressive loading. Engineering Fracture Mechanics 75, 4804–4818.

Griffith, D., Mustoe, G., 2001. Modelling of elastic continua using a grillage of structural elements based on discrete element concepts. International Journal for Numerical Methods in Engineering 50, 1759–1775.

Hrennikoff, A., 1941. Solution of problems of elasticity by the Framework method. Journal of Applied Mechanics 8, A619–A715.

Hüttig, C., Stemmer, K., 2008. Finite volume discretization for dynamic viscosities on Voronoi grids. Physics of the Earth and Planetary Interiors 171, 137–146.

Idiart, A.E., López, C.M., Carol, I., 2010. Modeling of drying shrinkage of concrete specimens at the meso-level. Materials and Structures 44, 415–435.

Jankovic, D., 2001. Numerical analysis of moisture flow and concrete cracking by means of Lattice Type Models, in: Fracture Mechanics of Concrete Structures: Proceedings of the 4th International Conference FRAMCOS4, Cachan. pp. 231–238.

Jirásek, M., Grassl, P., 2008. Evaluation of directional mesh bias in concrete fracture simulations using continuum damage models. Engineering Fracture Mechanics 75, 1921–1943.

Jox, S., Becker, C., Meschke, G., 2007. Hygro-mechanical modelling of cracked concrete in the framework of the X-FEM, in: Fracture Mechanics of Concrete Structures: Proceedings of the 4th International Conference FRAMCOS4.

Kawai, T., 1978. New Discrete Models and Their Application to Seismic Analysis of Structures. Nuclear Engineering and Design 48, 207–229.

Kim, J., Moridis, G.J., 2013. Development of the T+M coupled flow geomechanical simulator to describe fracture propagation and coupled flow thermal geomechanical processes in tight/shale gas systems. Computers & Geosciences 60, 184–198.

Li, L., Meng, Q., Wang, S., Li, G., Tang, C., 2013. A numerical investigation of the hydraulic fracturing behaviour of conglomerate in Glutenite formation. Acta Geotechnica 8, 597–618.

Liu, H., Rutqvist, J., 2012. Coupled Hydro-mechanical Processes Associated with Multiphase Flow in a Dual-continuum System: Formulations and an Application. Rock Mechanics and Rock Engineering 46, 1103–1112.

Liu, Y., Weyers, R., 1998. Modeling the Time-to-Corrosion Cracking in Chloride Contaminated Reinforced Concrete Structures. Materials Journal 6, 675–681.

Lundgren, K., 2002. Modelling the effect of corrosion on bond in reinforced concrete. Magazine of Concrete Research 54, 165–173.

Martys, N., Ferraris, C., 1997. Capillary Transport in Mortars and Concrete. Cement and Concrete Research 27, 747–760.

Meschke, G., Grasberger, S., 2003. Numerical modeling of coupled hygromechanical degradation of cementitious materials. Journal of engineering mechanics 129, 383–392.

Michel, A., Pease, B., Geiker, M., Stang, H., Forbes, J., 2011. Monitoring reinforcement corrosion and corrosion-induced cracking using non-destructive x-ray attenuation measurements. Cement and Concrete Research 41, 1085–1094.

Michel, A., Pease, B., Peterová, A., Geiker, M., Stang, H., Thybo, A., 2013. Penetration of corrosion products and corrosion-induced cracking in reinforced cementitious materials: experimental investigations and numerical simulations. Cement and Concrete Composites 47, 75–86.

van Mier, J., 1997. Fracture Processes of Concrete. 1st ed., CRC-Press.

Molina, F.J., Alonso, C., Andrade, C., 1993. Cover cracking as a function of rebar corrosion: part 2 numerical model. Materials and Structures 26, 532–548.

Morinaga, S., 1990. Prediction of service lives of reinforced concrete buildings based on rate of corrosion of reinforcing steel, in: Baker, J., Davies, H., Majumdar, A., Nixon, P. (Eds.),

Durability of Building Materials and Components: Proceedings of the Fifth International Conference, Taylor & Francis. pp. 5–17.

Mosley, B., Bungey, J., Hulse, R., 2007. Reinforced concrete design to Eurocode 2. Sixth ed., MacMilan.

Moukarzel, C., Herrmann, H., 1992. A vectorizable random lattice. Journal of Statistical Physics 68, 911–923.

Mullard, J.A., Stewart, M.G., 2009a. Corrosion-induced cover cracking of RC structures: new experimental data and predictive models. Technical Report 275. Centre for Infrastructure Preformance and Reliability, University of Newcastle. New South Wales, Australia.

Mullard, J.A., Stewart, M.G., 2009b. Stochastic assessment of timing and efficiency of maintenance for corroding RC structures. Journal of Structural Engineering 135, 887–895.

Mullard, J.A., Stewart, M.G., 2011. Corrosion-induced cover cracking: new test data and predictive models. ACI Structural Journal 108, 71–79.

Nakamura, H., Srisoros, W., Yashiro, R., Kunieda, M., 2006. Time-dependent structural analysis considering mass transfer to evaluate deterioration process of RC structures. Journal of Advanced Concrete Technology 4, 147–158.

Nemecek, J., 2005. Effect of transversal reinforcement in normal and high strength concrete columns. Materials and Structures 38, 665–671.

Noorishad, J., Ayatollahi, M.S., Witherspoon, P.A., 1982. A finite-element method for coupled stress and fluid flow analysis in fractured rock masses. International Journal of Rock Mechanics and Mining Sciences & Geomechanics Abstracts 19, 185–193.

Nooru-Mohamed, M., 1992. Mixed-mode fracture of concrete: an experimental approach. Ph.D. thesis. Delft University of Technology.

Okabe, A., Boots, B., Sugihara, K., Chiu, S., 2000. Spatial Tessellations: Concepts and Applications of Veronoi Diagrams. 2nd revise ed., Whiley-Blackwell.

Ouglova, A., Berthaud, Y., François, M., Foct, F., 2006. Mechanical properties of an iron oxide formed by corrosion in reinforced concrete structures. Corrosion Science 48, 3988–4000.

Ožbolt, J., Oršanić, F., Balabanić, G., 2014. Modeling processes related to corrosion of steel reinfrocement and damage in concrete, in: Bićanić, N., Mang, H., Meschke, G., de Borst,

R. (Eds.), Computational Modelling of Concrete Structures, CRC Press, St. Anton am Arlberg. pp. 705–714.

Patzák, B., Rypl, D., 2012. Object-oriented, parallel finite element framework with dynamic load balancing. Advances in Engineering Software 47, 35–50.

Pijaudier-Cabot, G., Bažant, Z., 1988. Nonlocal damage theory. Journal of Engineering Mechanics 113, 1512–1533.

Pijaudier-Cabot, G., Dufour, F., Choinska, M., 2009. Permeability due to the increase of damage in concrete: from diffuse to localized damage distributions. Journal of Engineering Mechanics 135, 1022–1028.

Purvis, R.L., Babaei, K., Clear, K.C., Markow, M.J., 1994. Life-cycle cost analysis for protection and rehabilitation of concrete bridges relative to reinforcement corrosion. Technical Report. Strategic Highway Research Program, National Research Council. Washington DC.

Roels, S., Moonen, P., De Proft, K., Carmeliet, J., 2006. A coupled discrete-continuum approach to simulate moisture effects on damage processes in porous materials. Computer Methods in Applied Mechanics and Engineering 195, 7139–7153.

Roels, S., Vandersteen, K., Carmeliet, J., 2003. Measuring and simulating moisture uptake in a fractured porous medium. Advances in Water Resources 26, 237–246.

Sadouki, H.G.M., van Mier, J., 1997. Meso-level analysis of moisture flow in cement composites using a lattice-type approach. Materials and Structures 30, 579–587.

Saka, T., Bolander, J., Grassl, P., 2012. Dual-lattice models of coupled fracture-flow in quasi-brittle materials, in: Proceedings of 17th Japan Computational Engineering Conference, Japan Society of Computational Engineering and Science (JSCES), Kyoto. pp. A–9–5 on CD–ROM.

Sanz, B., Planas, J., Sancho, J.M., 2013. An experimental and numerical study of the pattern of cracking of concrete due to steel reinforcement corrosion. Engineering Fracture Mechanics 114, 26–41.

Savija, B., Luković, M., Pacheco, J., Schlangen, E., 2013. Cracking of the concrete cover due to reinforcement corrosion: A two-dimensional lattice model study. Construction and Building Materials 44, 626–638.

Schlangen, E., 1993. Experimental and numerical analysis of fracture processes in concrete. Ph.D. thesis. Delft University of Technology.

Schlangen, E., Garboczi, E.J., 1996. New method for simulating fracture using an elastically uniform random geometry lattice. International Journal of Engineering Science 34, 1131–1144.

Schlangen, E., Mier, J.G.M., 1992. Simple lattice model for numerical simulation of fracture of concrete materials and structures. Materials and Structures 25, 534–542.

Shawki, G., El-Wahil, S., 1970. Strength of thinck-walled permeable cylinders. International Journal of Mechanical Sciences 12, 535–551.

Shewchuk, J.R., 2002. Delaunay refinement algorithms for triangular mesh generation. Computational Geometry: Theory and Applications 22, 21–74.

Suda, K., Misra, S., Motohashi, K., 1993. Corrosion products of reinforcing bars embedded in concrete. Corrosion Science 35, 1543–1549.

Sukumar, N., 2003. Voronoi cell finite difference method for the diffusion operator on arbitrary unstructured grids. International Journal for Numerical Methods in Engineering 57, 1–34.

Terzaghi, K., 1925. Erdbaumechanik auf boden physikalischer Grundlage. Franz Deuticke.

Thomas, H.R., He, Y., 1997. A coupled heat-moisture transfer theory for deformable unsaturated soil and its algorithmic implementation. International Journal for Numerical Methods in Engineering 40, 3421–3441.

Tuutti, K., 2981. Service Life of Structures with Regard to Corrosion of Embedded Steel. ACI-SP65 65, 223–236.

Valko, P., Economides, M., 1995. Hydraulic Fracture Mechanics. First ed., Wiley.

Vecchio, F.J., Shim, W., 2004. Experimental and analytical reexamination of classic concrete beam tests. Journal of Structural Engineering 130, 460–469.

Vogel, T., Cislerova, M., 1988. On the reliability of unsaturated hydraulic conductivity calculated from the moisture retention curve. Transport in Porous Media 3, 1–15.

Vogel, T., van Genuchten, M.T., Cislerova, M., 2000. Effect of the shape of the soil hydraulic functions near saturation on variably-saturated flow predictions. Advances in Water Resources 24, 133–144.

Vu, K., Stewart, M.G., Mullard, J., 2005. Corrosion-induced cracking: experimental data and predictive models. ACI structural journal , 719–726.

Wang, L., Soda, M., Ueda, T., 2008. Simulation of chloride diffusivity for cracked concrete based on RBSM and truss network model. Journal of Advanced Concrete Technology 6, 143–155.

Wang, L., Ueda, T., 2011. Mesoscale modeling of water penetration into concrete by capillary absorption. Ocean Engineering 38, 519–528.

Witherspoon, P., Wang, J., Iwai, K., Gale, J., 1980. Validity of cubic law for fluid flow in a deformable rock fracture. Water Resources Research 16, 1016–1024.

Wittmann, F., Zhang, P., Zhao, T., Lehmann, E., Vontobel, P., 2008. Neutron radiography, a powerful method for investigating water penetration into concrete., in: Advances in Civil Engineering Materials., Proceedings of The 50-year Teaching and Research Anniversary of Prof. Sun Wei, Nanjing, China.

Wong, H., Zhao, Y., Karimi, A., Buenfeld, N., Jin, W., 2010. On the penetration of corrosion products from reinforcing steel into concrete due to chloride-induced corrosion. Corrosion Science 52, 2469–2480.

Wong, H.S., Zobel, M., Zimmerman, R.W., Buenfeld, N.R., 2009. Influence of the interfacial transition zone and microcracking on the diffusivity, permeability and sorptivity of cement-based materials after drying. Magazine of Concrete Research 61, 571–589.

Yu, R., Ruiz, G., Chaves, E., 2008. A comparative study between discrete and continuum models to simulate concrete fracture. Engineering Fracture Mechanics 75, 117–127.

Zhang, P., Wittmann, F., Zhao, T., Lehmann, E., Vontobel, P., 2011. Neutron radiography, a powerful method to determine time-dependent moisture distributions in concrete. Nuclear Engineering and Design 241, 4758–4766.

Zubelewicz, A., Bažant, Z.P., 1987. Interface element modelling of fracture in aggregate composites. Journal of Engineering Mechanics 113, 1619–1630.

Appendix A

Derivation of Mass Transport Equation

This section presents the derivation of the differential equation used to describe mass transport (Section 3.2.1). The following simplifications and assumptions were made during the derivation of the differential equation

- Calculations are carried out for a 2D specimen.
- Fluid is regarded as incompressible.
- Laminar flow conditions.
- A positive sign is assumed for liquid tension, unlike the convention of soil mechanics which assumes compression positive.

A mass balance equation is used to describe the change in mass of fluid over time. Firstly the flux is calculated. For this, it is assumed that the flow into the specimen is positive and the flow out is negative. This notation is shown in Figure A.1.

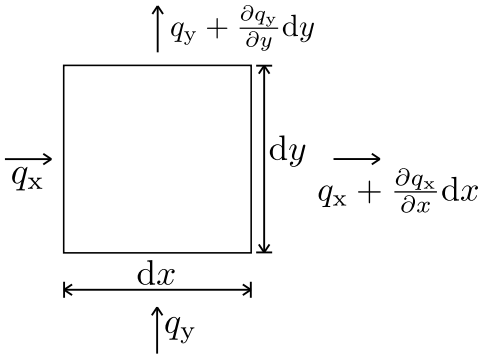

Figure A.1: Flux Diagram.

From Figure A.1, for mass flow in the x-direction the influx, I_x , is calculated as

$$I_x = \rho \left[q_x dy - (q_x + \frac{\partial q_x}{\partial x} dx) dy \right] dt = -\rho \frac{\partial q_x}{\partial x} dx dy dt \tag{A.1}$$

where ρ is the density of the fluid. Correspondingly, the mass flow in the y-direction results in

$$I_y = \rho \left[q_y dx - (q_y + \frac{\partial q_y}{\partial y} dy) dx \right] dt = -\rho \frac{\partial q_y}{\partial y} dy dx dt \tag{A.2}$$

This results in a total influx of

$$I = I_x + I_y = I = -\rho \left(\frac{\partial q_x}{\partial x} + \frac{\partial q_y}{\partial y} \right) dx dy dt \tag{A.3}$$

The total influx calculated in (A.3) is re-written as

$$I = -\rho \, \mathrm{div}\, \mathbf{q} \, dx dy dt \tag{A.4}$$

in which $\mathrm{div} = \begin{pmatrix} \frac{\partial}{\partial x} & \frac{\partial}{\partial y} \end{pmatrix}$ and $\mathbf{q} = \{q_x, q_y\}^T$.

Next the effect of porosity is considered. The mass of fluid within the specimen is calculated

as

$$M = \rho\theta \mathrm{d}x\mathrm{d}y \tag{A.5}$$

where M is the mass, ρ is the density of the fluid and θ is the volumetric water content. The change in mass with time is

$$\frac{\mathrm{d}M}{\mathrm{d}t}\mathrm{d}t = \rho\frac{\partial\theta}{\partial t}\mathrm{d}x\mathrm{d}y\mathrm{d}t \tag{A.6}$$

The influx is related to the storage in the material by the following mass balance equation

$$\frac{\mathrm{d}M}{\mathrm{d}t}\partial t = I \tag{A.7}$$

Previously, the definitions for the change in mass with time and the influx were defined in (A.6) and (A.4) respectively. Setting (A.6) and (A.4) into (A.7) and dividing by dxdydt gives

$$\rho\frac{\partial\theta}{\partial t} = -\rho\mathrm{div}\,\mathbf{q} \tag{A.8}$$

Through Darcy's Law, $\mathbf{q}$ is

$$\mathbf{q} = \frac{k}{\rho g}\mathrm{grad}\,(P_c - \rho g z) \tag{A.9}$$

where k is the hydraulic conductivity, g is gravity and z is the elevation. Expanding the left-hand side of (A.8) to include the change in capillary pressure P_c, the following equation is obtained

$$\rho\frac{\partial\theta}{\partial P_\mathrm{c}}\frac{\partial P_\mathrm{c}}{\partial t} = -\rho\mathrm{div}\,\mathbf{q} \tag{A.10}$$

From (A.10), the capacity of the material c can be defined as

$$c = -\rho\frac{\partial\theta}{\partial P_\mathrm{c}} \tag{A.11}$$

Combining the mass balance equation (A.10) and the application of Darcy's law to the conservation equation (A.9) leads to the following

$$c\frac{\partial P_\mathrm{c}}{\partial t} - \frac{k}{g}\mathrm{div}\,(\mathrm{grad}(P_\mathrm{c} - \rho g z)) = 0 \tag{A.12}$$

Also, by taking the k/g outside of the divergence term, it is assumed that k does not vary with x or y.